University of Texas at Arlington

MavMatrix

2023

Utilization of biomimetic molecules to control the carbonation of cementitious phases

Muhammad Intesarul Haque

UTILIZATION OF BIOMIMETIC MOLECULES TO CONTROL

THE CARBONATION OF CEMENTITIOUS PHASES

Prepared by

MUHAMMAD INTESARUL HAQUE

Presented to the Faculty of the Graduate School of The University of Texas at
Arlington in Partial Fulfilment of the Requirements for the Degree of

DOCTOR OF PHILOSOPHY

THE UNIVERSITY OF TEXAS AT ARLINGTON, TEXAS, USA

Fall 2023

(December 2023)

THE UNIVERSITY OF TEXAS AT ARLINGTON
GRADUATE SCHOOL STATEMENT OF COMMITTEE APPROVAL

1. Dr. Warda Ashraf, Committee Chair

Associate Professor, Department of Civil Engineering

The University of Texas at Arlington, Texas, USA

2. Dr. Surendra P Shah

Professor, Department of Civil Engineering

The University of Texas at Arlington, Texas, USA

3. Dr. Nur Yazdani

Professor, Department of Civil Engineering

The University of Texas at Arlington, Texas, USA

4. Dr. Suyun Ham

Associate Professor, Department of Civil Engineering

The University of Texas at Arlington, Texas, USA

5. Dr. Jan Olek

Professor, Department of Civil Engineering

Purdue University, Indiana, USA

ACKNOWLEDGEMENTS

All praise to the Almighty!

I want to express my profound gratitude to my Ph.D. supervisor, Professor Warda Ashraf, for her invaluable guidance throughout this dissertation. Her unwavering support and encouragement during my graduate studies have been instrumental in my academic journey. Her supervision has enhanced my research skills and boosted my confidence. Her insightful feedback has been a significant asset to my academic growth.

I would like to express gratitude to my dissertation committee members, Professor Surendra P Shah, Professor Jan Olek, Professor Nur Yazdani, Professor Suyun Ham for their guidance and support throughout the journey.

I am thankful to Professor Jiechao Jiang, Dr. Yi Shen from the Characterization Center for Materials and Biology (CCMB), UTA for their kind support. I am grateful to my former and current lab mates – Dr. Rakibul I Khan, Ishrat Baki Borno, Adhora Tahsin, Nithya Nair, Nishad Ahmed, Farzana Mustari and Anand Ambikadas. I am also thankful to Mr. Qays Mohammed for his technical help.

DEDICATION

To my parents – Md. Enamul Hoque, Rina Afrooz Jahan and my sister – Tasnia Haque
And my support system Shaika Shafiq

TABLE OF CONTENTS

LIST OF FIGURES

LIST OF TABLES

XV

Abstract

This study introduces an innovative approach to mitigate carbonation-induced degradation of C-S-H and to enhance the carbonation properties of low calcium based cementitious materials by utilizing specific biomimetic molecules. In this study, four different biomimetic molecules were utilized. Details about their chemical formula and chemical structure can be found in Chapter 1. The dissertation is broadly focused on two aspects, Part 1 (Chapter 2 and 3) evaluated the role of biomimetic molecules in reducing the carbonation degradation of C-S-H. Part 2 (Chapter 4 and 5) assessed the effectiveness of the biomimetic molecules as performance enhancing admixture of carbonation cured dicalcium silicates.

For part 1, synthetic C-S-H samples were prepared, incorporating biomimetic molecules M-1 and M-2. The impact of these biomimetic molecules on C-S-H, both before and after carbonation, was examined using various analytical techniques, such as ^{29}Si NMR, TEM, nanoindentation, and FTIR. Without these molecules, unmodified C-S-H underwent complete polymerization into silica gel after 168 hours of carbonation. However, C-S-H modified with biomimetic molecules retained its original structure even after 28 days of carbonation. The organic molecules also substantially increased the elastic modulus of C-S-H, a property that further improved after carbonation. Furthermore, this study addresses knowledge gaps by demonstrating the application of in-situ ATR-FTIR for monitoring decalcification kinetics of C-S-H, evaluating the influence of C/S ratio, pH, and the presence of M-1 on decalcification kinetics, and monitoring in-situ $CaCO_3$ formation and polymorph conversion during C-S-H carbonation for various experimental conditions.

For part 2 of the dissertation, this research investigated the effectiveness of different biomimetic molecules, including M-1, M-3, and M-4, to enhance the properties of carbonated dicalcium silicate-based cementitious systems. Low dosages (2.5% and 5%) of these molecules were

incorporated into the γ-C$_2$S paste. XRD and SEM analysis confirmed alterations in CaCO$_3$ polymorphs formation, with M-4 exhibiting the highest CaCO$_3$ content. While porosity measurements from MIP and DVS were higher, the modified batches showed increased compressive and flexural strengths. Specifically, the 2.5% M-4-modified batch displayed a 61% higher compressive strength than the control batch. Additionally, 5% M-3 and 5% M-1 batches demonstrated the highest flexural strength, 53% greater than the control batch, aligning with nanoindentation results that revealed an enhanced elastic modulus due to the formation of organic-inorganic hybrid phases. Finally, the study comprehensively explores the effects of M-4 with different molecular weights (MW 2000, MW 5000, and MW 240000) and dosages (0.5%, 1%, and 2.5%) on the carbonation of β-C$_2$S binders. It highlights the influence of M-4 on calcium carbonate (CaCO$_3$) formation, crystal polymorphs, microstructure, and mechanical strength. MW 5000 and MW 240000 significantly promoted CaCO$_3$ formation and controlled crystal polymorphs, particularly at the 1% dosage. The study employs various analyses to observe carbonation properties, revealing the potential of M-4-modified β-C$_2$S to enhance microstructural integrity and mechanical properties. Even under elevated temperature curing (50°C), M-4-modified β-C$_2$S binders maintained impressive mechanical strength, illustrating their adaptability across diverse environmental conditions. In summary, this research underscores the potential of biomimetic molecules to enhance construction materials, offering opportunities to optimize phase formation and boost mechanical properties.

Chapter 1: Research background and literature reviews

1.1 Introduction

Concrete produced using a high volume of supplementary cementitious materials (SCMs) and Ca-rich alkali-activated materials are sustainable alternatives to ordinary Portland cement (OPC)-based materials due to their lower carbon footprint [1], [2]. These sustainable cementitious materials contain C-S-H (or C-A-S-H) as the primary binding phases and are devoid of $Ca(OH)_2$, because of which they are more susceptible to deterioration caused by atmospheric CO_2 compared to the OPC [3]–[9].

In hardened cementitious composites, CO_2 can diffuse into the empty pores, where it reacts with water from the pore solution and forms bicarbonate ions. The bicarbonate ions react with portlandite ($Ca(OH)_2$) and C-S-H, forming $CaCO_3$ and water. The reaction between CO_2 present in atmosphere with C-S-H results in decalcification and polymerization of the binding phases followed by the formation of calcite [10]. The low molecular volume of calcite compared to that of C-S-H eventually leads to increased porosity in the matrix [7], [11]–[13] in addition to lower compressive strengths [14], carbonation shrinkage [15], [16], and increased vulnerability of reinforcement to corrosion due to the reduction of alkalinity [17], [18]. The increase in large porosity in the cementitious matrixes due to carbonation also increases the diffusivity of detrimental chloride/sulfate ions into the matrix, resulting in the further degradation of the durability performances of the matrix [19]–[21].

Nevertheless, carbonation technology is a promising way to enhance the performance of cement concrete composites. With more than 30 billion tons of carbon dioxide (CO_2) emissions into the atmosphere every year, global climate change has led to various environmental problems that need

immediate attention. Carbon capture, utilization, and storage (CCUS) technologies will play a key role in mitigating these adverse effects. Hence, carbonation has to be applied in such a way that the detrimental effects are well controlled. One impactful way is to control the calcium carbonate polymorphs formation in the cement concrete system.

1.2 Carbonation technology

Carbonation can be incorporated into both fresh and mature Portland cement (PC) concrete during the curing process, which involves applying it within the first few hours after casting and during long-term curing. The accelerated carbonation reaction is a highly exothermic and diffusion-controlled process, subject to the influence of both material properties, like physical attributes and chemical composition, as well as carbonation conditions, such as CO_2 concentration, pressure, and temperature [22]. This chemical reaction between CO_2 and calcium-based compounds in cement releases heat and offers several advantages, including (i) rapid strength improvement, (ii) enhanced durability, and (iii) the permanent sequestration of CO_2 [23], [24].

Furthermore, carbonation can be harnessed to improve the quality of recycled concrete aggregates (RCAs) and stimulate the strength development of artificial aggregates (AAs) [25]–[27]. These outcomes can greatly reduce CO2 emissions in the construction industry over the long term, thus mitigating its impact on global warming and the environment. Nevertheless, the commercial application of CO_2 in construction materials and associated technologies remains in its early stages of development, currently confined to prefabricated products like concrete blocks [28]. These advancements require ongoing support from additional research endeavors to address the obstacles hindering large-scale implementation [29].
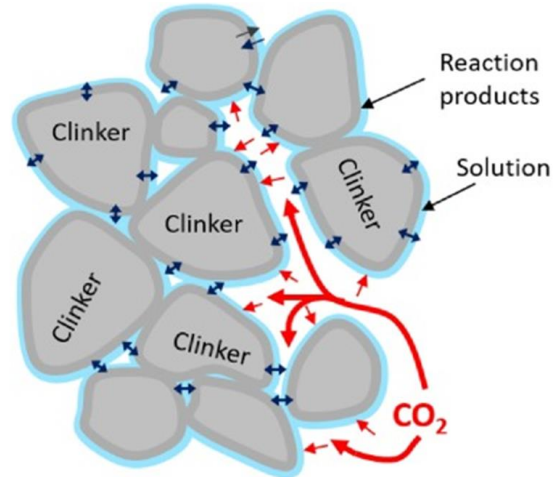
Figure 1.1: Schematic diagram showing the carbonation curing of cementitious materials [30]

The carbonation reaction follows these equations -

$$Ca_3SiO_5 + 3CO_2 + nH_2O \rightarrow 3CaCO_3 + SiO_2 \bullet nH_2O \tag{1}$$

$$\beta - Ca_2SiO_4 + 2CO_2 + nH_2O \rightarrow 2CaCO_3 + SiO_2 \bullet nH_2O \tag{2}$$

$$\gamma - Ca_2SiO_4 + 2CO_2 + nH_2O \rightarrow 2CaCO_3 + SiO_2 \bullet nH_2O \tag{3}$$

$$Ca(OH)_2 + CO_2 + H_2O \rightarrow CaCO_3 + 2H_2O \tag{4}$$

$$Ca_xSi_yH_z\,O_{(x+2y+z/2)} + xCO_2 \rightarrow xCaCO_3 + y(SiO_2 \bullet tH_2O) + (z/2 - yt)H_2O \tag{5}$$
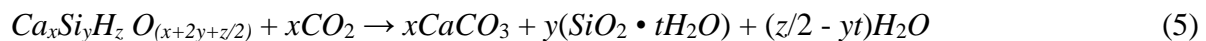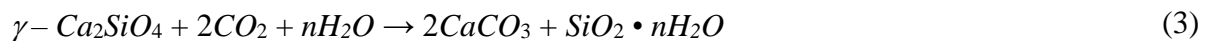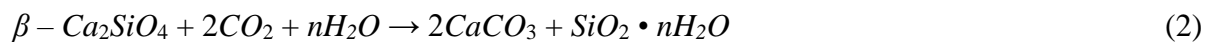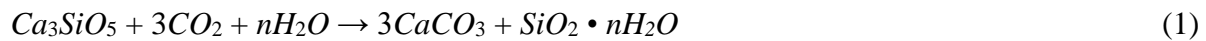
Accelerated carbonation techniques have been developed for RCAs to achieve rapid carbonation within hours [31] . Generally, the optimal conditions for carbonation involve a CO_2 concentration of 40–60% [32]–[34], humidity of 40–70% [34] and temperature of 20–30ºC [25], [35]. To further improve the carbonation efficiency of RCAs, pressurized carbonation technologies involving high CO_2 pressures are also employed [36]. CO_2 Concrete exhibits increased quality in concrete shrinkage and permeability when examining recycled aggregate concrete. The sequestration of CO_2 allows for the reduction of water absorption of recycled aggregate, which permits a great

improvement in drying shrinkage and water permeability [37]. Accelerated carbonation of RCAs consists of the following key steps shown in **Figure 1.2**.
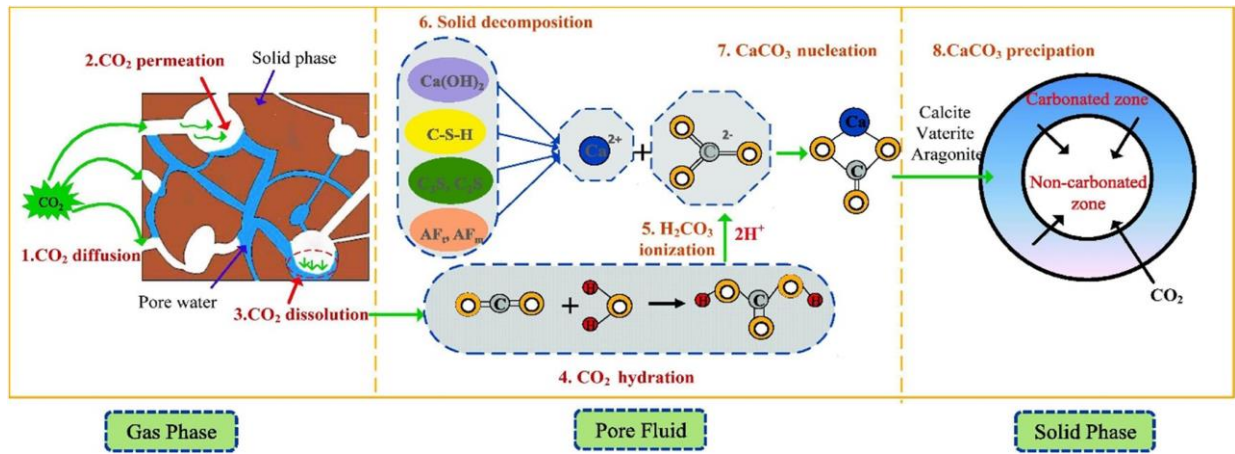
Figure 1.2: Reaction process involved in the accelerated carbonation treatment of RCA [38]

In the context of early-age carbonation, CO_2 is integrated into the production of concrete masonry units (CMUs), promoting an immediate carbonation reaction that occurs concurrently with the heat of hydration reaction of cement. CMUs are particularly suitable for CO_2 sequestration due to their relatively porous nature. This approach encompasses two methods for introducing CO_2 into the production process.

The first method entails introducing CO_2 during the curing phase by delivering it into a conventional curing chamber, which operates under either low- or high-pressure steam conditions. The second method involves injecting controlled quantities of gaseous CO2 directly into the mixer, which feeds into a masonry unit production machine. In both methods, carbon dioxide becomes permanently sequestered in the form of solid limestone within the concrete matrix.

Early-age carbonation involves the introduction of carbon dioxide (CO_2) during concrete production, specifically targeting the early stages of fresh concrete. This process can initiate as

early as during concrete mixing and continue until the completion of accelerated curing, offering a greater degree of control.

Carbonation curing offers environmental benefits by reducing shrinkage, minimizing defects in finished block units, and decreasing the energy required for concrete curing when applied to concrete blocks. Additionally, the incorporation of CO_2 into concrete production can lead to higher early strength, enabling producers to reduce their cement usage and, in turn, decrease their carbon footprint. Pre-cast concrete elements produced by CO_2 curing are shown in **Figure 1.3**.

Figure 1.3: Precast concrete elements produced by CO₂ curing mitigate shrinkage [39]

Nevertheless, carbonation can cause degradation in the cementitious phases if the calcium carbonate polymorphs formation is not well controlled. Hence, controlling the calcium carbonate polymorph in cementitious phases can show new avenues of improvement in the promising sector of carbonation curing and utilization.

1.3 Biomimetic molecules to resist carbonation degradation in calcium silicate hydrates

One of the potential solutions for reducing the extent of carbonation damage in cementitious materials is to control the polymorphs of the precipitated $CaCO_3$ particles [40]. Calcite, aragonite, vaterite, and amorphous calcium carbonate (ACC) are the primary polymorphs that can form during the carbonation of cementitious matrixes containing C-S-H or C-A-S-H as the primary

binding phases [41]–[43]. Other crystalline polymorphs, including ikaite ($CaCO_3 \bullet 6H_2O$) and mono-hydrocalcite ($CaCO_3 \bullet 1H_2O$), may also form [44], [45], but these are very rare. Even though this polymorph selection route is affected by several factors, including relative humidity (RH) [46], CO_2 concentration [47], and pH [48], in general, the final polymorph is calcite as it is the most stable form of $CaCO_3$. However, these polymorphs have different intrinsic characteristics, including solubility. The solubility constants for calcite, aragonite, and vaterite are $10^{-8.48}, 10^{-8.34}$ and $10^{-7.91}$, respectively [49], [50], and ACC is 120 times more soluble than calcite [51]. As suggested by Morandeau and White [40], the formation of ACC can reduce the extent of carbonation in cementitious matrixes due to the higher solubility of this phase and consequent saturation of solution. In support of this, a few recent studies have also shown that magnesium-stabilized ACC formation can lead to lower carbonation damage in alkali activated materials (AAM) [40], [52].

An alternative method of controlling the crystallization of $CaCO_3$ can be learned by studying the natural biomineralization process [53]. A series of biomimetic molecules have already been identified that can stabilize typically metastable ACC, aragonite, and vaterite during the biomineralization process by forming organic-inorganic hybrids [54]–[57]. However, the effectiveness of those biomimetic molecules in cementitious environments to control the crystallization of $CaCO_3$ is not well studied yet. In a previous study, it was observed that a few amino acids can control the crystallization of $CaCO_3$ in carbonation-cured wollastonite composites [58]. Among the tested amino acids, L-aspartic was found to stabilize ACC in carbonated composites. Such stabilization of ACC resulted in a reduced degree of carbonation, as expected, but also significantly improved mechanical performances of the carbonated composite [58]. The improved mechanical performance was attributed to the formation of organic-inorganic hybrid

6

phases [58]. Additionally, several past studies suggested that polydopamine can be used to control the crystallization of CaCO3 and stabilize vaterite and ACC [59]–[62]. The additional benefit of polydopamine is its self-adhesive characteristics that results from its polymerization in an alkaline environment [63]. Because of these adhesive characteristics, Fang et al. applied polydopamine in fine sand to improve its adherence to cement particles [64].

1.4 Biomimetic molecules to enhance properties of carbonation in calcium silicates

On the contrary, the carbonation activated low-lime calcium silicate binder is a recent addition to these alternative cementitious systems [65]. These low-lime phases are often not used in OPC because they lack hydraulic properties. However, in the presence of CO_2, these low-lime calcium silicates show increased reactivity [66]–[68]. Compared to the manufacturing of OPC, utilization of these low-lime calcium silicates can reduce the carbon footprint of cement by minimizing the temperature and clinker production [65].

Among the calcium silicates, dicalcium silicate (C_2S) can potentially lower the energy needed for cement manufacturing by 0.29 to 0.42 GJ/ton of clinker when used as the major cement compound (for example, belite-based binders) [69]. Even though Portland cement largely comprises β-C_2S, in recent studies, γ-C_2S has received attention for several reasons. First, γ-C_2S is less active than β-C_2S [69]. If an activation method is identified to be effective for γ-C_2S, it is expected to be equally or more effective for β-C_2S activation. Second, even though both γ-C_2S and β-C_2S have lower production temperature requirements, β-C_2S often requires more energy to grind than C_3S [69]. It is well-known that the production of γ-C_2S promotes the formation of fine powder due to 'dusting' effect lowering the grinding energy requirement when used as the primary cement component. Finally, studies showed that wollastonite (CS) and rankinite (C_3S_2) behave similarly

as that of γ-C_2S when exposed to carbonation curing owing to the common non-hydraulic behavior [65]–[67]. Therefore, knowledge of C_2S's reactivity can give direction for activation of low-carbon calcium silicate-based cementitious materials.
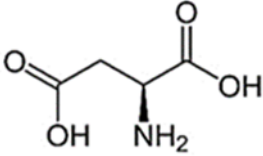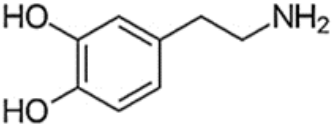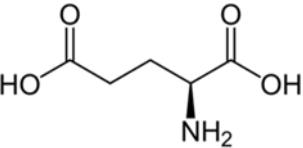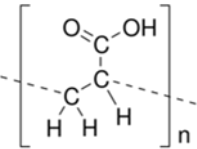
Crystalline characteristics of $CaCO_3$ have a substantial impact on the mechanical performances of carbonated cement composites [70], [71]. Formation of the polymorphs of $CaCO_3$ ideally should follow the Ostwald's process; the least stable polymorph amorphous calcium carbonate (ACC) is the first to nucleate, which then crystallizes to form metastable vaterite or aragonite, and finally, forms the most stable polymorph – calcite [72], [73]. It is difficult to control the relative proportions of the different $CaCO_3$ polymorphs formed in the carbonated composites due to relative humidity, CO_2 concentration, pH etc. [74]–[78]. The variation of different $CaCO_3$ polymorphs results in significant variability in the mechanical performance of carbonated cement composites [65]. The idea of controlling the polymorphs of $CaCO_3$ in carbonated cement composites is a relatively new concept, however, this approach has been widely used to produce bio-inspired materials [79]. The stabilization of metastable ACC, aragonite, and vaterite polymorphs by living creatures is demonstrated through studies on the mechanisms of biomineralization [80]–[82]. A number of organic molecules have been explored that can control the nucleation, crystal growth, and polymorphic selection of the $CaCO_3$ in biominerals [83], [84]. It has also been demonstrated that this method of using organic molecules to regulate the crystallization of inorganic $CaCO_3$ results in "organic-inorganic" hybrid phases that are incredibly strong, resilient, and resilient [85]. Amino acids, including aspartic acid [81], [86]–[88], serine [84], arginine [89] and glutamic acid [90] showed the ability to control the crystallization of $CaCO_3$. Several of these amino acids have been successfully utilized to improve the performances of carbonated wollastonite composites[91].

8

In addition to amino acids, polyacrylic acid can be an alternative since it also showed potential to control the crystallization of $CaCO_3$ [92]. From this motivation, the idea of incorporating biomimetic molecules into g-C2S and b-C2S to enhance the properties of carbonation was considered.

1.5 Research goals

To conduct these studies, a list of previously used biomimetic molecules had been chosen based on their different chain length and chemical structures. They are shown in **Table 1.1**.

Table 1.1: List of biomimetic molecules used in this study

Structures of the biomimetic molecules	
M-1	
M-2	
M-3	
M-4	

Based on the hypotheses and motivation, the research goals are –

(i)   By controlling the crystallization of $CaCO_3$, it can potentially reduce the carbonation damage of calcium silicate hydrates (C-S-H) [Part 1: Chapter 2 and Chapter 3].

(ii)   By controlling the crystallization of $CaCO_3$, properties of carbonation cured low calcium silicate cements can be enhanced [Part 2: Chapter 4 and Chapter 5].

Chapter 2: Reducing carbonation degradation and enhancing elastic properties of calcium silicate hydrates using biomimetic molecules

2.1 Research objectives

The significance of sustainable cementitious materials, utilizing supplementary cementitious materials (SCMs) and Ca-rich alkali-activated compounds, as eco-friendly alternatives to conventional Portland cement (OPC), owing to their reduced carbon footprint. These sustainable materials, primarily comprised of C-S-H or C-A-S-H binding phases and devoid of $Ca(OH)_2$, are more vulnerable to atmospheric CO_2-induced deterioration. CO_2 permeates the cementitious composites, triggering reactions with water and leading to the formation of bicarbonate ions. This process results in decalcification and polymerization of binding phases, ultimately giving rise to calcite. The formation of calcite, with a lower molecular volume than C-S-H, leads to increased matrix porosity, reduced compressive strengths, carbonation shrinkage, and heightened susceptibility to reinforcement corrosion. The augmented matrix porosity facilitates the penetration of detrimental chloride and sulfate ions, further undermining durability. One approach to mitigate carbonation damage is to control the polymorphs of precipitated $CaCO_3$ particles. Different polymorphs, such as calcite, aragonite, vaterite, and amorphous calcium carbonate (ACC), can form during carbonation. Of these, ACC, being highly soluble, can reduce carbonation extent and damage in cementitious matrices. Biomimetic molecules, like M-1 and M-2, can stabilize these polymorphs through organic-inorganic hybrids. The study explores the role of these biomimetic molecules, particularly M-1 and M-2, in controlling $CaCO_3$ crystallization during C-S-H carbonation. These molecules mimic biomineralization processes and can interact with different functional groups, making them promise for manipulating C-S-H properties. The study's

primary objective is to assess the efficacy of these biomimetic molecules in resisting atmospheric carbonation degradation of C-S-H.

The specific research objectives of this study are: (i) to investigate the effects of biomimetic molecules if they can reduce or prevent carbonation degradation of C-S-H by forming the meta stable calcium carbonates, (ii) to understand how biomimetic molecules can play role to enhance the elastic properties of C-S-H.

2.2 Materials and methods

2.2.1 Raw materials

Commercially available calcium nitrate ($Ca(NO_3)_2 \bullet 4H_2O$) and sodium silicate ($Na_2SiO_3 \bullet 9H_2O$) were used as the raw ingredients to synthesize pure C-S-H. For synthesizing biomimetic molecule-modified C-S-H, high purity grade biomimetic molecules, M-1 and M-2 were purchased from VWR and 10% dosage (by weight percentage of C-S-H) was chosen to prepare M-1 and M-2 modified C-S-H. Figure 2.1 displays the schematic drawing of the C-S-H structure.

(a)
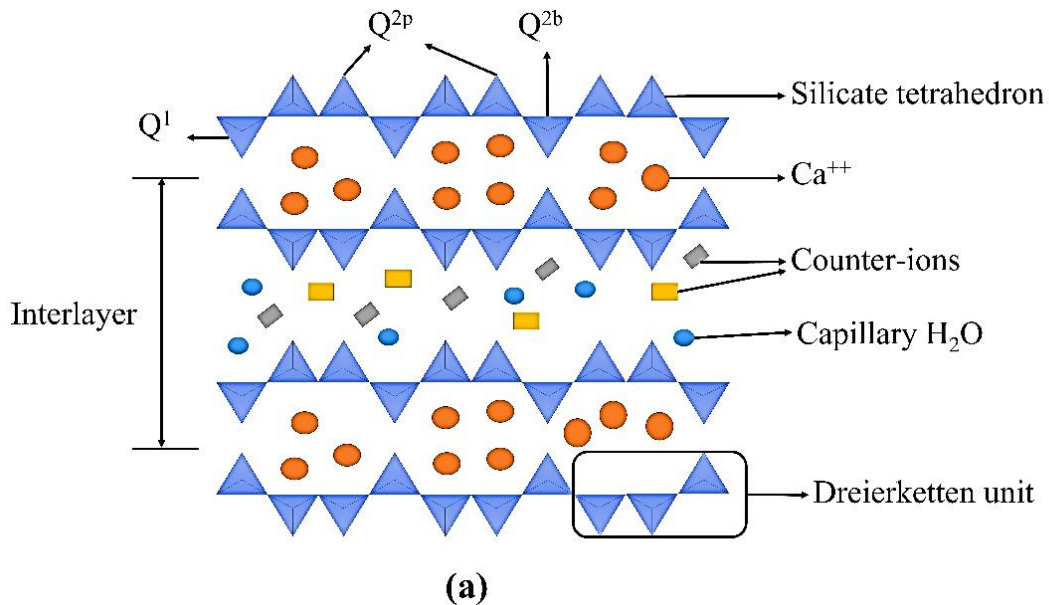
Figure 2.1: (a) schematic CSH structure

12

2.2.2 CSH synthesis

Previously published studies [93], [94] were followed to synthesize pure and biomimetic molecule-modified C-S-H. **Figure 2.2** shows the steps of laboratory synthesis of C-S-H (with and without biomimetic molecules). For the pure CSH preparation, at first, 250 ml deionized water was poured into a beaker. The water was boiled to get rid of the air bubbles and dissolved CO_2 gas. Next, the temperature of the solution was lowered to 50°C. Sodium hydroxide (NaOH) was then added to the water to increase the pH to 11.5. After that, 10 g of calcium nitrate salt was dissolved in the water. Meanwhile, sodium silicate salt was dissolved in 250 ml of deionized water and poured in a separate beaker. The amount of sodium silicate salt was calculated based on the calcium to silica (C/S) ratio of 1.5. Next, the calcium nitrate solution beaker was placed on the hotplate magnetic stirrer. The stirrer was rotated at 450 rpm and the temperature was set at 50°C. After that, the sodium silicate solution was added drop by drop to the calcium nitrate solution with a burette. Once the addition of sodium silicate solution was done, the beaker was kept on the hotplate magnetic stirrer, maintaining the same rotation and temperature for 48 h. After 48 h, the CSH gel was filtered and then put inside the oven at 50°C for 24 h. After that, the CSH gel was dried and formed solid chunks. The chunks were ground using mortar-and-pestle. All the above activities were performed in a nitrogen gas purging environment to avoid carbonation degradation of the synthesized CSH.
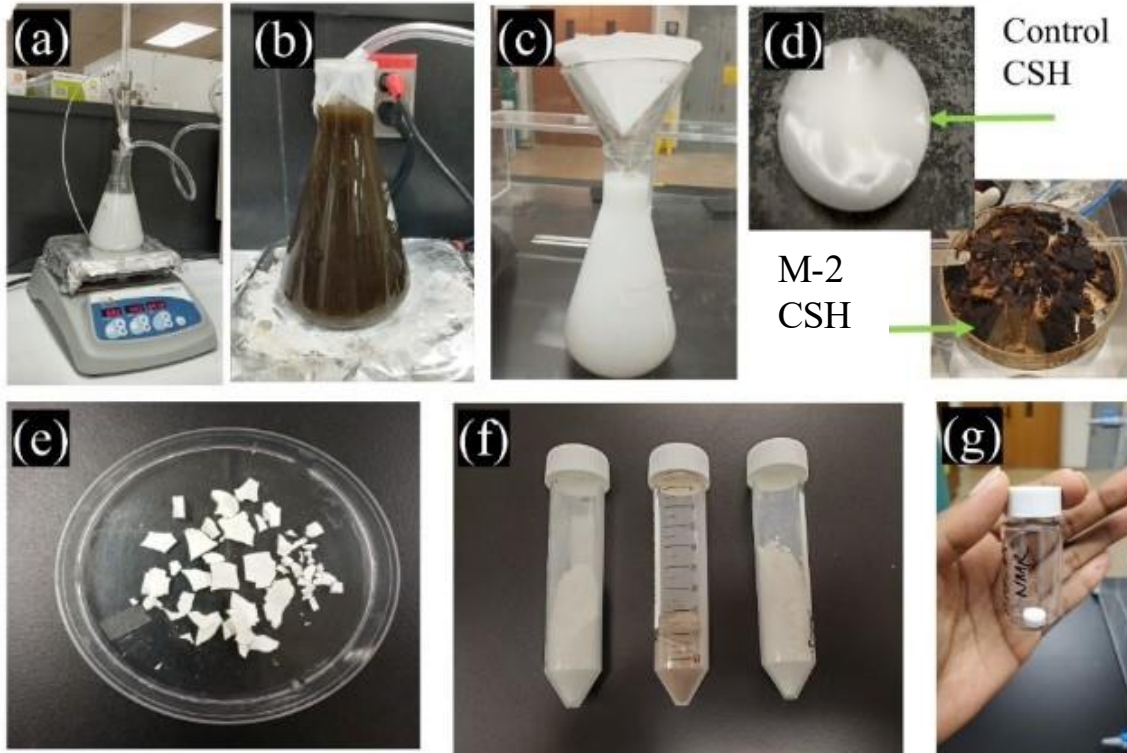
Figure 2.2: (a) Sodium silicate solution being added to calcium nitrate solution with burette; (b) calcium nitrate and sodium silicate solution kept on hotplate for 48 h; (c) filtering out the C-S-H gel; (d) C-S-H gel (e) oven dried C-S-H; (f) ground synthetic C-S-H (from left: pure C-S-H, M-2 modified C-S-H and M-1 modified C-S-H); (g) prepared pellet

A 10% dosage (by weight percentage of CSH) of M-1 and M-2 was chosen for the biomimetic molecules modified CSH preparation. This 10% dose was selected based on our preliminary study using portlandite carbonation. In this case, biomimetic molecules were added to the boiled pH 11.5 water, prior to adding the calcium nitrate salt. The solution was mixed for approximately 2 minutes to ensure the biomimetic molecules were visibly dissolved in the solution. After that, the calcium nitrate salt was added to the solution. All other steps remained the same as those for the pure CSH. Worth noting, both pure CSH and M-1 modified CSH had a whitish color. However, M-2 modified

CSH had darkish color. The conversion of dopamine hydrochloride to M-2 is known to be responsible for the dark grey appearance [64].

2.2.3 Sample preparation

The obtained pure and modified C-S-H were in powder form. These powders were used to prepare pellets of approximately 2 mm thickness and 10 mm diameter using a pellet press by applying a 5 MPa load. These pellet C-S-H samples were then subjected to accelerated carbonation using a commercially available carbonation chamber. The chamber was operated to maintain a 4% CO_2 concentration at 25°C and 75% relative humidity (RH). The pellet samples were extracted from the carbonation chamber after certain intervals as listed in Table 2.1. Since most of the characterization tests required powder samples, the collected carbonated pellets were ground using a mortar-and-pestle inside a glove box. The collected powder samples were preserved inside a vacuum chamber, ensuring an airtight environment and maintaining 11% RH controlled by a LiCl salt solution. Table 2.1 presents the test matrix for the various carbonation durations of the C-S-H pellets. As observed, the actual C/S ratios were lower than the target 1.5. Such reduced C/S ratios were expected as the efficiency of the C-S-H synthesis approach is not 100%. Below are the list experiments that were performed to achieve the research goals.

Table 2.1: Matrix of experiments before and after carbonation of the samples

Tests	Carbonation duration
Transmission Electron Microscopy (TEM)	0 h, 168 h
Thermogravimetric analysis with mass spectroscopy (TGA-MS)	168 h, 28 days
Nuclear Magnetic Resonance (NMR)	0 h, 168 h, 28 days
Fourier Transform Infrared Spectroscopy (FTIR)	0 h, 6 h, 24 h, 72 h, 168 h, 28 days

Nanoindentation	0 h, 168 h, 28 days
Scanning electron microscopy (SEM)	168 h, 28 days
X-Ray diffractions (XRD)	0 h, 28 days

2.2.4 Test methods

For TEM images, the CSH (either immediately after synthesizing or carbonated) powder was dispersed into an isopropanol solution. The solution was then ultrasonicated for 10 minutes using a commercially available sonicator (Cole-Parmer 8890). The samples were placed on a lacey carbon 300 mesh gold grid (Ted Pella Inc, USA) using a dropper. The images were collected using a Hitachi H-9500 transmission electron microscope and the operating voltage was 300 kV.

Solid state magic angle spinning nuclear magnetic resonance was performed on the samples to characterize the local atomic structure of ^{29}Si. The NMR test was performed on 0 h, 24 h and 168 h carbonated samples. All the ^{29}Si solid-state NMR experiments were conducted at 7.05 T on a Varian Unity Inova 300 MHz spectrometer at the SCS NMR Facility of the University of Illinois at Urbana-Champaign, operating at a resonance frequency of v_0 (^{29}Si) = 59.6 MHz, at room temperature. A Varian/Chemagnetics 7.5 mm double-resonance APEX HX magic-angle spinning (MAS) probe was used for all MAS experiments under a spinning rate of 4 kHz and TPPM 1H decoupling. All samples were finely ground and packed into 4 mm o.d. standard zirconia rotors (typically around 210-580 mg). Experimental silicon chemical shift referencing, pulse calibration and setup were done using powdered octakis (trimethylsiloxy) silsesquioxane (Q8M8), which has a chemical shift of 11.45 ppm, relative to the primary standard, TMS at 0 ppm. The ^{29}Si pulse width used was 1.5 µs, corresponding to a 45-degree pulse. A recycle delay of 30 s was used and 1920 scans were acquired for each sample.

The Fourier-Transformed Infrared (FTIR) spectra of the powder samples were collected using the Attenuated Total Reflection (ATR) mode with 4 cm^{-1} resolution and 32 scans for each sample. Signal to noise ratio was lower than 3:1. FTIR test was conducted on 0 h, 6 h, 24 h, 72 h, 168 h and 28 days carbonated samples.

TGA was coupled with a mass spectrometer (MS) for 168 h and 28 days carbonated samples. This coupled TGA-MS system enabled the separation and identification of any volatile elements coming off the sample during the heating process. In this case, TGA was performed using a Netzsch STA 449 F3 Jupiter Simultaneous Thermal Analysis (STA) instrument. All samples were measured under ultra-high purity helium gas (flow of 50 ml/min). The temperature was increased at a rate of 10ºC/min, and gases were transferred to the GC/MS instrumentation via a heated (250ºC) transfer line. An Agilent Technologies 7890A GC system equipped with a non-polar capillary column (Agilent J&B HP-5 packed with [5%-Phenyl-methylpolysiloxane]) coupled with a 5975 MSD spectrometer was used for the analyses of the gases released from the samples. A gas injection was triggered every minute (60 s) from the beginning of the heating cycle, and 0.25 ml of gas was sampled from the gases released by the compound and carrier gas (He).

For grid nanoindentation, 0 h, 168 h and 28 days carbonated samples were chosen. Because of the mirror like finishing of the pellet press die set, the CSH pellets could be used for nanoindentation measurements without any further surface preparation of the samples. The load function had three segments: (i) loading from zero to maximum load in the span of 5 s, (ii) holding at the maximum load for 5 s, (iii) unloading from maximum to zero load within 5 s. Since the depth of the indentations should also be small enough to determine the mechanical properties of the individual microscopic phases (i.e. indentation depth $\ll$ characteristic size of each microscopic phases) [95], a maximum of 300 µ-N force was selected for the SNI technique during this study. The average

indentation depth for this load function was around 100-300 nm for a 30 μm × 30 μm area. The elastic moduli were determined from the load-depth plots using the Oliver and Pharr method [96]. Nanoindentation tests were performed using a Hysitron Triboindenter UB1 system (Hysitron Inc. Minneapolis, USA) fitted with a Berkovich diamond indenter probe. The tip area function was calibrated by performing several indents with various contact depths on a standard fused quartz sample. In all cases, a surface RMS roughness lower than 80 nm (measured with the Berkovich tip) was detected over an area of 60 μm × 60 μm.

The microstructures of 168 h and 28 days carbonated samples were evaluated using a Hitachi 3000N SEM. The instrument was operated in high vacuum mode with a 30 kV accelerated voltage and a working distance of about 10 mm. The cement paste sample was coated with platinum (Pt) before capturing the SEM images.

X-ray diffraction patterns of the paste samples were collected with a Bruker D-500 spectrometer using Cu Kα radiation (40 kV, 30 mA). Diffraction patterns were obtained for a 2θ range of 5° to 60° with a step size of 0.03 (2θ) per second. XRD patterns were only obtained to ensure the quality of the synthesized CSH.

2.3 Results and discussions

2.3.1 Characteristics of biomimetic molecules modified C-S-H

The chemical environment of ^{29}Si is generally expressed as Q^n in silicate minerals, where Q denotes the silicon atom bonded tetrahedrally to four oxygen atoms and the subscript n refers to the number of the other $[SiO_4]^{4-}$ attached to the SiO_4 tetrahedron being investigated [97], [98]. **Figure 2.3** represents the ^{29}Si NMR spectra of the freshly prepared pure C-S-H and biomimetic-modified C-S-H. Based on the literature [99], [100], the ^{29}Si NMR peaks were assigned as below:

end groups and dimers (Q^1): -79.7 ppm; the bridging sites (Q^2_b): -82 pp; and pairing sites (Q^2_p): -85 ppm. The pure C-S-H was found to contain a relatively high intensity of Q^2 compared to that of Q^1. Such a high Q^2/Q^1 ratio is expected for C-S-H synthesized with a low C/S ratio [99]. The actual C/S ratios of the synthesized samples were significantly lower than the target ratio of 1.5, thus resulting in relatively high intensity for Q^2 in all the CSH samples. In the M-2 modification, the intensities for Q^1 and Q^3 present in the CSH were increased. Therefore, the addition of M-2 increased the non-uniformity in CSH structure. The effects of M-1 addition were similar to those of M-2. Additionally, M-1 modified CSH showed the highest intensity of Q^0 species. Considering that the addition of biomimetic molecules increased the intensities for both low polymerized (Q^0, Q^1) and highly polymerized (Q^3) units, it was not possible to conclude whether such molecules increase or decrease the overall chain length of the CSH.
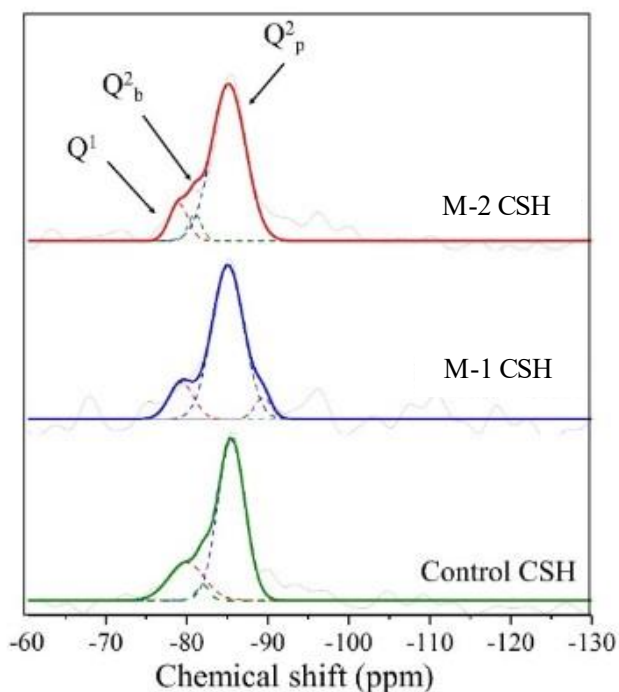
Figure 2.3: ^{29}Si MAS NMR spectra of pure and modified C-S-H at 0 h carbonation period

Figure 2.4 shows the TEM images of the pure C-S-H and biomimetic-molecule modified C-S-H nanostructures. The images were taken at two different magnification levels: 100 nm and 50 nm. Pure C-S-H was found to have lath or globule-like structure. Such morphology of CSH matches previous observations [101]. Interestingly, the addition of biomimetic molecules had distinct effects on the morphology of the CSH. The synthetic CSH with 10% M-2 showed a foil-like morphology. Additionally, the CSH deposition appeared to have become denser due to the addition of M-2. Such an effect was more prominent in the case of the M-1 modified CSH. Specifically, the TEM image of the M-1 modified CSH showed the formation of randomly oriented needle-like shapes. The molecules interacted differently due to different chain length and charges. The M-2 has a longer chain length than the M-1.
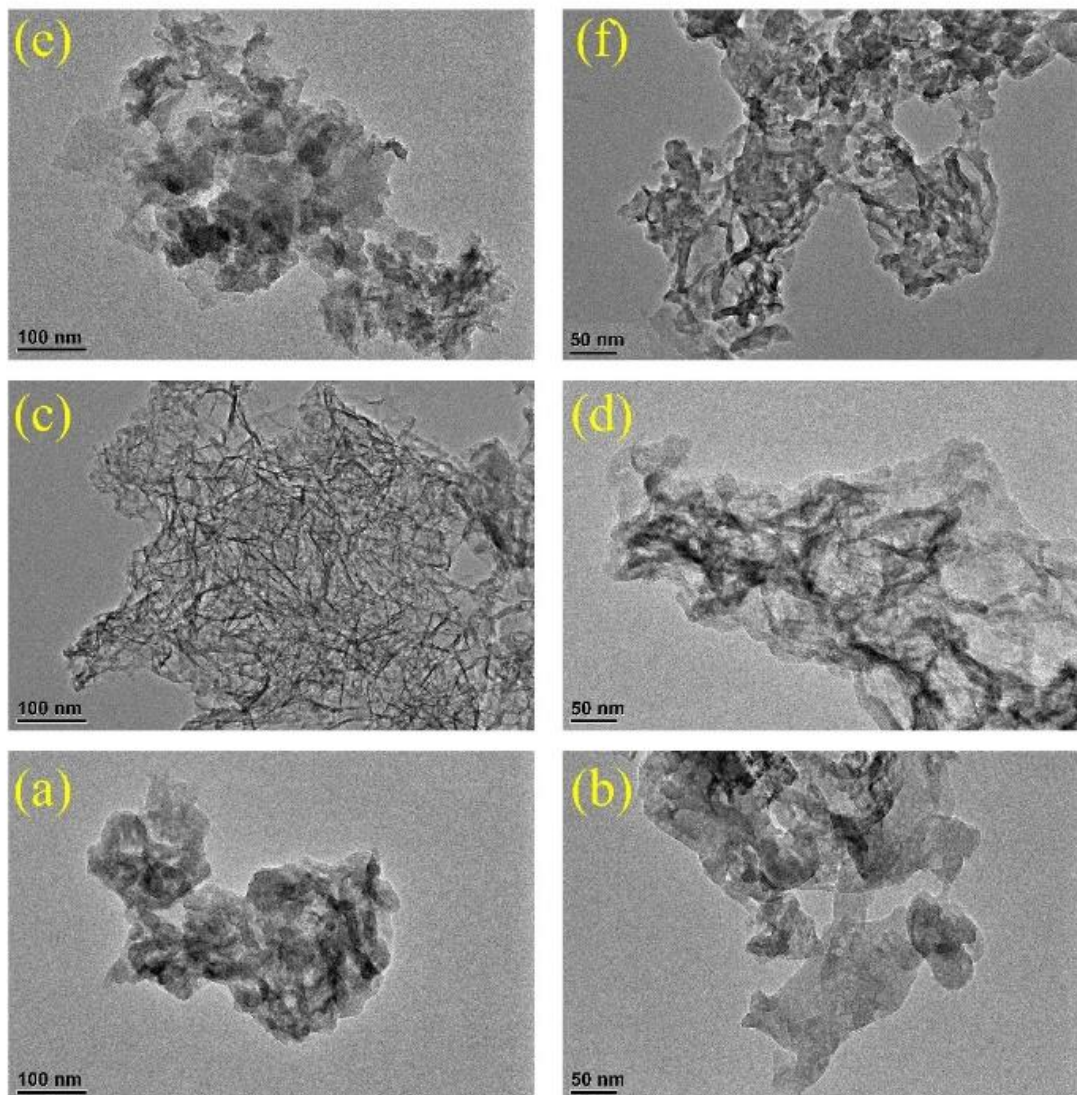
Figure 2.4: TEM image of (a) Control CSH (100 nm), (b) Control CSH (50 nm), (c) M-1 - CSH (100 nm), (d) M-1 - CSH (50 nm), (e) M-2 - CSH (100 nm), and (f) M-2 - CSH (50 nm)
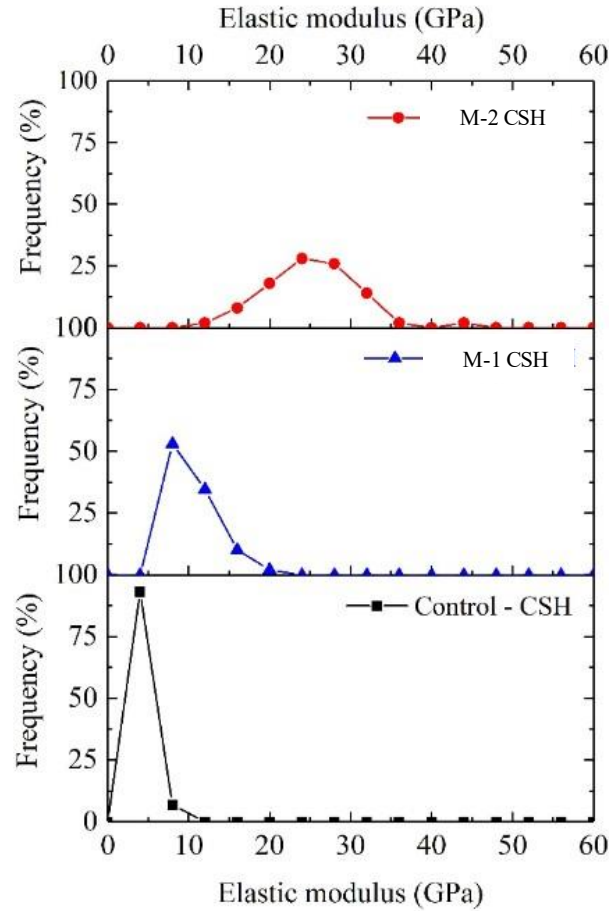
Figure 2.5: Percent frequency vs elastic modulus of (a) pure C-S-H (b) M-1 modified C-S-H, (c) M-2 modified C-S-H without any carbonation.

The compacted C-S-H pellets were subjected to nanoindentation over two different 30 μm × 30 μm areas in a grid pattern resulting in a total of 120 indentations per sample. Based on the results from those 120 indentations, the frequency distribution of the elastic modulus of the pure C-S-H(control), M-2 modified C-S-H, and M-1 modified C-S-H are given in **Figure 2.5**. The pure C-S-H was found to have a mean modulus of 3 GPa. This value exactly matches a recently reported measurement of a modulus of C-S-H with a C/S ratio of 1.0 [102]. M-2 modified C-S-H showed a higher elastic modulus of 25 GPa which is around 8 times higher than the pure C-S-H. Worth noting, M-2 is also well known for its adhesive properties [103]. The self-polymerization of

dopamine hydrochloride to M-2 in an alkaline environment creates a polymer network with strong adhesive properties [103]. We suggest that due to this adhesive nature, the M-2 modification of C-S-H resulted in the observed increase in the modulus of C-S-H. The M-1 modified C-S-H was found to have an elastic modulus of around 9 GPa which is around 3 times higher than the control sample. This increased modulus could be due to the formation of higher amounts of Q^3 as observed from the ^{29}Si NMR spectra. Considering the above results, it is interesting to note that the addition of biomimetic molecules can significantly enhance the elastic properties of C-S-H. These findings point toward a new approach for nano-engineering cement-based materials for superior mechanical performance. However, it is important to note that a previous study by Kamali and Ghahremaninezhad [104] reported that the modification of CSH by biomolecules reduced the elastic modulus of this phase. In that study [104], the used biomimetic molecules were arginine, leucine, glutamic acid, albumin, and hemoglobin. Therefore, the type of organic molecules used plays an important role in whether the elasticity of the modulus of CSH is enhanced or not. Based on the current findings, it can be suggested that biomimetic molecules with distinct Ca^{2+} binding properties can enhance the modulus of CSH. However, additional investigations are required to confirm this observation.

2.3.2 Effectiveness of biomimetic molecules to resist carbonation.

The ^{29}Si NMR spectra of the 168 h and 28 days carbonated C-S-H samples are given in **Figure 2.6** **(a)** and **(b)**, respectively. After 168 h of accelerated carbonation at a 4% CO_2 concentration, the pure C-S-H batch contained only Q^3 (around -100 ppm) and Q^4 (around -112 ppm) species. The complete absence of Q^1 and Q^2 species confirmed that the original C-S-H structure was fully deteriorated and had formed a highly polymerized 3-dimensional silica gel network. The NMR spectra for the control batch remained similar after 28 days of carbonation (contained only Q^3 and

Q^4). Interestingly, in the case of the M-1 and M-2 modified batches, the original C-S-H structure containing Q^2 species were retained after 168 h of carbonation, and there was no Q^4 formation. After 28 days of carbonation, minor peaks corresponding to Q^3 and Q^4 species were observed, even though the intensities of Q^1 and Q^2 remained prominent. Accordingly, the M-2 and M-1 modifications were successful in significantly lowering the carbonation degradation of C-S-H.
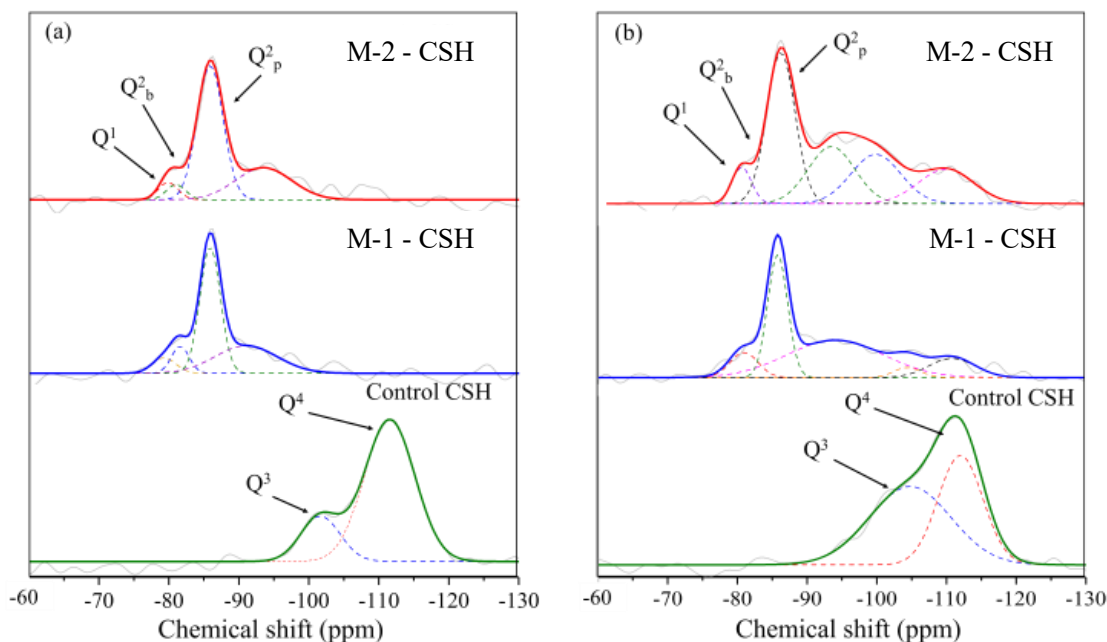
Figure 2.6: ^{29}Si MAS NMR spectra of pure and modified C-S-H at (a) 168 h and (b) 28 days of carbonation

However, the chemical shift corresponding to Q^3 were in a lower range (- 90 to -100 ppm) for the modified CSH batches compared to those observed in the control batch (-104 ppm). This indicates the difference in the environment of the Q^3 species formed during the carbonation of CSH with and without the presence of biomimetic molecules and can correspond to the formation of organic-inorganic hybrid phases (CSH-organic molecule-$CaCO_3$) as hypothesized earlier.

The TEM images of the CSH samples after 168 h of carbonation are given in **Figure 2.7**. In the case of the carbonated CSH batch, the presence of a crystalline phase within the disordered matrix is visible (**Figure 2.7(a)**). This indicates the intermixing of $CaCO_3$ crystals in the carbonated CSH matrix. Such formation of a crystalline phase within the disordered matrix due to the carbonation of CSH has been reported in the past [105]. In the zoomed-in version (**Figure 2.7(b)**), small globules with dense borders or periphery were observed. Such globules can be considered as the characteristic morphology of polymerized silica gel. In the case of M-2 and M-1 modified CSH, formation of such globules was not visible. It was observed that even after carbonation, the original foil-like morphology was retained for these batches, thus confirming other experimental observation that the biomimetic molecules modified CSH were able to retain the original molecular arrangements even after carbonation.
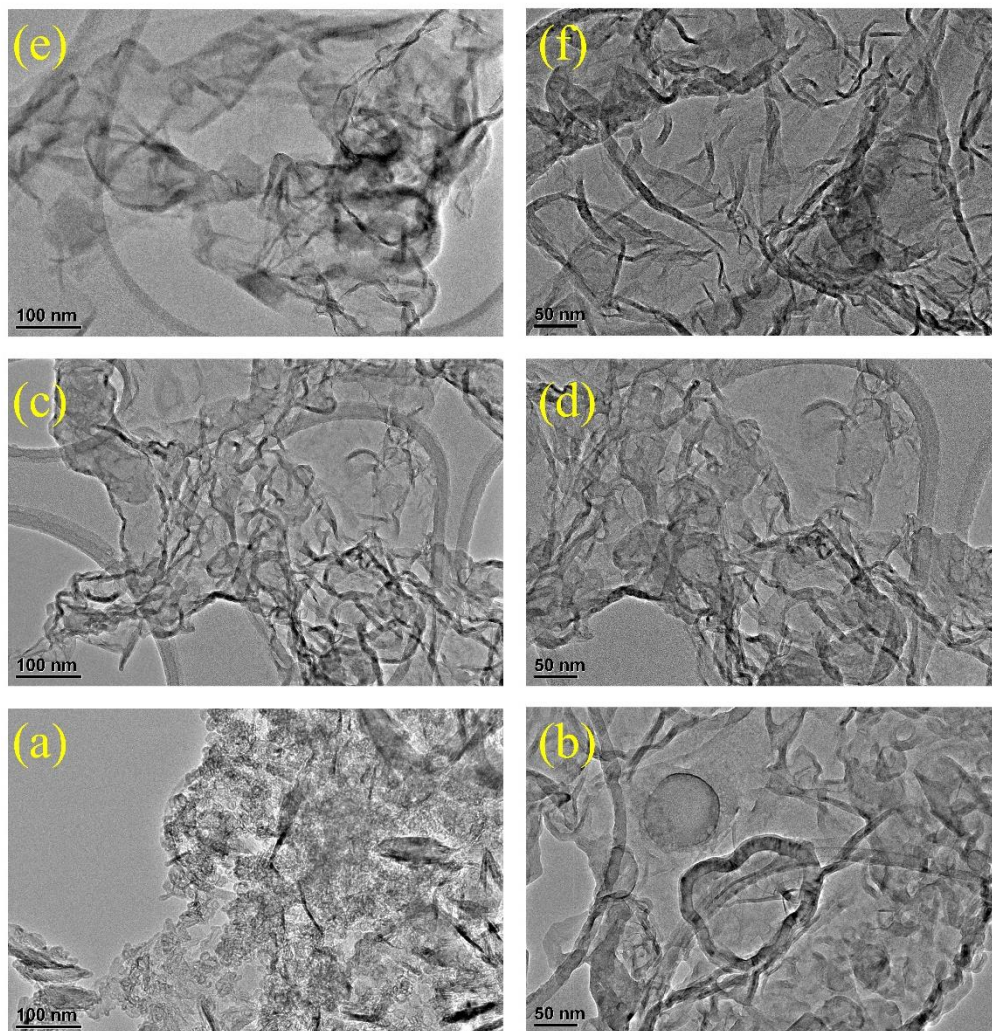
Figure 2.7: TEM image of (a) pure CSH (100 nm), (b) pure CSH (50 nm), (c) M-1 modified CSH (100 nm), (d) M-1 modified CSH (50 nm), (e) M-2 modified CSH (100 nm), and (f) M-2 modified CSH (50 nm) after 168 h of carbonation period.

ATR-FTIR measurements has proven to be a highly valuable tool to monitor the polymerization of CSH [106] as well as the formation of various $CaCO_3$ polymorphs [58] during the carbonation reaction. In this work, FTIR spectra were collected from the carbonated CSH samples at certain intervals as shown in **Figure 2.8**. The FTIR spectra for CSH exhibit a broad absorption between 800 cm^{-1} and 1200 cm^{-1} which corresponds to the asymmetrical stretching vibration (v_3) of the Si-

O bond present in silicate [106]. Based on the literature [107], the various polymerized silicate units in CSH were assigned as followings: the 960 ~ 980 cm^{-1} peaks are the Q^2 units, the 1050 ~ 1080 cm^{-1} peaks are the Q^3 units, and the 1100 ~ 1200 cm^{-1} are the Q^4 units. The $CaCO_3$ polymorphs can be identified by studying the asymmetrical stretching vibration (v_3), the out-of-plane bending (v_2), and the in-plane bending (v_4) of the CO_3^{2-} bond in the ranges of 1300 ~ 1500 cm^{-1}, 800 ~ 900 cm^{-1} and 700 ~ 750 cm^{-1}, respectively [58] [108].

With increased carbonation duration, the asymmetrical stretching vibration (v_3) of CO_3^{2-} started forming at around 1420 cm^{-1} in the pure CSH sample (**Figure 2.8(a)**). Additionally, sharp peaks at around 872 cm^{-1} and 711 cm^{-1} were also formed. These are characteristics peaks of calcite [58][109], [110]. However, the minor peaks of out-of-plane bending at 858 cm^{-1} and in-plane bending at 700 cm^{-1} indicate the presence of a small amount of aragonite in the control batch after 168 h of carbonation. Additionally, the in-plane bending peak at around 745 cm^{-1} also represents the formation of vaterite in these samples. Regardless, the characteristic peaks of calcite were most prominent in the control batch indicating that these samples primarily formed calcite but contained small amounts of vaterite and aragonite after 168 h of carbonation curing. The 28 days carbonated CSH samples also primarily contained the characteristic peaks for calcite (1410 cm^{-1}, 873 cm^{-1}, and 712 cm^{-1}). This indicates that the initially formed vaterite and aragonite were converted to stable calcite polymorph in the case of the pure CSH carbonated sample.

The FTIR spectra of the M-2 modified, and M-1 modified CSH samples before and after carbonation were very similar (**Figure 2.8**(b) and (**c**)). Unlike the pure CSH sample, the asymmetrical stretching vibration (v_3) of CO_3^{2-} bond started forming a split peak at around 1350 cm^{-1} and 1390 cm^{-1}. Such split peaks are the characteristic of ACC as well as vaterite [110], [111]. The formation of out-of-plane and in-plane bending peaks at around 834 cm^{-1} and 744 cm^{-1},

respectively, in these samples also indicate the formation of vaterite in the biomimetic molecules modified CSH after carbonation. Unlikely the pure CSH samples, the characteristics FTIR peaks for ACC and vaterite were found to persist in the biomimetic-molecule modified CSH samples even after 28 days. Accordingly, it can be postulated that the presence of M-1 and M-2 stabilized the formation of ACC and vaterite in the carbonated CSH samples.
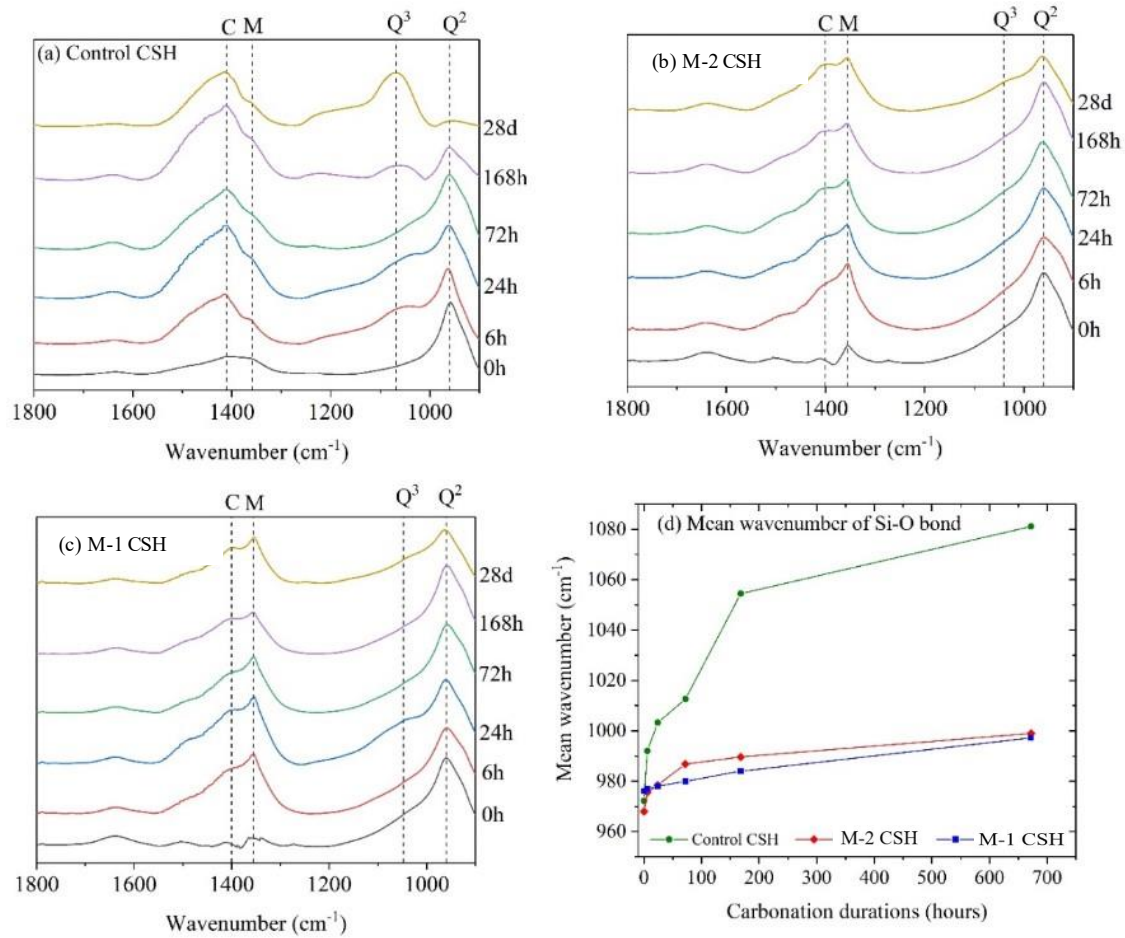
Figure 2.8: FTIR spectra of (a) pure C-S-H; (b) M-2 modified C-S-H; (c) M-1 modified C-S-H at different carbonation periods [C: calcite and M: metastable calcium carbonate]; (d) mean wavenumber of the silica tetrahedron polymerization chain at different carbonation periods

To understand the carbonation induced polymerization of C-S-H, the asymmetrical stretching vibration (v_3) of the Si-O bond formed in the range of 900 cm^{-1} to 1200 cm^{-1} was analyzed. As observed in **Figure 2.8(a)**, the control batch initially had an asymmetrical stretching vibration (v_3) of Si-O bond at around 960 cm^{-1} which is characteristic of the C-S-H structure. With increased carbonation duration, a peak at around 1100 cm^{-1}, corresponding to the Q^3 species, started forming. After 168 h of carbonation, the carbonated C-S-H sample contained primarily Q^3 and Q^4 peaks, in addition to Q^2 peaks. However, after 28 days of carbonation, only the absorption bands corresponding to Q^3 and Q^4 were visible, indicating the complete molecular arrangement of C-S-H was damaged and formed a highly polymerized silica gel network. This observation also matches the finding of the ^{29}Si NMR spectra. In the case of the modified C-S-H samples, the original Q^2 structure of C-S-H was retained even after 28 days of carbonation, thus, corroborating the findings of ^{29}Si NMR, that the presence of biomimetic molecules was able to aid C-S-H in resisting carbonation-induced polymerization.

To obtain a semi-quantitative comparison, the FTIR absorption peak corresponding to the Si-O bond in the range of 900-1200 cm^{-1} was deconvoluted to get the mean wavenumber. The deconvolution method was presented in a previous publication [106]. The absorption bands below 900 cm^{-1} wavenumbers were not considered in the calculation to avoid the effect of the C-O bond which has an absorption band at around 870 cm^{-1}. The mean wavenumbers for the different C-S-H batches along with their carbonation durations are presented in **Figure 2.8(d)**. From this plot, it can be seen that the accelerated carbonation only slightly changed the chain silicate structure present in the M-1 and M-2 modified CSH samples. The original molecular arrangements of CSH were retained even after 28 days. However, in the case of the pure CSH sample, the conversion of CSH to the polymerized 3D network for silica gel happened within 168 h.

The TGA-MS plots of CSH carbonated for 168 h and 28 days are presented in **Figure 2.9** and **Figure 2.10**, respectively. Nearly all the CSH showed gradual weight loss due to the release of chemically bound water within the temperature range of 100°C to 600°C, and the release of CO_2 due to the decarbonation of $CaCO_3$ within the temperature range of 200°C to 800°C. As suggested previously, the gradual weight loss due to the decarbonation is primarily associated, including vaterite and ACC [58]. The decomposition (recrystallization to a stable phase) of ACC occurs in the temperature range of 170°C to 350°C, depending on the particle size and pH [112], [113]. In the case of vaterite, recrystallization occurs at around 450°C and exhibits multiple stages [114]. Based on this literature information, we mark four stages in the CO_2 mass spectra of the carbonated CSH samples and assign those stages as follows, I: recrystallization of ACC, II and III: recrystallization of vaterite, and IV: decomposition of calcite. Aragonite was not observed in these samples using XRD (see supplementary data). From **Figure 2.9(a)**, it can be observed that the carbonated control CSH contained vaterite, ACC, and calcite after 168 h of carbonation. The CO_2 spectra for M-1 and M-2 were similar to that of the control batch, except the intensity corresponding to vaterite was low. Based on the TGA-MS plots, the weight loss associated with the CO_2 release was further calculated and presented in **Figure 2.9(d)**. It can be observed that due to carbonation, pure CSH was able to sequester around 20% CO_2. On the other hand, the CO_2 sequestration in the M-1 and M-2 modified CSH samples was around 11% and 15%, respectively. After 28 days of carbonation, the CO_2 release corresponding to ACC (stage I) was not observed in the control CSH batch [**Figure 2.10(a)**], but the intensity corresponding to vaterite was increased. In the case of the M-1 modified CSH, after 28 days of carbonation, the intensity of CO_2 spectra corresponding to ACC was increased, whereas, in the case of the M-2 modified CSH it remained the same as at 168 h. Accordingly, we suggest that while all the carbonated batches contained

vaterite and calcite, only the biomimetic molecules modified batches produced a stable form of ACC. It was further observed that after 28 days of carbonation, the CO_2 sequestered in the control batch and M-2 modified batch increased to 27% and 20%, respectively. On the other hand, the M-1 modified CSH did not show any increase in CO_2 sequestration capacity after 28 days of carbonation. Accordingly, M-1 modification was able to resist further carbonation of the samples after 168 h, and M-2 modification slowed down the carbonation rate compared to that of the control batch. Interestingly, the biomimetic molecules modified CSH samples were able to sequester CO_2 without deteriorating the original chain like structure of the CSH.
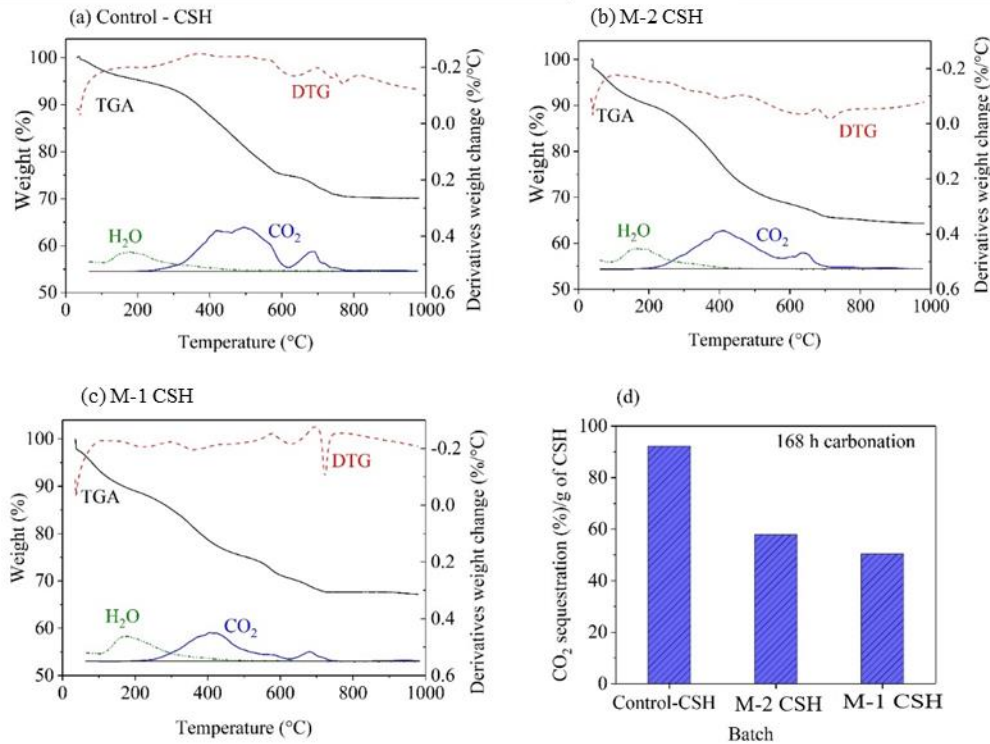
Figure 2.9: Thermogravimetric analysis of CSH after 168 h of carbonation
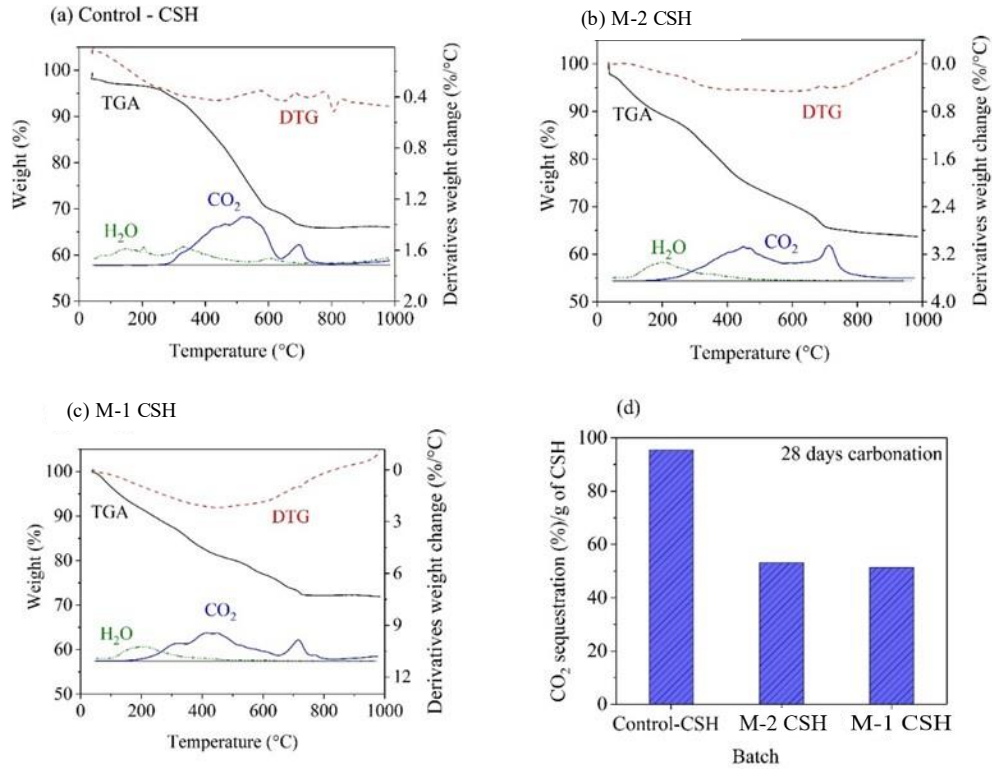
Figure 2.10: Thermogravimetric analysis of CSH after 28 days of carbonation

The frequency distribution of the elastic modulus in the C-S-H pellets after 168 h and 28 days of carbonation are presented in **Figure 2.11(a)** and **Figure 2.11(b)**, respectively. Considering the pure C-S-H batch, with an increased degree of carbonation, the average elastic modulus was observed to increase. This is expected considering calcite has a higher modulus compared to that of C-S-H.
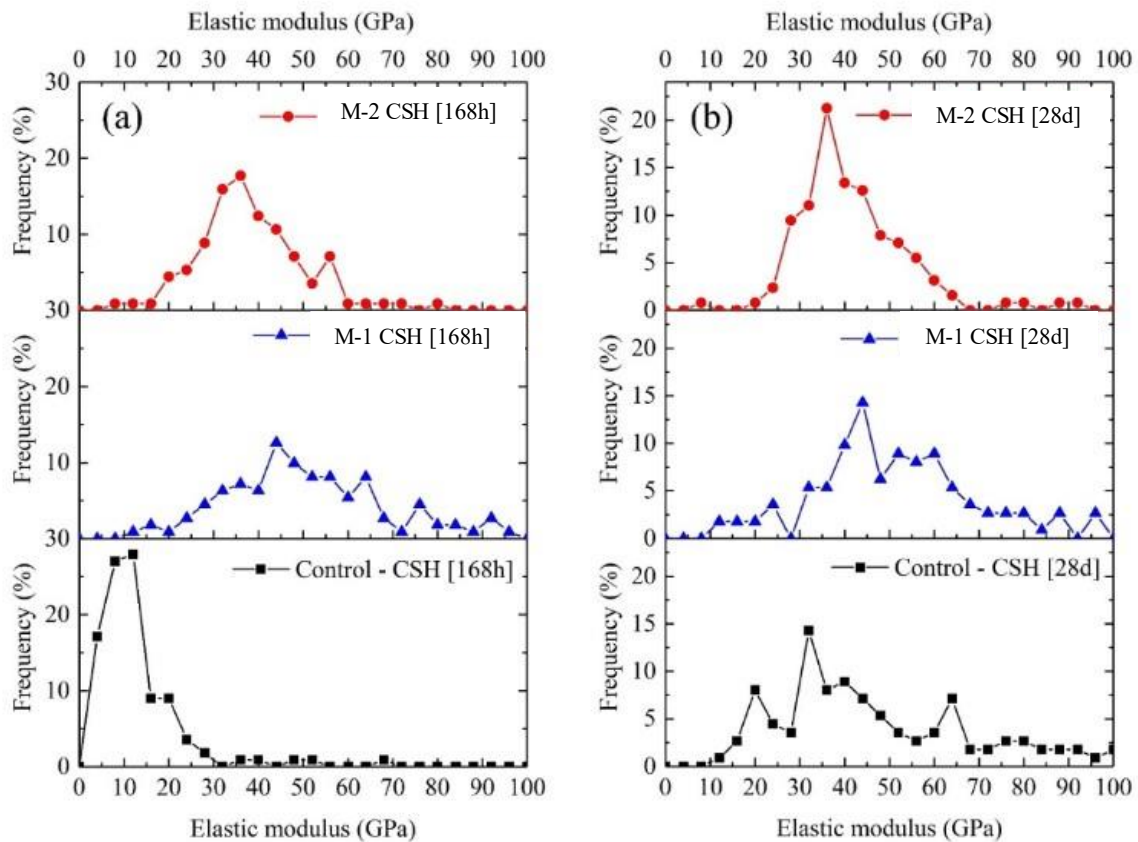
Figure 2.11: Percent frequency vs elastic modulus of control C-S-H, M-1 modified C-S-H, M-2 modified C-S-H at (a) 168 h and (b) 28 days of carbonation

It is postulated that after 168 h of carbonation, the pure CSH pellets consist of $CaCO_3$ crystals, remaining original CSH, and polymerized silica gel. Considering the combination of these phases, the average elastic modulus was increased to around 15 GPa (original CSH average was 3 GPa). The average modulus remains close to the previously reported value for the carbonated compact CSH disc [115]. At this stage, the pure CSH also contained vaterite and ACC, which may have also resulted in a lower modulus compared to those of calcite. However, after 28 days of carbonation, the formation of calcite evidently caused a significant increase in the modulus. Interestingly, considering the frequency distribution of the elastic modulus, the presence of three

distinct phases were clearly identifiable (as marked in **Figure 2.11(b)**). This indicates that the carbonated pure CSH pellet contained a mixture of these three phases. In contrast, in the M-2 modified CSH, the elastic modulus increased from 23 GPa to 36 GPa after 168 h of carbonation. Upon carbonation for 28 days, the average elastic modulus distribution shifted further to ~ 40 GPa. In the case of M-1 modified CSH, this increase in elastic modulus was significantly more prominent. Specifically, M-1 CSH had an average elastic modulus of 9 GPa before carbonation, which increased to 45 GPa after 168 h of carbonation. After 28 days of carbonation, the elastic modulus increased further to 55 GPa.

Worth noting, pure calcite crystals have an elastic modulus of around 60 to 70 GPa [116]. Therefore, the frequency distribution of the observed elastic modulus of the control batch can be statistically deconvoluted to three phases and assigned as follows: 20 GPa – remaining CSH and silica gel, 35 GPa – intermixed gel phase and calcite, and 65 GPa – calcite. In contrast, in the case of the M-2 modified batch, there weren't any separable phases observed in the frequency distribution after 28 days of carbonation. Specifically, the frequency distribution appeared to have a normal distribution with mean modulus of around 36 GPa. A similar pattern was observed in the case of the M-1 modified batch, except the mean modulus was higher (45 ~ 55 GPa). This observation further indicates the potential formation of a single hybrid phase, instead of separate microscopic phases.

The morphologies of the $CaCO_3$ crystals formed in the carbonated CSH are shown in **Figure 2.12**. Individual crystal sizes and shapes were visible in all the CSH batches [**Figure 2.12(a to f)**]. In the case of the control batch, $CaCO_3$ crystals were mostly embedded in the silica gel phase [**Figure 2.12(a, b)**]. However, sharp rhombohedral edges of calcite crystals were identifiable in the control batch. In contrast, in the cases of the M-1 modified samples, spherical ACC were visible [**Figure

2.12(c, d)]. On the other hand, M-2 batches were mostly found to contain vaterite plates. Based on

the several SEM images, it was apparent that M-1 and M-2 primarily stabilized ACC and vaterite,

respectively. However, both of the batches also found to contain calcite crystals.
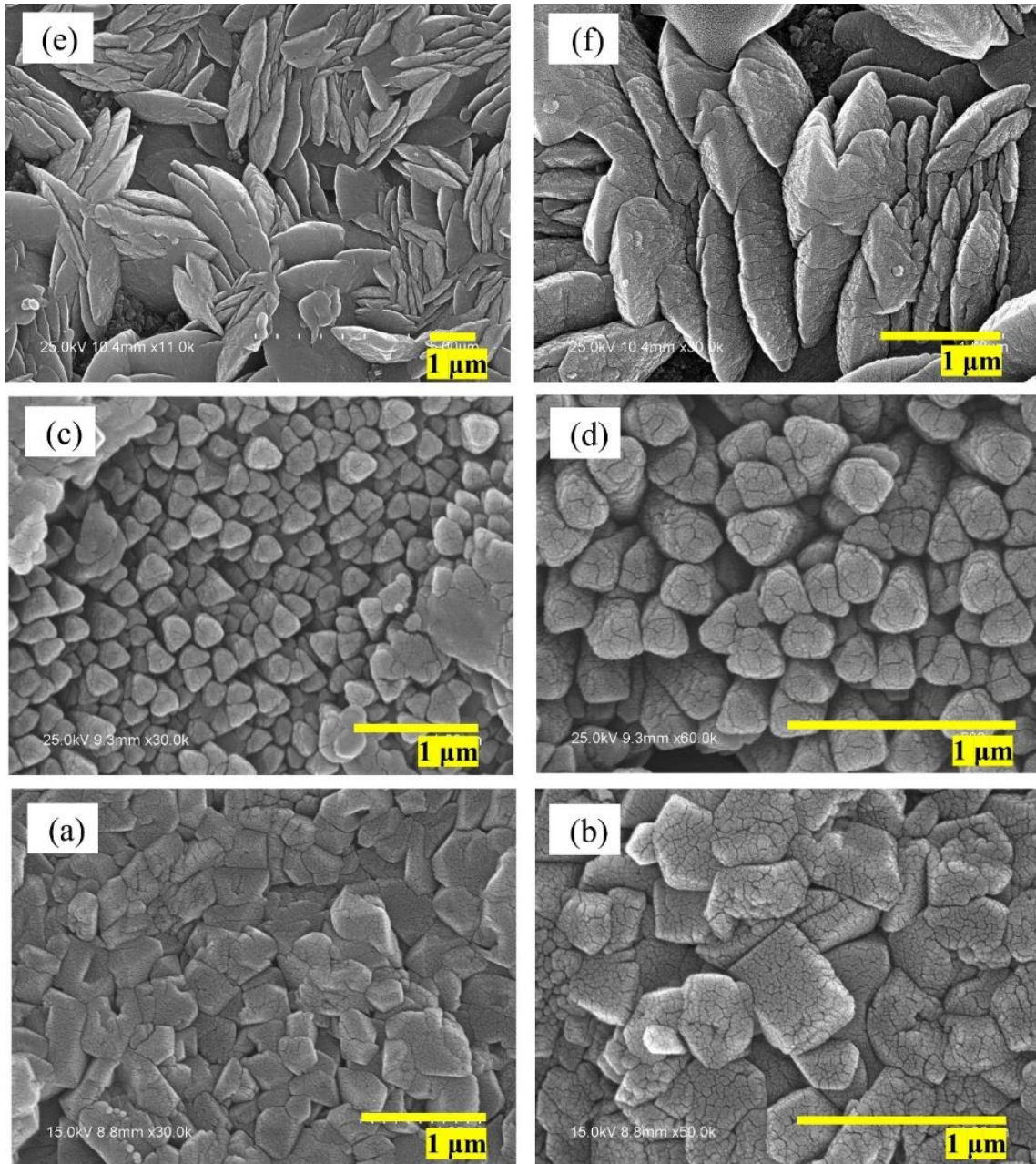
Figure 2.12: SEM images showing the CaCO₃ morphology in carbonated (a and b) control; (c and d) M-1 modified CSH; and (e and f) M-2 modified CSH samples

2.4 Discussion

The primary finding of this study is that the carbonation-induced decalcification and subsequent polymerization of CSH can be reduced by biomimetic-molecule modifications. The enhanced carbonation resistance of CSH due to this modification can be attributed to the following mechanisms. The presence of the selected biomimetic molecules ensures the stabilization of ACC and vaterite during the early stages of carbonation of the CSH. The governing mechanism for how the molecules interact with the CSH is shown in **Figure 2.13**. The negative OH^- from the biomimetic molecule gets attached with the positive Ca^{2+} from the CaO sheet of CSH and later forms the organic-inorganic hybrid phase while carbonation. The formation of organic-inorganic hybrid phase due to the presence of biomimetic molecules and $CaCO_3$ are discussed in a previous publication [58].
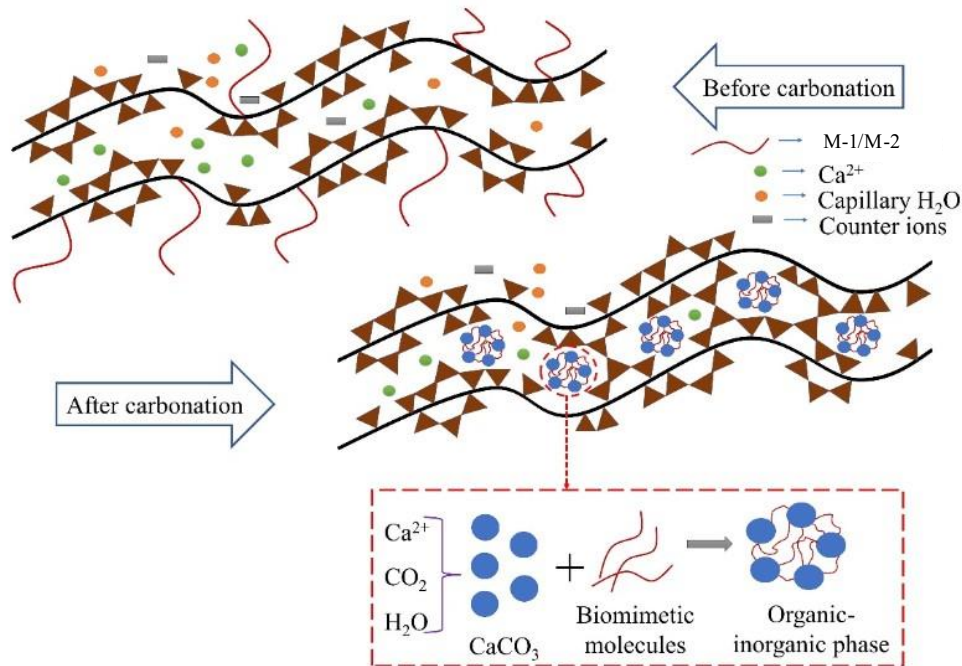
Figure 2.13: Interaction of biomimetic molecules with the CSH and formation of organic-inorganic phase

Stabilization of these metastable $CaCO_3$ polymorphs have multiple consequences:

(i)   These polymorphs have lower solubility compared to that of calcite. Specifically, the solubility constants for calcite, aragonite, and vaterite are $10^{-8.48}$, $10^{-8.34}$, and $10^{-7.91}$, respectively [49], [50]. ACC is 120 times more soluble than calcite [51]. Due to the high solubility of ACC and vaterite, formation of these phases can reduce the extent of carbonation [40].

(ii)   ACC (1.62~2.59 g/cc, depending on the H_2O content) and vaterite (2.66 g/cc) have lower density compared to that of calcite (2.71 g/cc) [117]. Accordingly, formation of same weight of metastable $CaCO_3$ occupies a higher volume compared to calcite, and therefore, formation of these $mCaCO_3$ reduces the CO_2 diffusion in the matrix.

(iii)   As reported by Kim et al. [118], this approach of controlling the in-situ crystallization of $CaCO_3$ using biomimetic molecules results in the formation of organic-inorganic nanohybrids with superior elastic modulus and hardness compared to that of the pure calcite crystal.

We suggest that due to mechanisms (i) and (ii), the biomimetic molecule modified CSH showed notable resistance to the carbonation degradation compared to that of the pure CSH. In addition, the above mechanism (iii) is responsible for the increased modulus of elasticity of the modified CSH after carbonation. We further suggest that the biomimetic-molecule $CaCO_3$ was not the only hybrid phase, but rather a nanocomposite phase containing the CSH-biomimetic molecule-$mCaCO_3$ was formed which had excellent elastic modulus compared to the pure CSH. A brief comparison of Figure 2.11 and Figure 2.5 reveals that the elastic modulus of the above hybrid phase is 16 times higher than the pure CSH (a 49 GPa average modulus of carbonated M-1 modified CSH vs. the 3 GPa of pure CSH).

The above findings can be highly beneficial for cementitious materials that contain CSH/C-A-S-H as the primary binding phases. These cementitious materials show degradation and strength loss due to carbonation-induced degradation of CSH. By utilizing the biomimetic molecules, it can be possible to reduce the carbonation degradation of the cementitious composites. Additionally, as observed due to the presence of biomimetic molecules, the mechanical properties of the CSH compacts were improved after carbonation. Thus, when the cementitious composites are exposed to atmospheric CO_2, the mechanisms of the biomimetic molecules will allow a denser outer layer to form which can work as an in-situ sealant layer for the composite.

2.5 Conclusions

The following are the concluding remarks from the present study:

i.   M-1 and M-2-modified C-S-H showed foil-like morphology and similar silicate polymerization as that of the pure C-S-H. However, C-S-H modified with M-1 and M-2 had nearly 3 times and 8 times higher elastic modulus, respectively, compared to that of the pure C-S-H.

ii. From TEM image analysis, it was seen that the morphology of the modified C-S-H samples were unaffected even after 168 h carbonation duration. On the other hand, after 168 h of carbonation, pure C-S-H converted to spherical silica gel particles with distinguishable periphery.

iii. ^{29}Si NMR of the C-S-H samples before and after carbonation showed that within the carbonation duration, pure C-S-H was fully converted to polymerized silica gel containing Q^3 and Q^4 species. In the cases of M-1 and M-2 modified C-S-H, no significant change in the C-S-H polymerization was observed despite the increased amount of $CaCO_3$ formation after 28 days of carbonation. Accordingly, we suggest that the carbonation of C-S-H took

place by the removal of interlayer Ca^{2+} from the C-S-H, which does not significantly alter the cross-linking/polymerization of the C-S-H.

iv. The modified C-S-H showed significantly increased elastic modulus after carbonation. The increase in the modulus of the M-1 modified C-S-H batch was higher than that of the M-2 modified C-S-H. The increase of modulus during carbonation was attributed to the formation of an organic-inorganic nanohybrid phase in the presence of the biomimetic molecules.

v. Under the tested experimental scenario, the modification by M-1 and M-2 reduced the CO_2 sequestration capacity of C-S-H by 45% and 25%, respectively. It is important to note that the result of this reduced CO_2 sequestration capacity was that the biomimetic-molecule modification allowed the C-S-H to retain its original structure and increased the elastic modulus after carbonation.

Chapter 3: In-situ FTIR experimental technique for monitoring the effect of different pH, Ca/Si ratio, and addition of biomimetic molecules on carbonation degradation of C-S-H

3.1 Research objectives

Calcium silicate hydrate (C-S-H) is a critical component in Portland cementitious materials, and its characteristics are pivotal for the physical performance, sustainability, and longevity of concrete infrastructures. One common degradation process of C-S-H is decalcification, wherein calcium leaches from its structure, leading to an increase in the degree of polymerization. Different decalcification mechanisms can result in varying physical performances of C-S-H. For example, decalcification induced by NH_4NO_3 has been observed to reduce the indentation modulus of C-S-H, while carbonation-induced decalcification increases the indentation modulus by forming $CaCO_3$ within the matrix. Carbonation also leads to matrix shrinkage due to C-S-H polymerization and increased porosity, which provides pathways for detrimental ions to penetrate, further degrading durability. Various polymorphs of $CaCO_3$ can form during carbonation, such as calcite, vaterite, aragonite, and amorphous calcium carbonate (ACC). Recent studies suggest that the use of specific biomimetic molecules can stabilize the C-S-H structure during carbonation, enhancing the indentation modulus and forming a hybrid phase comprising C-S-H, organic molecules, and $CaCO_3$. Given that carbonation is an inevitable process for most concrete structures due to atmospheric CO_2 exposure, extensive ex-situ research has been conducted to comprehend the carbonation mechanism of C-S-H, relying on techniques like NMR, X-ray diffraction, XPS, Raman spectroscopy, TEM, and thermal analysis. The calcium to silica ratio (C/S) emerged as a primary factor influencing C-S-H carbonation behavior, with different C/S ratios leading to distinct carbonation products. In-situ studies, despite their challenges related to C-S-H's semi-crystalline structure, are crucial for understanding early-stage carbonation behavior and $CaCO_3$ polymorph

formation. Notably, it was conducted the only in-situ carbonation study of C-S-H using X-ray total scattering measurements and PDF analysis, providing insights into the kinetics of C-S-H carbonation for a specific C/S ratio of 1.4. However, the in-situ carbonation kinetics of C-S-H for different C/S ratios and pH levels remain unexplored, presenting a promising avenue for future research.

To address the above discussed knowledge gap, the primary objectives of this study are as follows (i) demonstrate the application of in-situ ATR-FTIR as a simple method to monitor decalcification kinetics of C-S-H, (ii) evaluate the roles of C/S, pH, and the presence of M-1 on the decalcification kinetics of C-S-H, and (iii) in-situ monitoring of $CaCO_3$ formation and polymorph conversion during the carbonation of C-S-H for various experimental parameters.

1.1 Materials and methods

3.2.1 Raw materials

To prepare the laboratory synthesized C-S-H, the same procedures mentioned in Chapter 2 had been followed. This time, primarily the focus was on C-S-H containing Ca/Si = 1.5. However, to observe the effects of different Ca/Si, two more batches were prepared – Ca/Si = 1.0 and Ca/Si = 2.0. High purity grade biomimetic molecule, M-1 was purchased from VWR. For biomimetic molecule doped batch, 2.5% of M-1 (by percent weight of C-S-H) was added to the matrix before starting the in-situ FTIR experiment. NaOH pellets were used to prepare different pH water solution. To investigate the effects of different pH, four different pH water solutions were prepared – pH 7, pH 9, pH 11.5 and pH 13.

3.2.1 Methods

3.2.1.1 In-situ FTIR

The in-situ Fourier-Transformed Infrared (FTIR) spectra of the powder samples were collected using the Attenuated Total Reflection (ATR) mode with 4 cm^{-1} resolution and 32 scans for each sample. The test was conducted with freshly prepared samples. To perform the in-situ FTIR, first the background spectrum was collected using a 1 μL water drop in CO_2 atmosphere. The samples were taken in powder form. Around 15 mg samples were taken. 1 μL water was put on top of the powder sample before starting the test. CO_2 gas purging commenced immediately upon the placement of the paste sample onto the ATR tip. A total of 280 spectra was collected maintaining a time interval of 3.75 mins between two spectra. 99% CO_2 gas purging was maintained. The signal to noise ratio was maintained lower than 3:1.

3.2.1.1 Thermogravimetric analysis (TGA)

After the completion of the in-situ FTIR test, samples were collected and ground using a mortar and pestle, and the resulting powder was immediately utilized for TGA measurements. TGA measurements were conducted using a commercially available instrument (TA instrument, TGA 550). Approximately 15 mg of powder sample was tested for each batch. The powdered sample was loaded into a platinum pan and was kept under isothermal conditions at room temperature for 5 minutes. The temperature of the TGA furnace chamber was then incrementally raised to 980°C at a rate of 15°C per minute. Nitrogen was employed as purging gas throughout the experiment to maintain an inert environment.

3.2.1.1 Scanning electron microscopy (SEM)

The assessment of calcium carbonate crystal morphology was conducted using the Hitachi S4800 II FE-SEM. The equipment was operated under high-vacuum conditions, employing a 30-kV accelerated voltage and maintaining a working distance of approximately 12 mm. Prior to SEM

image capture, a Gold (Au)-Platinum (Pt) coating was applied to the sample. In this examination, the fractured surface of the carbonated samples was employed.

3.3 Results

3.3.1 Data repeatability

The obtained FTIR spectra range is too wide, from 400 cm^{-1} to 4000 cm^{-1}. We focused on two certain ranges to investigate the carbonate formation and silica gel polymerization. They are – 700 cm^{-1} to 750 cm^{-1} range and 900 cm^{-1} to 1200 cm^{-1} range respectively (**Figure 3.1**).
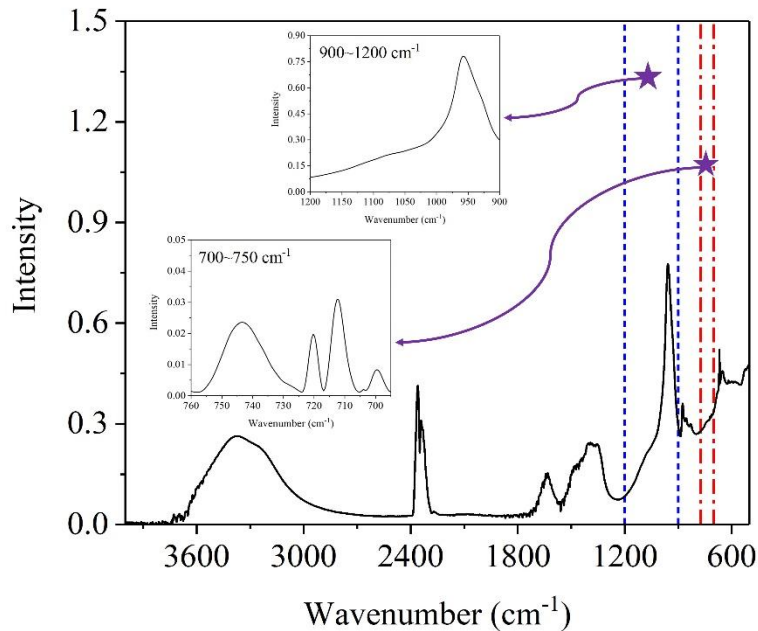
Figure 3.1: FTIR full range plot (700-4000 cm^{-1} range)

One of the major challenges of this in-situ FTIR work is to ensure the data repeatability. Every time, same steps were followed. However, to prove the acceptability of the datasets, we ensured data repeatability by repeating the control C-S-H batch (pH 7) thrice. They were labelled as – CSH T01, CSH T02, and CSH T03. **Figure 3.2(a)** shows all the collected spectra at 900 cm^{-1} to 1200 cm^{-1} range.

One of the major challenges of this in-situ FTIR work is to ensure the data repeatability. Every time, same steps were followed. However, to prove the acceptability of the datasets, we ensured data repeatability by repeating the measurements for the control C-S-H batch (pH 7) thrice. They were labelled as – CSH T01, CSH T02, and CSH T03. **Figure 3.1** shows all the collected spectra at 900 cm^{-1} to 1200 cm^{-1} range.

The Q^2 peak was found at 957 cm^{-1} and Q^3 was found at 1050 cm^{-1} (already mentioned in Chapter 2). Figure 3.2(b) presents the Q^2 to Q^3 degradation with time. During this convergence phase, it was observed that, the degradation occurred in two distinct phases: initial dormant period and then rapid convergence period. To compare among the repeated batches, the slope was taken at the rapid convergence period (**Figure 3.2(c)** and **(d)**). It was found that, 50% Q^2 degradation happened after 204 mins on average (with only 3.8% coefficient of variance). Besides, the mean slope value was obtained -0.2826 which was also within a very low coefficient of variance (only 2.4%). These results prove the repeatability of the datasets at 900 cm^{-1} to 1200 cm^{-1} range.
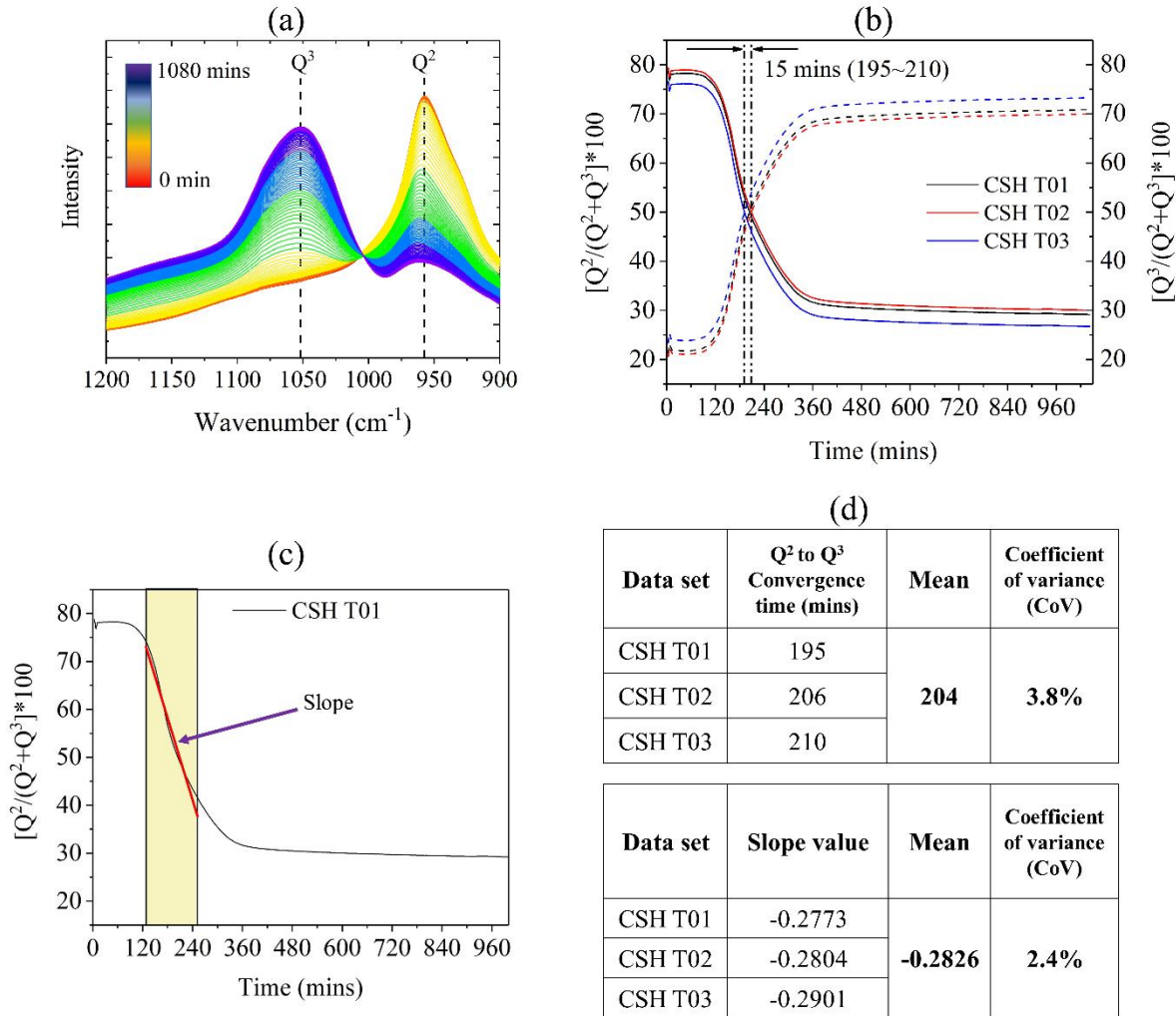
Figure 3.2: (a) CSH 900-1200 (b) Q^2 vs Q^3 convergence (T01, T02, T03) (c) obtained slope value (d) Summary of Q^2 vs Q^3 convergence and slope values

The Q^2 peak was found at 957 cm^{-1} and Q^3 was found at 1050 cm^{-1} [119]. **Figure 3.2**(b) presents the Q^2 to Q^3 degradation with time. During this convergence phase, it was observed that degradation occurred in two distinct phases: initial dormant period and then rapid convergence period. During the rapid convergence period, C-S-H degradation starts happening and silica gel formation begins. The remaining percent C-S-H and silica gel percentage at the corresponding time were calculated following the equations (1) and (2).

$$Remaining\ percent\ C-S-H = \frac{Q^2}{Q^2+Q^3} \times 100\ (\text{Eq 1})$$

$$Silica\ gel\ percentage\ =\ \frac{Q^3}{Q^2+Q^3} \times 100\ (\text{Eq 2})$$

To compare among the repeated batches, the slope was taken at the rapid convergence period (**Figure 3.2(c)** and **(d)**). It was found that, 50% Q^2 degradation happened after 204 mins on average (with only 3.8% coefficient of variance). Besides, the mean slope value was obtained 0.2826 which was also within a very low coefficient of variance (only 2.4%). This slope value indicates the rate of C-S-H degradation. These results prove the repeatability of the datasets at 900 cm^{-1} to 1200 cm^{-1} range.

To ensure data repeatability at low range (700 cm^{-1} to 750 cm^{-1}), percent calcium carbonate formation among the batches with standard deviation versus time plot has been generated in **Figure 3.3**. Percent calcite and vaterite were calculated following the equation (3).

$$\%\ Calcium\ carbonate = \frac{Calcium\ carbonate\ (e.g.\ calcite)}{Calcite + Vaterite + Aragonite + Bicarbonate} \times 100 \qquad (\text{Eq 3})$$

Based on the literature [58], [66], [119], [120], aragonite forms at around 700 cm^{-1}, calcite forms at around 713 cm^{-1} and vaterite forms at around 740 cm^{-1}. **Figure 3.3(a)** and **(b)** are presenting the 2D contour and 3D plotting at this range. Prominently, it is forming calcite at 713 cm^{-1} and vaterite formation is also visible at 740 cm^{-1}. **Figure 3.3(c)** shows the percent calcium carbonate formation with time. Since, calcite is the most thermos-dynamically stable calcium carbonate polymorph, it is showing low standard deviation. On the other hand, vaterite is metastable calcium carbonate polymorph and thermodynamically unstable, due to which, the standard deviation is higher.

To ensure data repeatability at low range (700 cm^{-1} to 750 cm^{-1}), % calcium carbonate formation among the batches with standard deviation versus time plot has been generated in **Figure 3.3**. Based on the literature [58], [66], [119], [120], aragonite forms at around 700 cm^{-1}, calcite forms at around 713 cm^{-1} and vaterite forms at around 740 cm^{-1}. **Figure 3.3(a)** and **(b)** are presenting the 2D contour and 3D plotting at this range. Prominently, it is forming calcite at 713 cm^{-1} and vaterite formation is also visible at 740 cm^{-1}. **Figure 3.3(d)** shows the percent calcium carbonate formation with time. Since, calcite is the most thermos-dynamically stable calcium carbonate polymorph, it is showing low standard deviation. On the other hand, vaterite is metastable calcium carbonate polymorph and thermos-dynamically unstable, due to which, the standard deviation is higher.
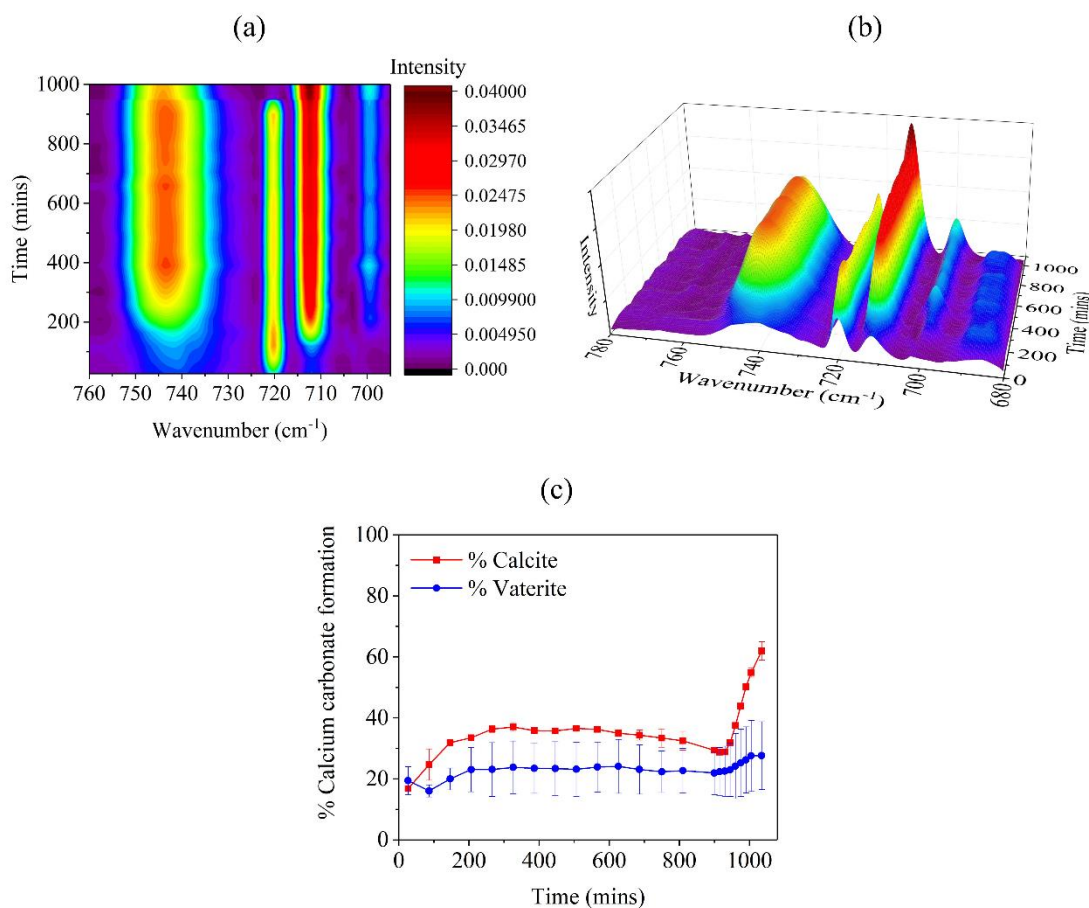
Figure 3.3: Plots for repeatability at 700cm^{-1} to 750 cm^{-1} range
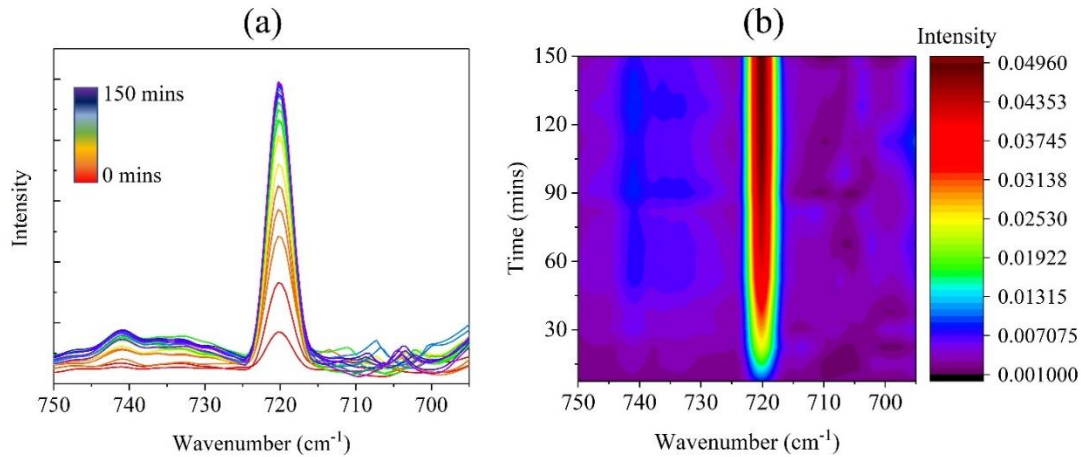
Figure 3.4: Water drop at 720 cm^{-1}

However, another prominent peak is noticeable at 720 cm^{-1}. It was bicarbonate peak. To ensure it, in-situ FTIR experiment was conducted on a drop of water for 150 mins, and the outcome is presented in **Figure 3.4**.

3.3.2 Role of pH on decalcification

To investigate the effects of pH on decalcification, four different pH environments were chosen on the control C-S-H sample. They are – pH 7, pH 9, pH 11.5 and pH 13. The same in-situ FTIR technique was applied for these batches.
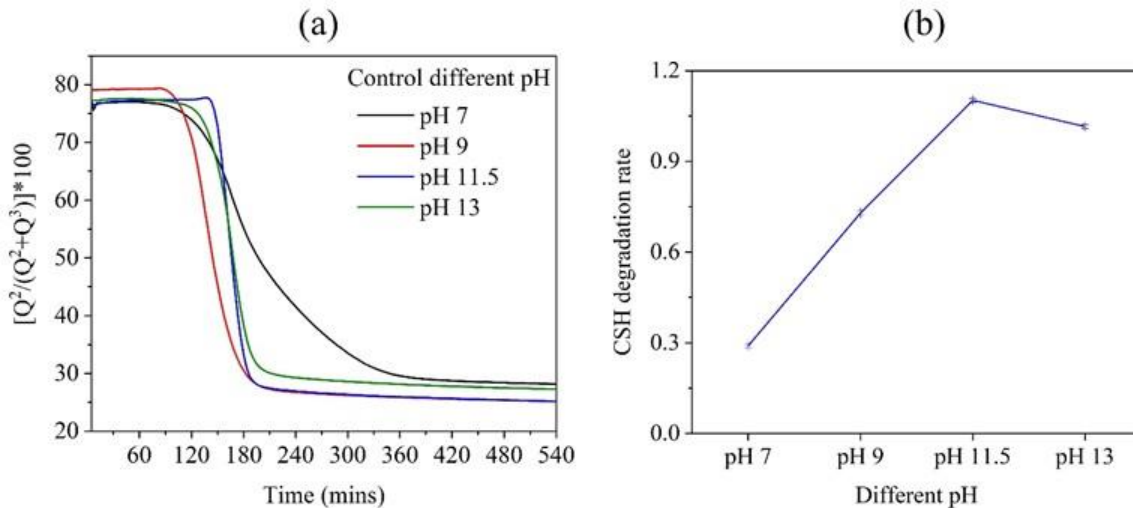
Figure 3.5: (a) Change of Q^2 vs time of control pure CSH at different pH, (b) slopes at different pH, (c) 50% Q^2 degradation vs different pH

Figure 3.5(b) shows that, increasing the pH increases the slopes as well which means faster Q^2 degradation. **Figure 3.6** shows the percent formation of different calcium carbonate polymorphs at different pH environments. Among the batches, at pH 9 environment, percent vaterite formation was the highest while, the pH 7 formed the lowest amount of vaterite. From this outcome, pH 9 environment has been chosen to observe the effects of different Ca/Si ratio.
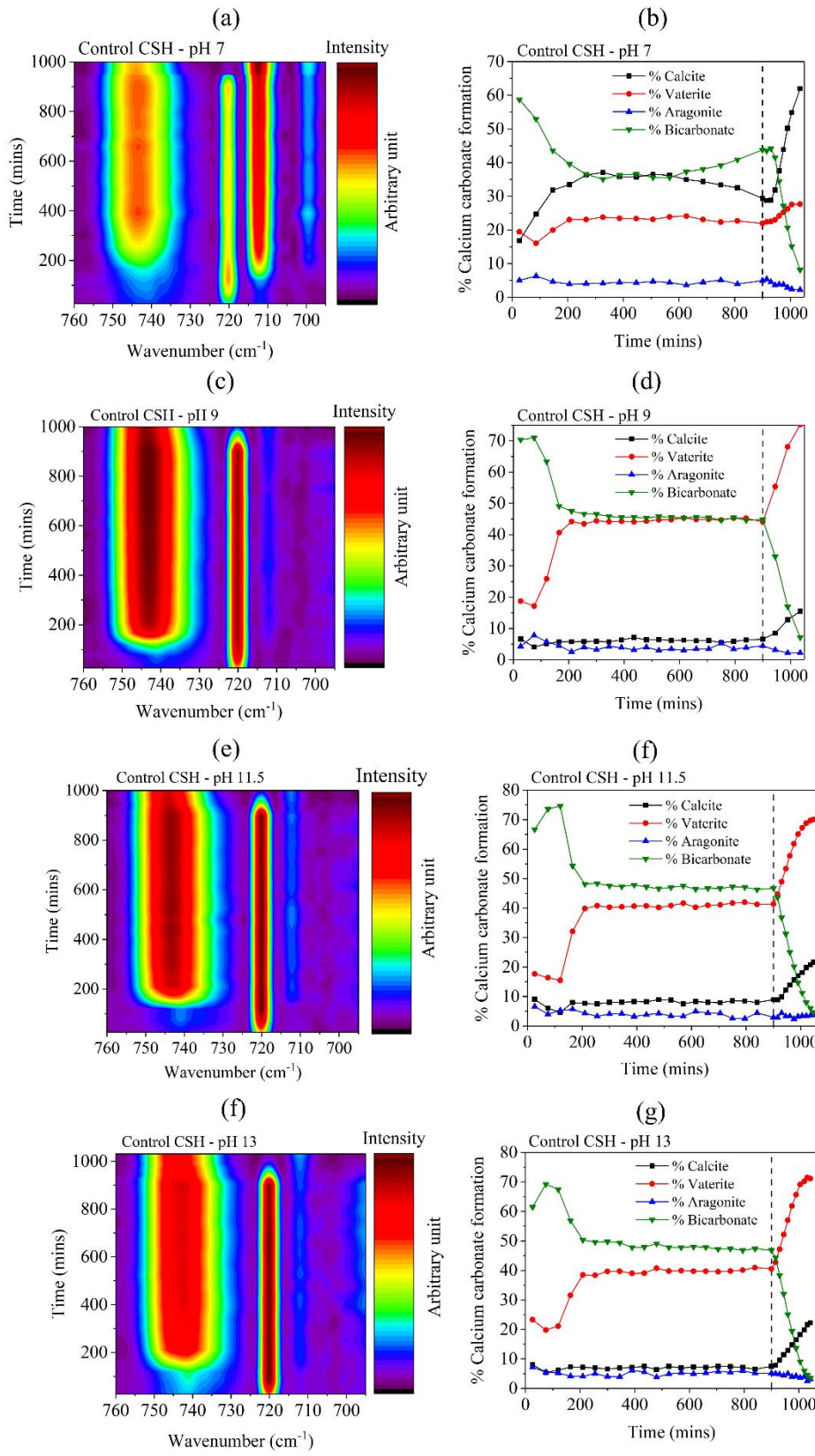
Figure 3.6: Calcium carbonate formation in control CSH at different pH environments

3.3.3 Role of Ca/Si on decalcification

The effects of different Ca/Si on decalcification are presented in **Figure 3.7.** Three different batches of C-S-H were synthesized following the ratio 1.0, 1.5 and 2.0 at pH 9 environment.
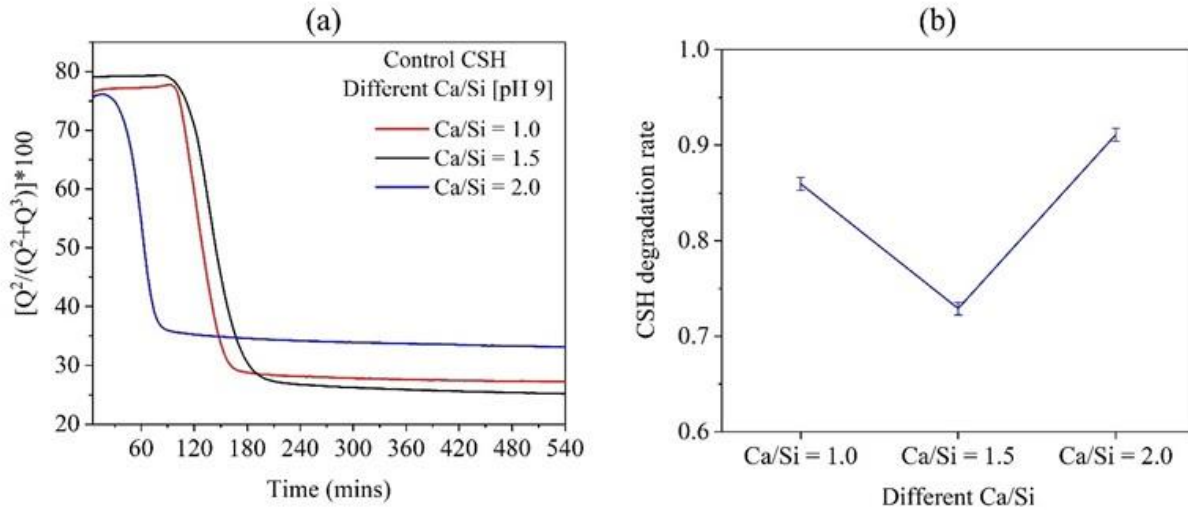
Figure 3.7: (a) Change of Q^2 vs time of pure CSH at different Ca/Si; (b) slope values at different Ca/Si

Except Ca/Si = 1.5, the other two showed higher degradation rate. Higher Ca/Si indicated higher Ca^{++} in the system, therefore, carbonates formation was easier due to the more available calcium ions in the system. Due to this phenomenon, Ca/Si = 2.0 did not resist for more than an hour. However, Ca/Si = 1.5 took the highest amount of time to degrade among the three batches. From **Figure 3.8**, it also exhibits that, percent vaterite formation was the maximum for the Ca/Si ratio batch. The other two ratio batches formed less amount of metastable calcium carbonates with higher calcite formation.
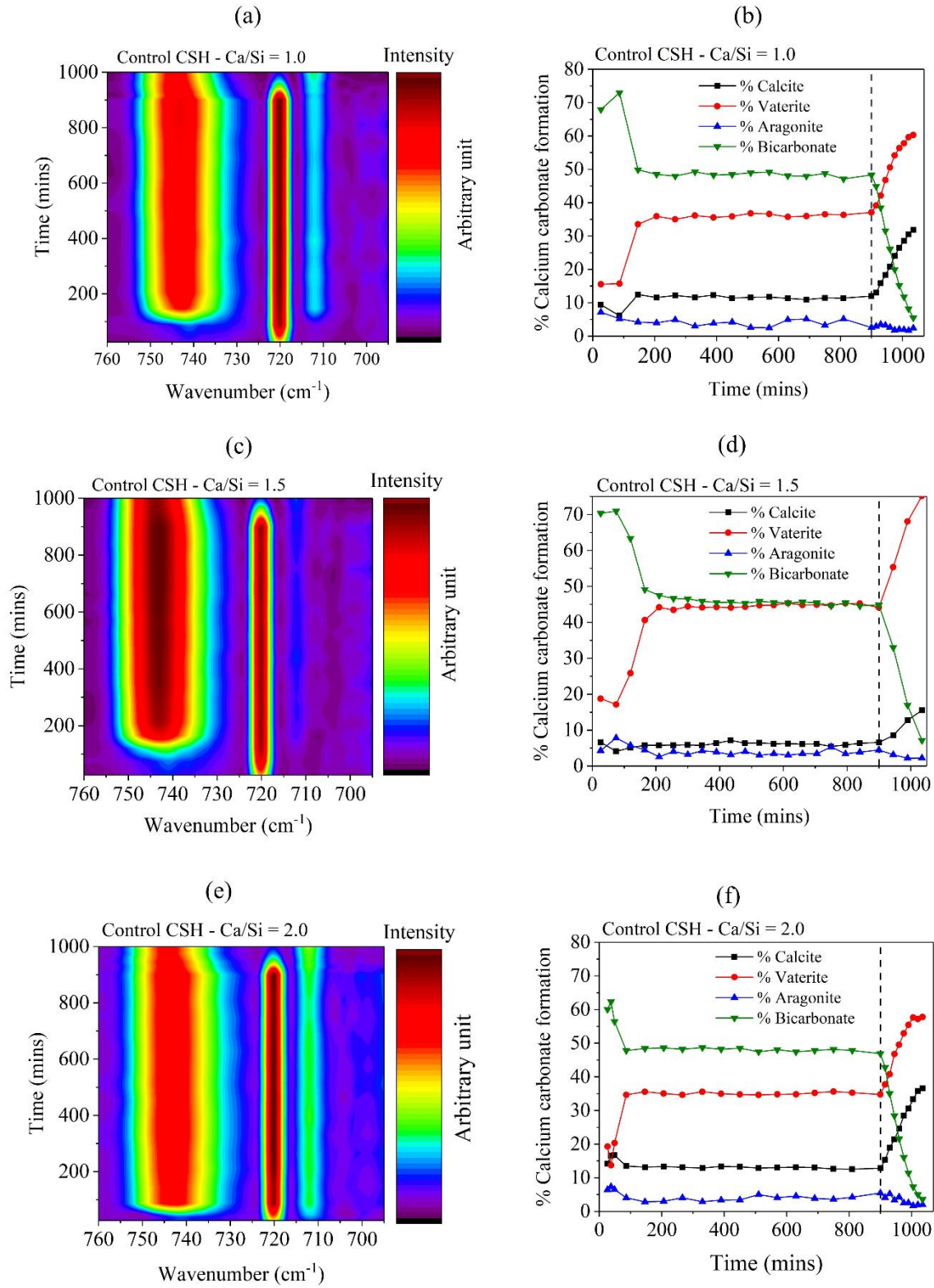
Figure 3.8: Calcium carbonate formation in control CSH at different Ca/Si

3.3.4 Role of biomimetic molecule on decalcification

Role of biomimetic molecule on decalcification was observed in presence of M-1 molecule at a very low dosage (2.5%). Then, it was compared with respect to the control batch to see any further improvement.
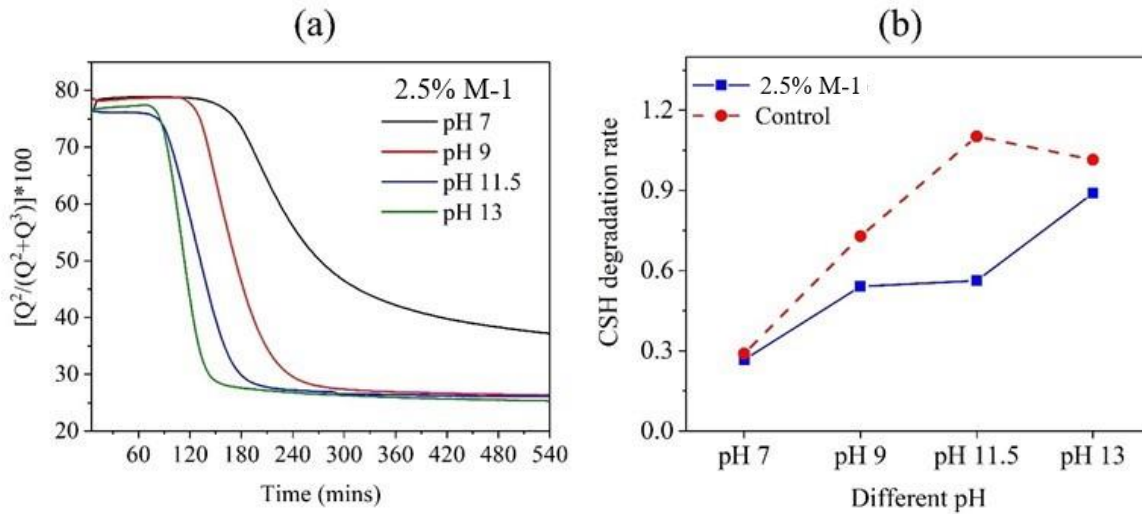
Figure 3.9: (a) Change of Q^2 vs time of biomimetic modified CSH at different pH; (b) slope values at different pH of 2.5% M-1 modified CSH

Figure 3.9(a) shows Q^2 degradation of 2.5% M-1 modified C-S-H batches with respect to different pH environment. With the increase of the pH, the degradation is happening faster. However, it showed better performance with respect to control batches at lower pH dosages (pH 7 and pH 9). At higher pH dosages (pH 11.5 and pH 13), it could resist the degradation well (**Figure 3.9(b)**). However, it resisted faster degradation compared to the control batch (**Figure 3.9(b)**). **Figure 3.10** shows that, all the M-1 modified batches formed significant amount of metastable calcium carbonates (vaterites) compared to the control batches (**Figure 3.6**).
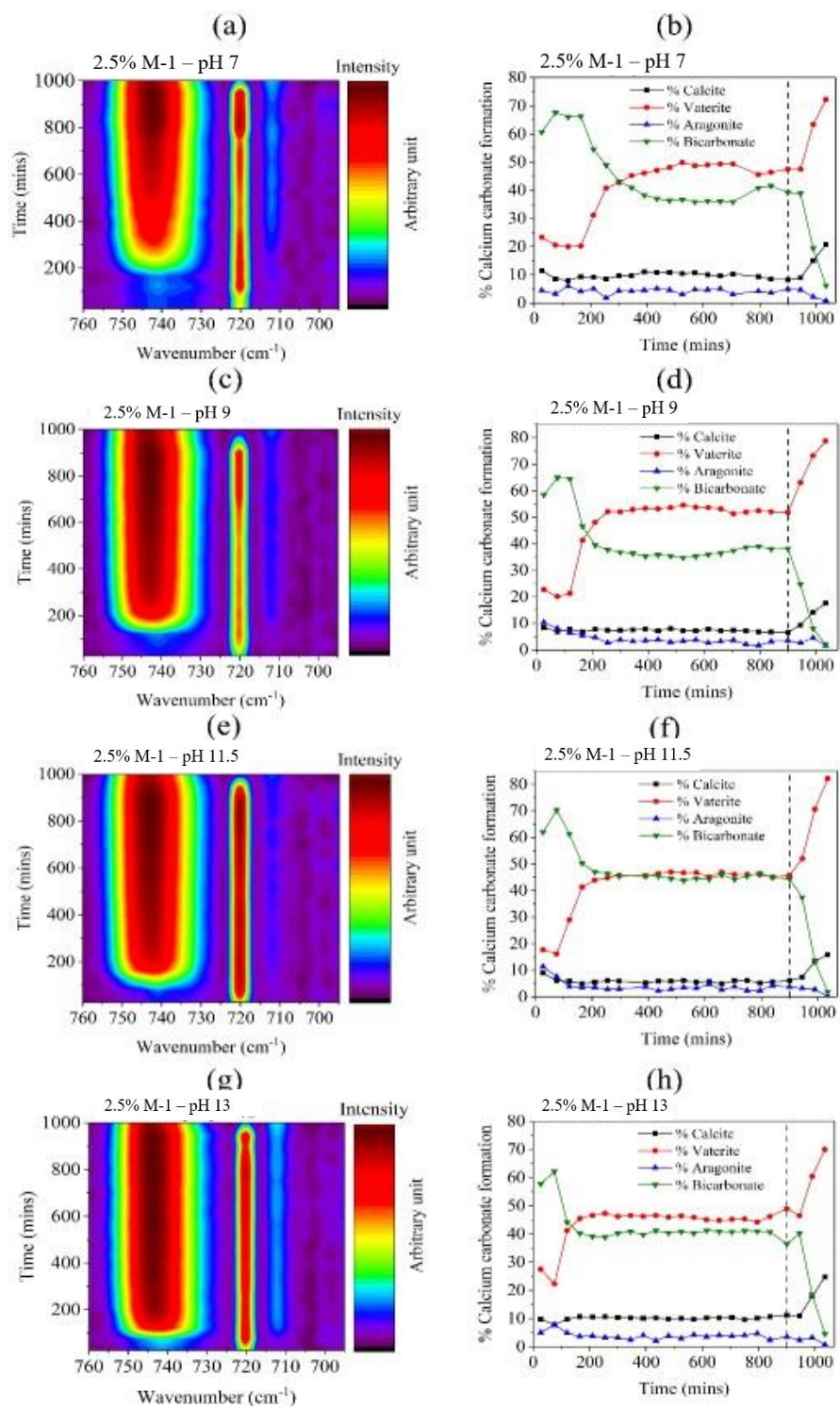
Figure 3.10: Calcium carbonate formation in biomimetic molecule modified CSH batch at different pH

3.3.4 CO₂ sequestration

Figure 3.11 presents the TGA-DTG plots of the samples after the completion of in-situ FTIR experiments. The weight loss range has been taken into consideration from 200°C to 780°C where the decomposition was occurred due to the chemically bound H_2O and CO_2.
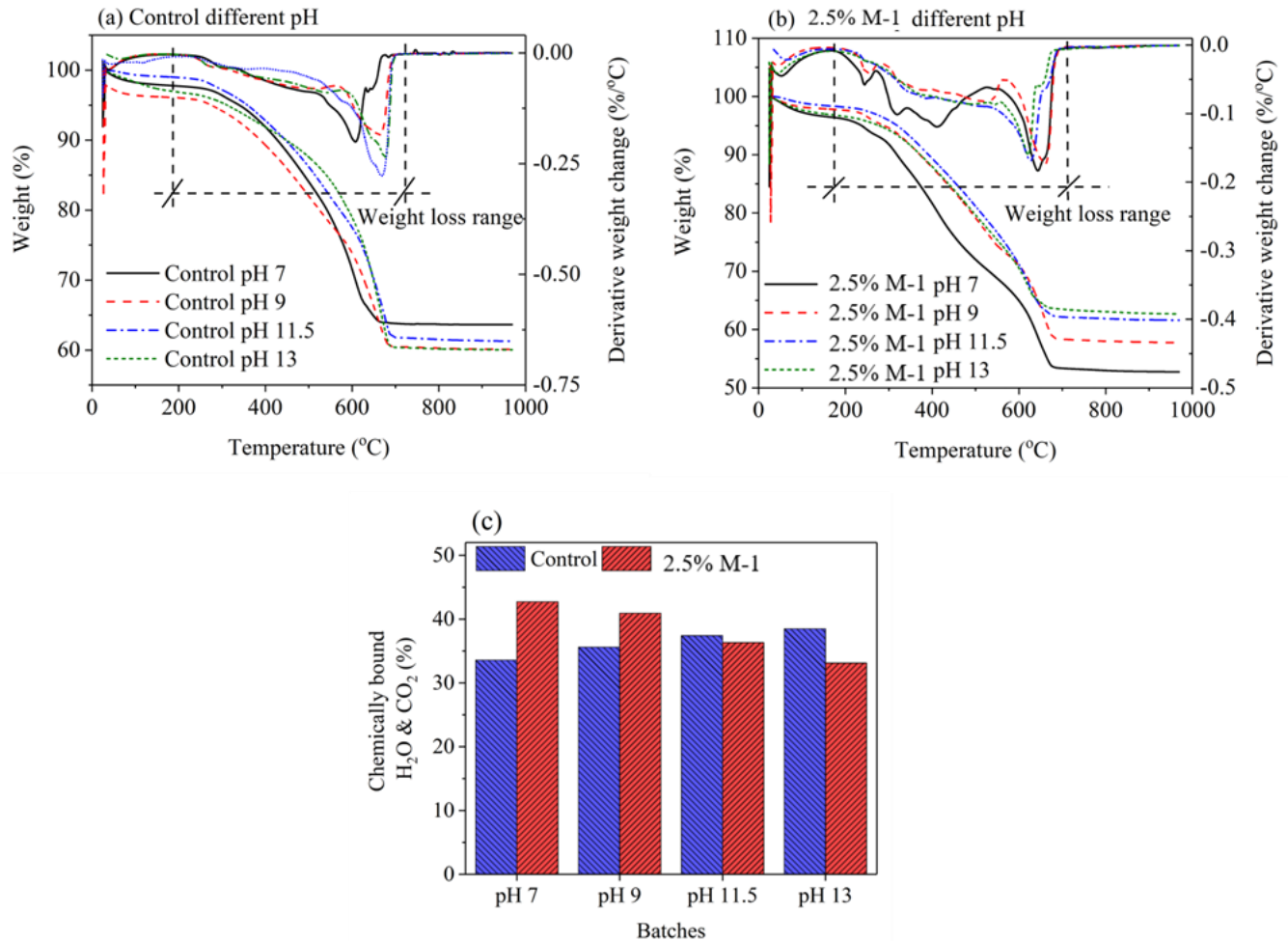
Figure 3.11: (a) TGA-DTG of Control CSH different pH batches; (b) TGA-DTG of 2.5% M-1 dosage different pH batches; (c) percent chemically bound H_2O and CO_2 contents

In the **Figure 3.11(a) and (b),** TGA DTG plots of the control and M-1 modified batches at different pH environments are shown. From the decomposition range 200°C to 780°C, percent chemically bound H_2O and CO_2 are calculated using the area under the curve method and presented in **Figure**

3.11(c). Significant amount of CO_2 uptake can be observed at high pH and after the addition of M-1 molecules which shows the promising avenue of carbon sequestration while the CSH is incorporated with a very low dosage of biomimetic molecules.

The CSH samples with Ca/Si = 1.5 were tested for thermogravimetric analysis with or without the M-1 addition. It was calculated from the before carbonation fresh CSH sample that, the amount of chemically bound H_2O was around 20%. However, theoretically, maximum CO_2 binding capacity of the CSH with Ca/Si = 1.5 is around 29.6%. Therefore, we can see the combined storage capacity of chemically bound H_2O and CO_2 from the plots.

3.3.4 Scanning electron microscopic observations
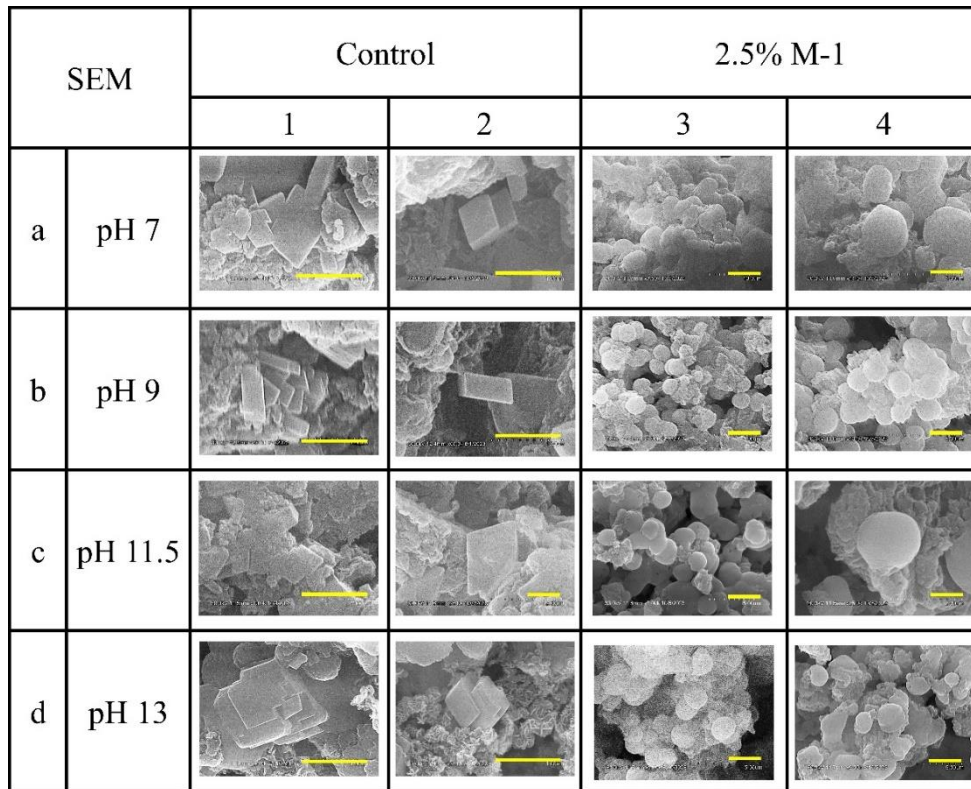
Figure 3.12: Scanning Electron Micrographs (SEM) of C-S-H (Ca/Si = 1.5) with and without M-1 of different pH environments. The scale bar represents 1 μm.

The Scanning Electron Micrographs (SEM) of the different samples after 18 hours of exposure to carbonation are presented in **Figure 3.12**. Here, columns 1 and 3 represent agglomerated, and columns 2 and 4 represent single crystals of different calcium carbonate polymorphs. For all the control samples, calcite crystals were prominent irrespective of the pH environment. The crystal sizes varied from 400 nm to 1.6 µm. The crystals co-existed with the C-S-H gel phase. On the other hand, C-S-H with 2.5% M-1 sample exhibited primarily amorphous calcium carbonate (ACC) phase. The size of the ACC crystal varied from 250 nm to 1.7 µm.

3.4 Discussions

In our experimental investigation, the influence of varying pH levels on the process of decalcification was explored. To do this, four distinct pH environments - pH 7, pH 9, pH 11.5, and pH 13 - were selected, and the same in-situ FTIR technique was applied to the control calcium-silicate-hydrate (C-S-H) sample. Observations revealed that an increase in pH was associated with an elevated rate of decalcification, as evidenced by steeper slopes, indicating faster degradation of the Q2 component. Additionally, the percentage formation of various calcium carbonate polymorphs under different pH conditions was illustrated in our findings. Remarkably, at a pH environment of 9, the formation of vaterite was most pronounced, while pH 7 resulted in the lowest vaterite formation. Consequently, pH 9 was selected as the optimal environment for the examination of the effects of different Ca/Si ratios on decalcification.

The effects of diverse Ca/Si ratios on decalcification were subsequently investigated in a pH 9 environment, with three distinct C-S-H batches synthesized according to ratios of 1.0, 1.5, and 2.0. Except for Ca/Si = 1.5, a higher degradation rate was exhibited by the other two ratios. This trend was attributed to higher Ca++ content in the system, which facilitated the formation of carbonates due to the increased availability of calcium ions. As a consequence, Ca/Si = 2.0 showed limited

resistance to degradation, lasting no longer than an hour. In contrast, Ca/Si = 1.5 demonstrated the longest time to degrade among the three batches. Furthermore, our analysis indicated that the Ca/Si = 1.5 batch displayed the highest percentage of vaterite formation, whereas the other two ratio batches exhibited reduced metastable calcium carbonate formation and a greater prevalence of calcite formation.

To delve into the role of biomimetic molecules in decalcification, a biomimetic molecule, M-1, was introduced at a low dosage (2.5%) and its performance was compared with the control batch. Findings unveiled that Q^2 degradation in the 2.5% M-1 modified C-S-H batches was influenced by the pH environment, with faster degradation observed as pH levels increased. Nevertheless, at lower pH values, specifically pH 7 and pH 9, enhanced performance compared to the control batches was displayed by the 2.5% M-1 modified batches. At higher pH levels, namely pH 11.5 and pH 13, resistance to degradation was exhibited by the modified batches, although they still degraded faster when contrasted with the control batch. Additionally, analysis demonstrated that a significant amount of metastable calcium carbonates, specifically vaterite, was formed by all M-1 modified batches in comparison to the control batches.

In the pursuit of carbon dioxide (CO_2) sequestration, TGA-DTG plots of the samples after in-situ FTIR experiments were provided. The weight loss range considered was between 200°C and 780°C, reflecting the decomposition attributable to chemically bound H_2O and CO_2. Notably, it was observed that a substantial uptake of CO_2 occurred at higher pH levels and with the addition of M-1 molecules. This outcome suggests a promising avenue for carbon sequestration when employing C-S-H with a very low dosage of biomimetic molecules. Furthermore, thermogravimetric analysis was performed on C-S-H samples with a Ca/Si ratio of 1.5, both with and without the addition of M-1. Analysis indicated that the chemically bound H_2O content in

fresh C-S-H samples, prior to carbonation, was approximately 20%. However, the maximum CO_2 binding capacity of C-S-H with a Ca/Si ratio of 1.5 was theoretically estimated to be around 29.6%. But the total amount of chemically bound H_2O and CO_2 was more than that. Therefore, it is evident that a significant amount of CO_2 was sequestered in the system.

3.5 Conclusions

Based on the findings, the concluding remarks are –

(i)   In-situ FTIR experiment is a novel technique to monitor the carbonation effects on calcium silicate hydrates samples. However, ensuring strict quality control cannot be compromised.

(ii)   pH has effects on C-S-H degradation. Higher pH environment occurs the degradation faster. pH 9 environment showed fastest degradation.

(iii)   Ca/Si has noticeable effects on C-S-H decalcification. Ca/Si = 1.5 showed a low degradation rate compared to Ca/Si = 1.0 and 2.0.

(iv)   Even though, higher pH environment makes the degradation faster, it can be reduced with a very low dosage (2.5%) of M-1 biomimetic molecule. Addition of M-1 biomimetic molecule showed improved resistibility to C-S-H degradation. However, lower pH environment needs to be ensured.

(v)   The addition of M-1 biomimetic molecule showed significant improvement in CO_2 sequestration as well.

Chapter 4: Utilization of biomimetic molecules to enhance the properties of carbonation cured gamma dicalcium silicates (γ-C_2S)

4.1 Research objectives

In response to the escalating need for eco-friendly binder systems, there has been a growing push to address the substantial carbon footprint associated with conventional Portland cement (OPC). An emerging alternative in this regard is the carbonation-activated low-lime calcium silicate binder, which has gained attention for its potential to reduce the environmental impact of cement production by lowering temperature requirements and clinker production. Among the calcium silicates, dicalcium silicate (C_2S) has emerged as a candidate for reducing energy consumption in cement manufacturing, particularly when used as the primary cement constituent. Of note, γ-C_2S, has garnered interest due to its unique characteristics, including the "dusting" effect, which reduces grinding energy requirements, and its remarkable CO_2 absorption abilities, making it a sustainable construction material. Research also indicates similarities in the behavior of wollastonite (CS) and rankinite (C_3S_2) to that of γ-C_2S when subjected to carbonation curing, underscoring the importance of understanding γ-C_2S's carbonation reactivity for low-carbon calcium silicate-based cementitious materials. The mechanical properties of carbonated cement composites are significantly influenced by the formation of different $CaCO_3$ polymorphs, with amorphous calcium carbonate (ACC) as an initial precursor that transforms into metastable phases like vaterite or aragonite before stabilizing as calcite, ultimately contributing to improved mechanical strengths. However, controlling the formation of these polymorphs is a complex task, influenced by factors such as humidity, temperature, CO_2 concentrations, and water content. To address this challenge, researchers have explored the use of organic molecules, including amino acids and biomimetic molecules, to influence polymorph formation in carbonated cementitious composites. Amino acids

like ovalbumin, lysozyme, and bovine serum albumin (BSA) have been employed to modify $CaCO_3$ polymorphs, demonstrating potential for enhancing mechanical properties. Previous studies on carbonated γ-C_2S samples have been carried out under molding pressure and high-temperature curing conditions, resulting in substantial strength gains when exposed to high CO_2 concentrations.

Biomimetic molecules, M-1 and M-3 were chosen along with M-4 to observe their ability to enhance the nano and micro-structural properties of carbonated γ-C_2S composites. The hypothesis is - these biomimetic molecules can alter the $CaCO_3$ polymorphs formation which will eventually enhance the micro and nano-mechanical performance of the carbonated γ-C_2S composites. For this, micro to nano structural analyses were performed on carbonated γ-C_2S composites to verify the hypothesis.

4.2 Materials and methods

4.2.1 Raw materials and sample preparation

There are several methods for synthesizing pure calcium silicate phases [121]–[123]. Most of these methods use the technique of sintering the stoichiometric mixture of lime and silica. In this study, $CaCO_3$ (>99% purity) and fumed silica (>99% purity) were used to synthesize γ-C_2S. High purity grade M-1, M-3 and M-4 were purchased from VWR.
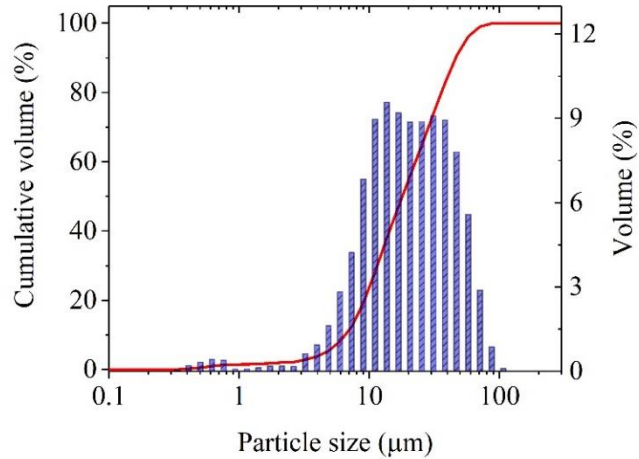
Figure 4.1: Particle size distribution of the synthesized γ-C₂S

Uniform mixing of $CaCO_3$ and fumed silica was prepared to obtain a molar ratio of 2:1 in the presence of water (w/b was maintained 0.65 to ease the mixing procedure). This paste mixture was then placed inside a high temperature furnace and sintered up to 1400°C for 4h. After this, it was left inside the furnace until it cooled down to a room temperature following a slow cooling process to ensure the stabilization of γ-C₂S. The resulting products were ground, sieved through mesh #200 (74 μm) and fried twice to maximize the chemical reaction of available lime and silica. After each sintering cycle, powder sample was evaluated by the X-ray diffraction (XRD) to check the presence of any free lime contents. From thermogravimetric analysis (TGA), it was checked that the free lime content of the synthesized γ-C₂S was maintained to be below 3%. The particle size distribution of the synthesized γ-C₂S is shown in Figure 4.1 which was determined using a commercially available laser particle size analyzer. Two types of samples were prepared for carbonation curing: (i) thin disc from paste samples (~5 mm thick and 20 mm dia) and (ii) compacted paste cube and beam samples.
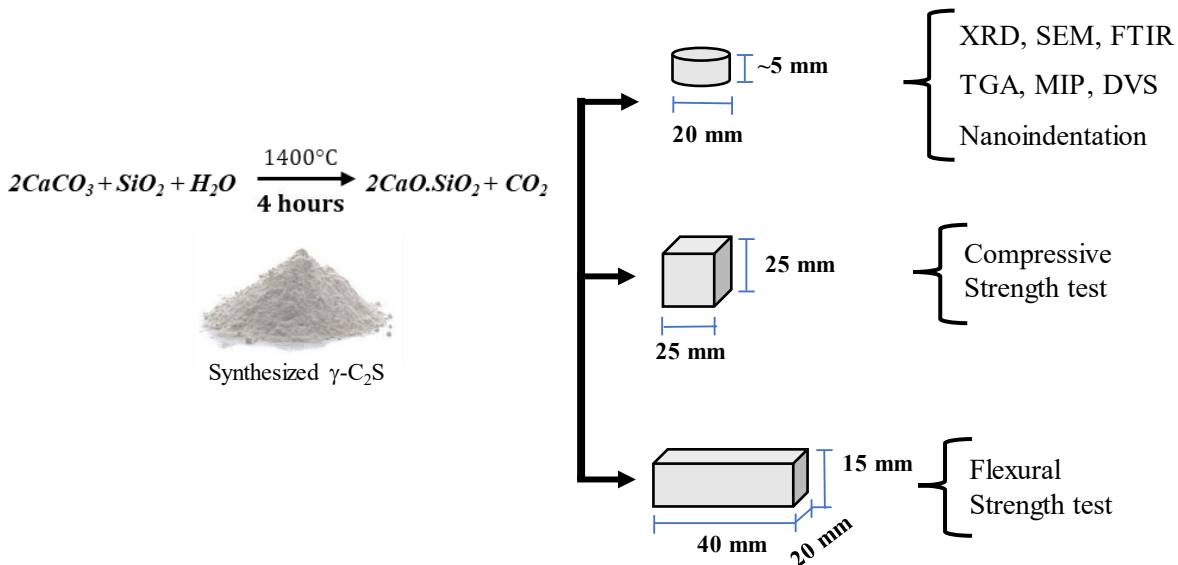
Figure 4.2: Schematic diagram of the sample preparation

First type of samples was used to monitor the $CaCO_3$ polymorph formation and evolution along with nanomechanical properties during the carbonation period. The second category was prepared for mechanical strength and pore size distribution analysis. For preparing the paste samples, dry biomimetic molecules were first mixed with water at 2.5% and 5% concentration (by weight percentage of γ-C_2S). **Figure 4.2** shows the schematic diagram of the sample preparation of each experiment.

4.2.2 Test methods

Samples of carbonated paste were gathered after 7 days and subsequently ground to prepare them for X-ray diffraction (XRD) analysis. These powdered samples were loaded into a Bruker D500 spectrometer, where a Cu Kα radiation (40 kV, 30 mA) was employed. The diffraction patterns were then recorded in the 2θ range of 10° to 60° with a step size of 0.03 (2θ) per second.

Phase identification through X-ray diffraction (XRD) was carried out using commercially available software known as "Match! Phase Analysis using Powder Diffraction." The PDF card

numbers used for reference were as follows: PDF #96-900-0967 for calcite, PDF #96-901-3802 for aragonite, PDF #96-150-8972 for vaterite, and PDF #96-154-6026 for γ-C_2S.

The microstructures of the carbonated γ-C_2S pastes were analyzed using the Hitachi S4800 II FE-SEM. Operating in high-vacuum mode, the instrument employed a 30-kV accelerated voltage and maintained a working distance of approximately 11 mm. Before capturing the SEM images, the cement paste sample was coated with Gold (Au)-Platinum (Pt). The analysis utilized the powder form of the paste samples.

Fourier-Transformed Infrared (FTIR) spectra of the ground paste sample were obtained using the Attenuated Total Reflection (ATR) mode, employing a resolution of 4 cm^{-1} and conducting 32 scans for each sample. The signal to noise ratio was maintained below 3:1. The FTIR test was performed on carbonated samples collected after 7 days.

The TGA experiment of the paste sample was conducted using a commercially available instrument (TA instrument, TGA 550). The paste samples, which had been stored in a vacuum desiccator, were used for this test. To prepare the samples, they were ground with a mortar pestle until a fine powder was obtained. Around 25-30 mg of the powdered sample, passing through a #200 sieve, was loaded into a platinum pan. The pan was subjected to an isothermal condition at 25°C for 5 minutes before gradually increasing the chamber temperature to 980°C at a rate of 15°C per minute. To ensure an inert environment, nitrogen gas was purged during the process.

To validate the consistency of carbonation across samples, the TGA test was initially performed with three replicate samples. The results showed a deviation of less than 2% by weight of total carbonated samples, indicating good reproducibility. Consequently, for the remaining batches, TGA was performed with only one sample due to the low level of deviation.

The Micrometrics Instrument Corporation AutoPore IV 9500 V2.03.01 was utilized to conduct Mercury intrusion porosimeter (MIP) experiments on cementitious composites. This technique is employed to determine the structure of meso-porous (pore radius 2~50 nm) and macro-porous (> 50 nm) materials. The MIP test was carried out on three sets of samples: the control batch, and paste samples with 2.5% and 5% dosages, all subjected to carbonation curing for 7 days. The sample size was standardized to $15 \times 15 \times 15$ mm.

In the MIP experiment, mercury was used with a surface tension of 0.485 N/m and an average contact angle of 130° with the pore wall. The maximum pressure applied was 413 MPa, allowing the examination of pores with a diameter as small as 3.02 nm. This analysis helps in characterizing the pore structures of the cementitious composites in different dosage conditions after the carbonation curing period.

To obtain the moisture desorption isotherm of carbonated paste samples, the commercially available DVS equipment (TA instrument, Q5000) was employed. Prior to testing, the samples were immersed in DI water for 6 hours to ensure complete saturation. About 4-5 mg of the saturated sample was loaded into a quartz pan.

The desorption isotherm was obtained by first equilibrating the sample at 97.5% relative humidity (RH) for 5760 seconds. Subsequently, the RH was gradually reduced in steps of 5-10% to achieve desorption. At each RH level, mass equilibrium was considered reached when the sample's mass fluctuation remained below 0.001% for 15 minutes. The entire experiment was conducted at a constant temperature of 23°C, and nitrogen gas was consistently purged during the process to maintain a stable environment.

DVS is the favored method for assessing meso and gel pore structures in cementitious phases, as opposed to mercury intrusion porosimetry (MIP) [124]. When compared to water sorption, the nitrogen sorption technique significantly underestimates the surface area of cementitious matrix. This article utilized the BET method to determine the surface area (S_{BET}) of carbonated composites. [125] and pore size distribution was determined based on the BJH model [126]. The calculation of the BET and BJH methods can be found elsewhere [77], [127].

For the nanoindentation tests, a Hysitron Triboindenter UB1 system (Hysitron Inc., Minneapolis, USA) equipped with a Berkovich diamond indenter probe was utilized. To ensure accurate measurements, the tip area function was calibrated using multiple indents with varying contact depths on a standard fused quartz sample. The surface roughness was evaluated using the Berkovich tip, and in all instances, it was found to be below 80 nm over an area of 60 μm × 60 μm. This level of surface quality was deemed suitable for conducting nanoindentation tests.

For grid nanoindentation, 7 days carbonated samples were specifically chosen. The load function adopted a three-segment approach: (i) a 5-second loading process from zero to maximum load, (ii) a 5-second hold at the maximum load, and (iii) a 5-second unloading from maximum to zero load. To accurately determine the mechanical properties of individual microscopic phases, it was essential to ensure that the depth of indentations remained considerably smaller than the characteristic size of each microscopic phase (indentation depth ≪ characteristic size of each microscopic phase) [128]. Therefore, for this study using the SNI technique, a maximum force of 2000 μN was selected. As a result, the average indentation depth within a 30 μm × 30 μm area ranged from approximately 100-300 nm.

To measure the compressive strength, a Gilson compressive strength testing machine was employed, applying a loading rate of 450 N/s. On the other hand, the flexural strength, determined

through the 3-point bending test, was measured using a laboratory-made micro-mechanical tester with a displacement rate of 1 mm/min.

After 7 days of carbonation curing, the compressive and flexural strength of paste samples were evaluated. The cube-shaped samples measured 25 mm $\times$ 25 mm $\times$ 25 mm, while the beam-shaped samples were 40 mm $\times$ 20 mm $\times$ 15 mm.

To observe the effects of high temperature curing, another set of samples were prepared for both compressive and flexural strength testing and kept inside the carbonation chamber at 50°C for 7 days (maintaining the same other parameters; 20% CO_2 concentration, 80% RH).

4.3 Results and discussions

4.3.1 Effects on the carbonation extent and CO_2 sequestration

The thermogravimetric analysis graphs (TGA and DTG) of 7 days carbonated samples are shown in **Figure 4.3**. Mass losses in the temperature range of 500-800 °C of 7 days cured paste samples were due to the decomposition of $CaCO_3$ phases [69]. Presence of multiple DTG peaks in this temperature range were attributed to the decomposition of different polymorphs of $CaCO_3$ [77], [91], [129]. From SEM and XRD analysis, multiple $CaCO_3$ polymorphs formation was also confirmed. TGA results were eventually used to calculate the total $CaCO_3$ contents decomposed in the system **Figure 4.3(c).**
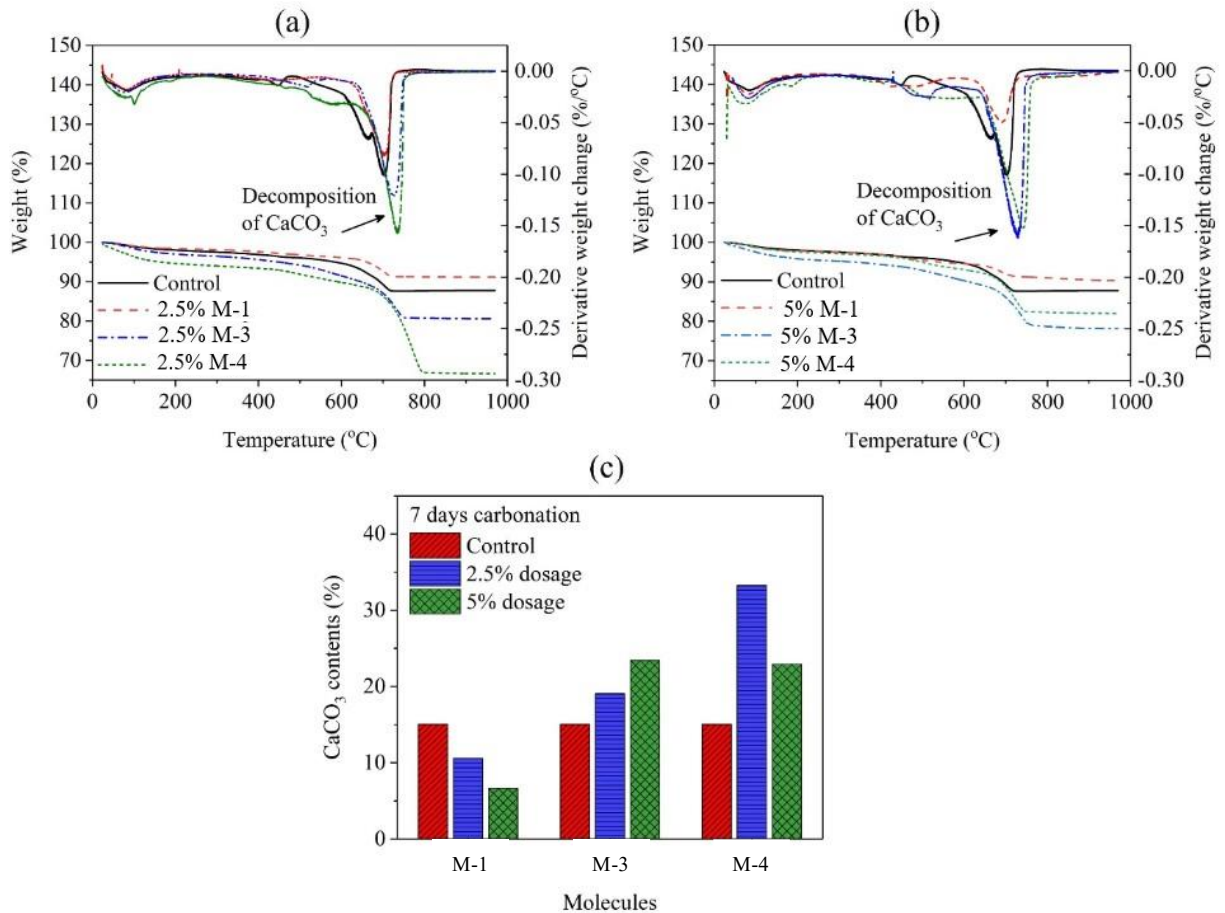
Figure 4.3: Thermogravimetric analysis of 7 days carbonated γ-C2S paste samples; (a) 2.5% batches, (b) 5% batches, (c) comparison of CaCO3 contents formation among the batches

The observed mass losses in the temperature range of 500-800°C for the 7 days cured paste samples can be attributed to the decomposition of $CaCO_3$ phases [69]. The occurrence of multiple DTG peaks within this temperature range was associated with the decomposition of various polymorphs of $CaCO_3$ [77], [91], [129]. From SEM and XRD analysis, multiple $CaCO_3$ polymorphs formation was also confirmed. The TGA results were utilized to determine the total $CaCO_3$ content that underwent decomposition in the system (**Figure 4.3 (c)).**

It was observed that with the increase of the dosage in M-1 batches, the $CaCO_3$ contents decreased. This observation matches with previous findings on the role of M-1 in carbonated wollastonite

composites [91]. For M-3 batches, the observation was opposite to that of M-1. Increasing the dosage of M-3 increased carbonate formation, and therefore, the degree of carbonation. In M-4 modified batches, 2.5% batch showed the highest amount of $CaCO_3$ contents. Accordingly, while the addition of M-1 reduced the CO_2 sequestration capacity of γ-C_2S, the other two molecules increased the sequestration capacity. The CO_2 stored in the carbonated composite increased by nearly 46% due to the addition of 5% M-3 and by around 110% due to the addition of 2.5% M-4.

4.3.2 Effects of molecules on the CaCO₃ polymorphs: Observations from XRD, FTIR and SEM

Figure 4.4 shows the XRD patterns of the 7-days carbonated γ-C_2S paste samples. The XRD pattern of the synthesized γ-C_2S matched with previously published literature [69], [130]. Both the γ-C_2S and the calcite peak are identified at a very close range (~ 29° 2θ). From **Figure 4.4Error! R eference source not found.(a)**, it is observed that 2.5% M-4 modified γ-C_2S batch showed the highest calcite peak (~ 29° 2θ). Nevertheless, 2.5% M-4 modified batch showed the formation of aragonite and vaterite as well. The other 2.5% biomimetic molecule modified batches showed comparatively less prominent calcite peak formation. However, all the 2.5% batches showed metastable $CaCO_3$ polymorphs (vaterite and aragonite) formation.

From **Figure 4.4(b)**, it can be observed that calcite peak (around 29.6^O) got reduced for the 5% molecule containing batches. With the increase of the dosage, the γ-C_2S peak intensity got decreased as well. Other metastable $CaCO_3$ polymorphs peak was also observed in the 5% batches, but those were not prominent. Aragonite formation was also observed on the control batch.

Apart from XRD, the formation of carbonate polymorphs in biomimetic molecule modified γ-C_2S binders was also investigated with FTIR spectra (**Figure 4.5**). Noteworthy, the background was

removed and only the 690 cm^{-1} to 755 cm^{-1} range was focused for this work to clearly distinguish the carbonate polymorphs. The peak at around 1450 cm^{-1} (corresponding to asymmetric stretching (ν_3) of CO_3^{2-}) are often used to identify the presence of vaterite/ACC in the carbonated composite in literature [91].
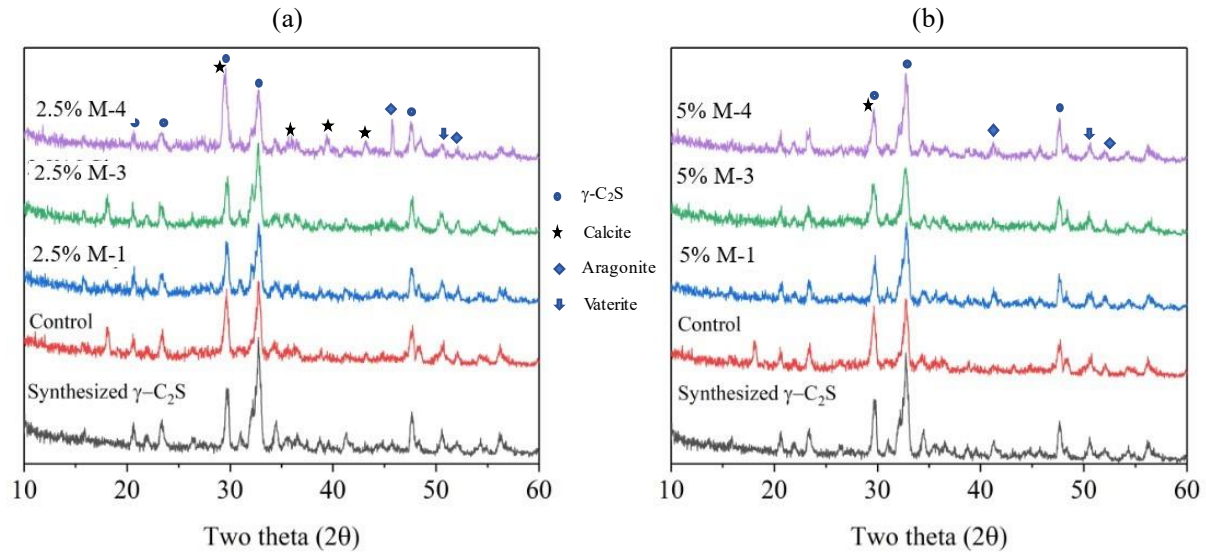
Figure 4.4: X-ray diffraction pattern of the γ-C₂S paste, (a) 2.5% batch and (b) 5% batch

However, the peak at 1450 cm^{-1} is generally overlapped by the presence of all carbonate polymorphs. The peaks in the 690 cm^{-1} to 755 cm^{-1} range shows clearly distinguishable peaks for different carbonate polymorphs. They are at 700 cm^{-1} for aragonite, at 712 cm^{-1} for calcite and at 746 cm^{-1} for vaterite (all these bands are due to the in-plane bending vibration (ν_4)) [120], [131]–[135]. ACC formation does not show any peak in this wavenumber range, and therefore, allowing clear distinction between vaterite and ACC.

From the observation, both the 2.5% and 5% M-4 and M-3 modified γ-C₂S carbonated paste samples showed calcite peak at 712 cm^{-1}. A small aragonite peak was identified in the control and 2.5% M-4 containing batches. The 2.5% M-1 batch showed low intensity calcite and vaterite peaks. However, at 5% M-1 dosage, the calcite peak disappeared and the intensity of vaterite peak

70

was significantly reduced. The absence of any peak in this range can be considered as an indication of ACC stabilization, formation of carbonates was confirmed using TGA.
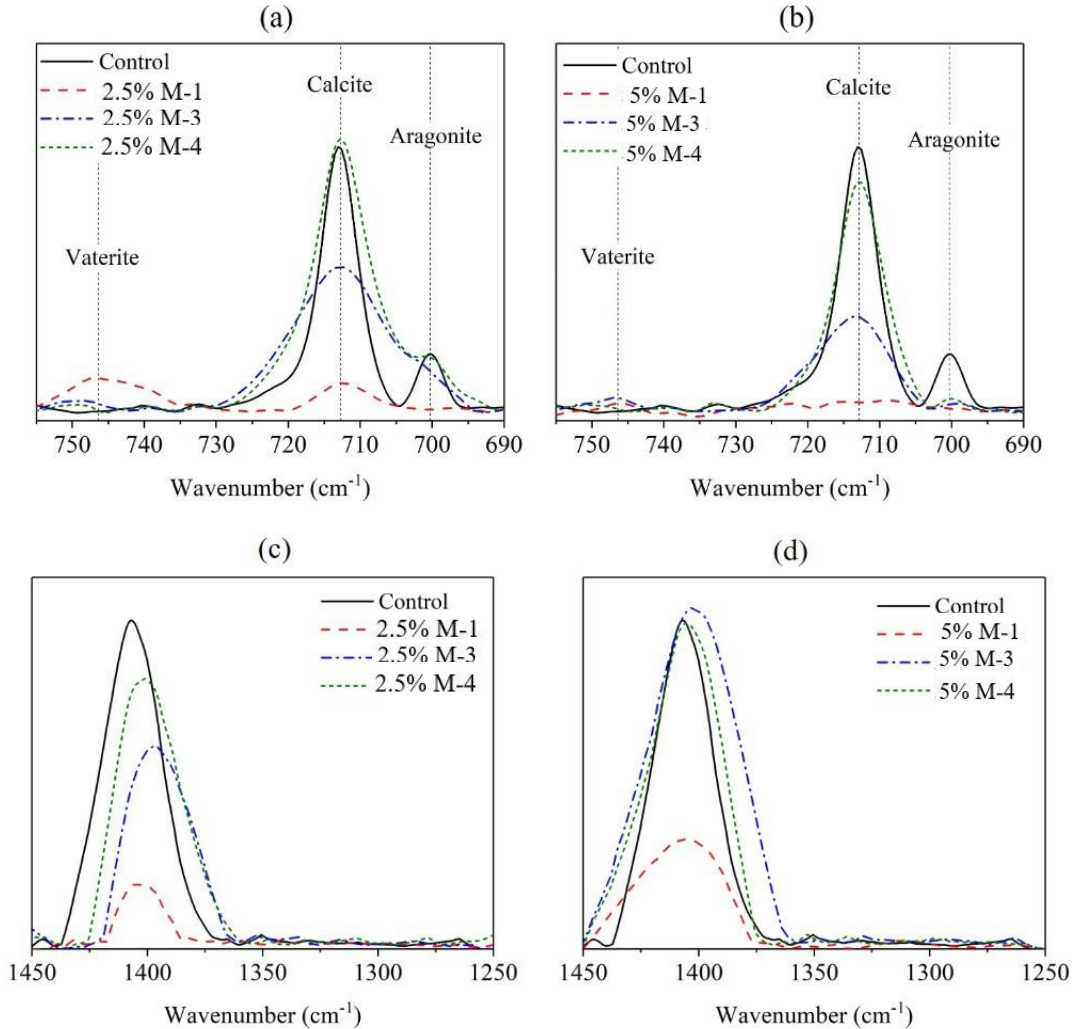
Figure 4.5: FTIR spectra of 7 days carbonated biomimetic molecules modified γ-C₂S paste samples; (a) 2.5% batch at 700-750 cm⁻¹; (b) 5% batch at 700-750 cm⁻¹; (c) 2.5% batch at 1400 cm⁻¹; (d) 5% batch at 1400 cm⁻¹

The morphology of the paste samples of gamma dicalcium silicate with and without different dosages of different biomimetic molecules was evaluated using SEM. The control sample exhibited calcite crystals with sharp rhombohedral edges (**Figure 4.6(a)**). The 2.5% M-1 (**Figure**

4.6(b)) and 2.5% M-4 (**Figure 4.6 (d)**) contained spherical ACC and vaterite phases. In 2.5% M-1 sample, the ACC spheres were larger in diameter (200 nm, 20-point average with a standard deviation of 38 nm) and agglomerated together, whereas in 2.5% M-4, the crystal sizes were smaller (60 nm, 20-point average with a standard deviation of 17 nm), and spheres were agglomerated. It was interesting to note that both 2.5% and 5% M-3 (**Figure 4.6 (c)** and **Figure 4.7(c)**, respectively) samples contained vaterite with different crystal sizes.
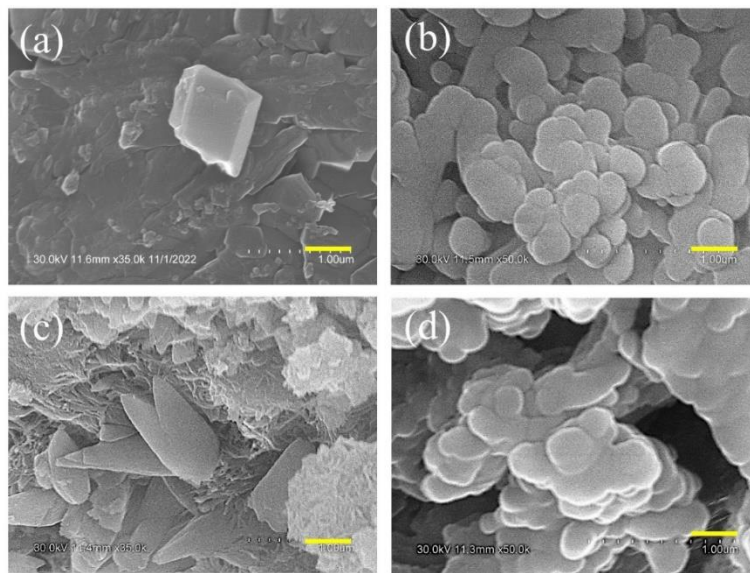
Figure 4.6: Morphology of the calcium carbonate polymorphs in (a) control, (b) 2.5% M-1, (c) 2.5% M-3, and (d) 2.5% M-4 samples. The scale bar represents 500 nm.
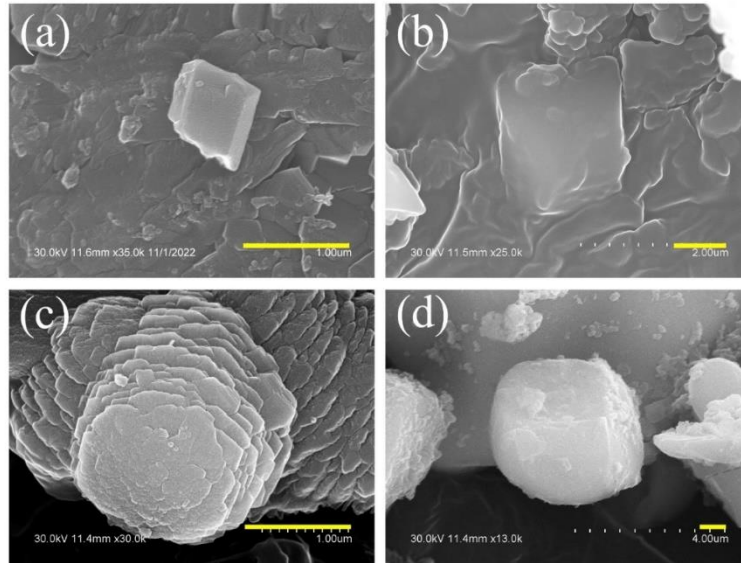
Figure 4.7: Morphology of the calcium carbonate polymorphs in (a) control, (b) 5% M-1, (c) 5% M-3, and (d) 5% M-4 samples. The scale bar represents 1 μm.

A relatively larger crystal of calcite with rounded edges compared to the control sample was observed in 5% dosages of M-1 and M-4 (**Figure 4.7(b)** and **Figure 4.7(d)**, respectively). In the 5% M-1 sample, there were no individual crystals of calcium carbonate observed throughout the sample. However, it appeared that the carbonate phases were covered with extra deposition, as presented in **Figure 4.7(b)**. Therefore, it can be concluded that smaller dosages of M-1 and M-4 were able to stabilize the ACC, whereas M-3 stabilized vaterite in all of the dosages after 7 days of carbonation.

4.3.3 Effects on the micro and nanoscale pore size distribution

Pore size distributions of the 7 days carbonated γ-C_2S composites as obtained using MIP are presented in **Figure 4.8**. Compared to the control batch, the addition of 2.5% M-3 increased the total porosity by 19% and also reduced the critical pore diameter. The addition of 2.5% M-4 and 2.5% M-1 reduced the total porosity by 23% and 5%, respectively compared to the control batch. Therefore, the addition of these molecules enabled the formation of a denser microstructure. The

73

addition of 5% M-1 showed nearly the same total porosity as compared to the control batch, however with a significant increase in the large porosity. Such formation of large porosity is due to the reduced degree of carbonation (as observed from TGA) after the addition of 5% M-1. The 5% M-3 containing batch showed a reduced porosity compared to the control batch. The addition of 5% M-4 resulted in an increase of the total porosity without altering the critical pore size compared to the control batch. The pore size distribution as obtained from MIP matches well with the observations from TGA. Specifically, at 2.5% dosage, M-4 showed the highest degree of carbonation and the lowest total porosity. In the case of 5% dosage, M-3 showed the highest carbonate formation and the lowest total porosity.

Figure 4.8: Effects of biomimetic molecules on pore size distribution of 7 days carbonated γ-C_2S paste samples

The nano pore size distributions of the carbonated γ-C_2S composites with and without the biomimetic molecules are shown in **Figure 4.9**. Compared to the control batch, the addition of

2.5% M-3 increased the total porosity by 19% and also reduced the critical pore diameter. The addition of 2.5% M-4 and 2.5% M-1 reduced the total porosity by 23% and 5%, respectively compared to the control batch. Therefore, the addition of these molecules enabled the formation of a denser microstructure. The addition of 5% M-1 showed nearly the same total porosity as compared to the control batch, however with a significant increase in the large porosity. Such formation of large porosity is due to the reduced degree of carbonation (as observed from TGA) after the addition of 5% M-1. The 5% M-3 containing batch showed a reduced porosity compared to the control batch. The addition of 5% M-4 resulted in an increase of the total porosity without altering the critical pore size compared to the control batch. The pore size distribution as obtained from MIP matches well with the observations from TGA. Specifically, at 2.5% dosage, M-4 showed the highest degree of carbonation and the lowest total porosity. In the case of 5% dosage, M-3 showed the highest carbonate formation and the lowest total porosity.

From these graphs, three major peak locations were noticed. They are at 5 Å, 8 Å and 11.5 Å. The peak location at 11.5 Å is the corresponding peak due to the porosity of the interlayers in calcium silicate hydrates (CSH) or Ca-modified silica gel structures [131]. After the addition of the biomimetic molecules, no peak shift was occurred which indicates the biomimetic molecules do not affect the silicate structure. However, addition of these biomimetic molecules resulted in reduced interlayer porosity indicating lower amount of CSH/Ca-modified silica gel formation. The specific surface area is correlated with the quantity of water-accessible fine pores [127]. The specific surface area (S_{BET}) of fully hydrated cement paste is approximately 100-200 m^2/g [136]. The carbonated calcium silicates are known to have lower S_{BET} compared to the hydrated cement paste[137]. As observed from **Figure 4.9** (c) and (d), the addition of biomimetic molecules decreased the specific surface area of the carbonated matrices compared to the control batch. In a

past study [137], it was reported that the formation of metastable carbonates shows a lower surface area compared to the matrix primarily containing calcite.
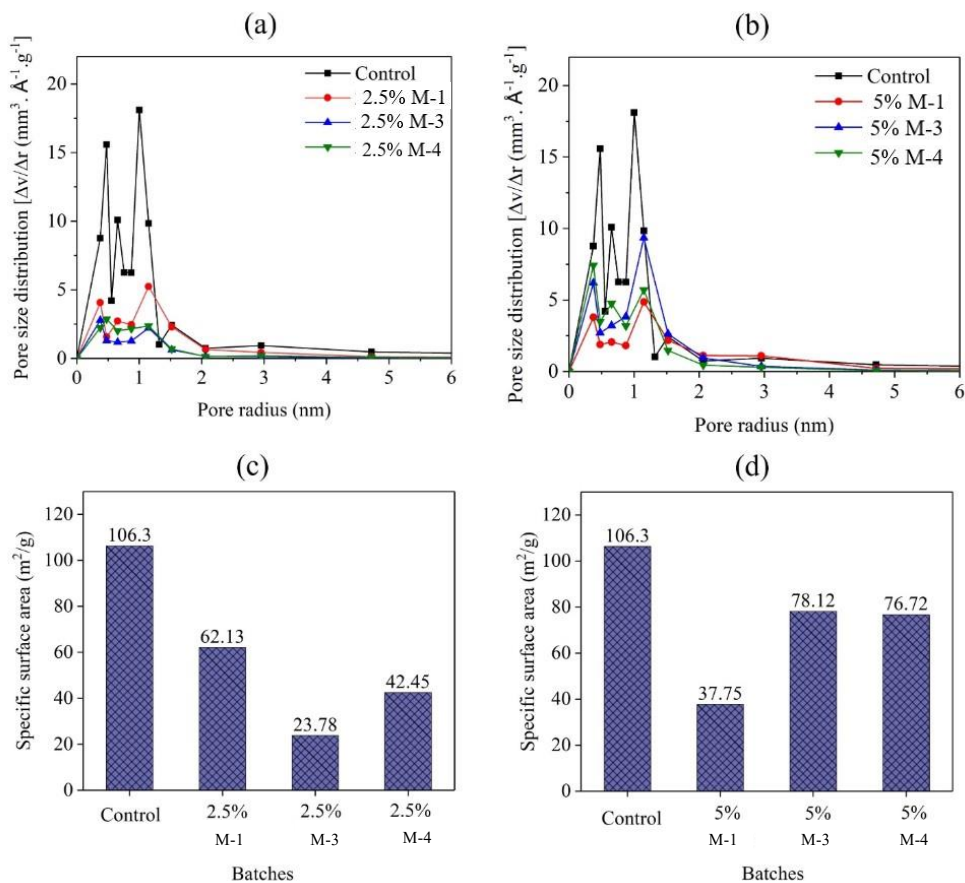
Figure 4.9: Pore size distribution (a) 2.5% batch and (b) 5% batch; specific surface area (c) 2.5% batch and (d) 5% batch

This is because the stabilization of typical metastable carbonates (vaterite and ACC) often occurs due to the coating of the particle by silica gel or the biomimetic molecules. Such a process makes the surface area of the metastable carbonated inaccessible by water molecule and therefore, shows a lower surface area measurement. Accordingly, the reduced surface area in the cases of M-3 and M-4 containing batches can be attributed to the formation (and stabilization) of typical metastable carbonates and agglomeration of carbonate particles as observed in the SEM. In the case of M-1

containing batch, the reduced surface area can be attributed to the similar agglomeration of the phases along with reduced degree of carbonation as observed from the TGA.

4.3.4 Effects on Nanomechanical properties

Grid nano-indentation technique was applied to each sample over two 60 μm x 60 μm sections, with a total of 200 indentations. **Figure 4.10** shows the elastic modulus (GPa) frequency distribution for the control and biomimetic molecules-modified γ-C_2S paste samples after 7 days of carbonation period. According to previous literature, the elastic moduli of Ca-modified silica gel and $CaCO_3$ present in carbonated cured cementitious composites are around 32-42 GPa and 54-79 GPa, respectively [65], [77], [138]–[140]. Additionally, carbonated calcium silicates form a composite phase by the mixture of $CaCO_3$ and Ca-modified silica gel, which shows the mean elastic modulus of around 40 GPa [139]. Noteworthy, due to the formation of different $CaCO_3$ polymorphs, the range of $CaCO_3$ elastic modulus is wide. The elastic modulus are 39 GPa, 67 GPa and 72 GPa for aragonite, vaterite and calcite, respectively [141].

From **Figure 4.10 (a)**, it can be observed that the control batch contains tentatively two peaks: one at around 22 GPa, corresponding to HD C-S-H or Ca-modified silica gel and another around 30 GPa, which can be attributed to the carbonate phases with and without mixing with the gel. The 2.5% M-1 containing batch showed a single peak at around 30 GPa elastic modulus, indicating the formation of a single hybrid phase instead of two microstructure phases. The mean modulus due to the addition of 2.5% M-1 was increased by 8.5%. In the case of 2.5% M-3 containing batch, two peaks corresponding to the gel and carbonate phases are clearly visible.

However, the elastic modulus corresponding to the carbonate phase (~ 40 GPa) was higher in this batch compared to that of the control batch. The mean modulus of the 2.5% M-3 containing batch

was 3.5% higher than the control batch. The frequency distribution plot for 2.5% M-4 containing batch was similar to that of the 2.5% M-1 batch, as this sample also showed a single peak instead of separate carbonate and gel phases. Therefore, the addition of 2.5% M-4 also led to the formation of hybrid phase, i.e., mixture of silica gel and different $CaCO_3$ polymorphs.
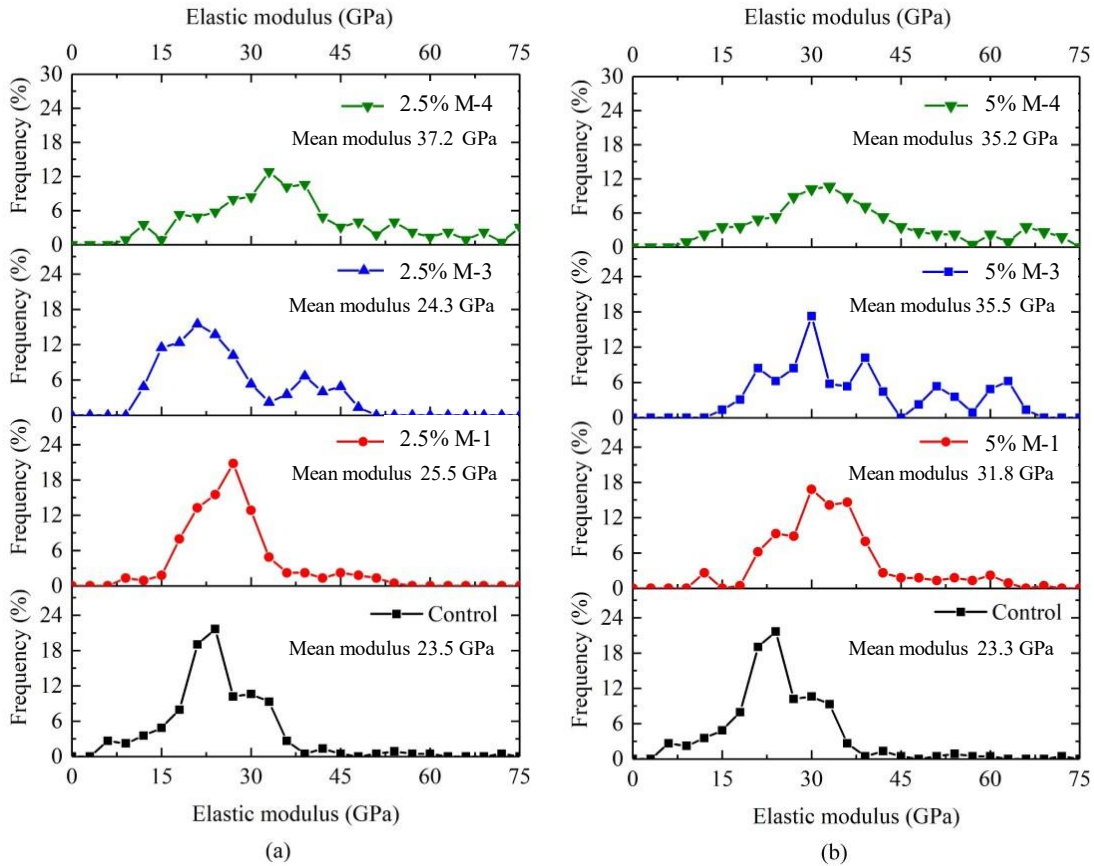
Figure 4.10: Percent frequency versus elastic modulus (a) 2.5% batches, (b) 5% batches

All of the molecules at 5% dosage showed an increase in the elastic modulus compared to the control batch. Specifically, the highest mean modulus was obtained for the batch containing 5% M-3 batch. This study confirms that all of the molecules can effectively enhance the nanomechanical properties of the carbonated γ-C_2S composites.

4.3.5 Effects on Compressive and flexural strengths at 25°C (room temperature)

Figure 4.11(a) and (b) exhibits the compressive and flexural strength properties of the 7 days carbonated γ-C_2S paste samples with and without the addition of biomimetic molecules. **Figure 4.11(a)** shows that 2.5% M-4 and 5% M-1 modified γ-C_2S paste samples resulted in 61% and 52% higher than the control batch, respectively. Not only these two batches, but all other biomimetic molecules also modified batches increased the compressive strength as well. **Figure 4.11(b)** shows the flexural strength properties of the 7 days carbonated paste samples. Both 2.5% and 5% dosage increased the flexural strength in the carbonated cementitious system.
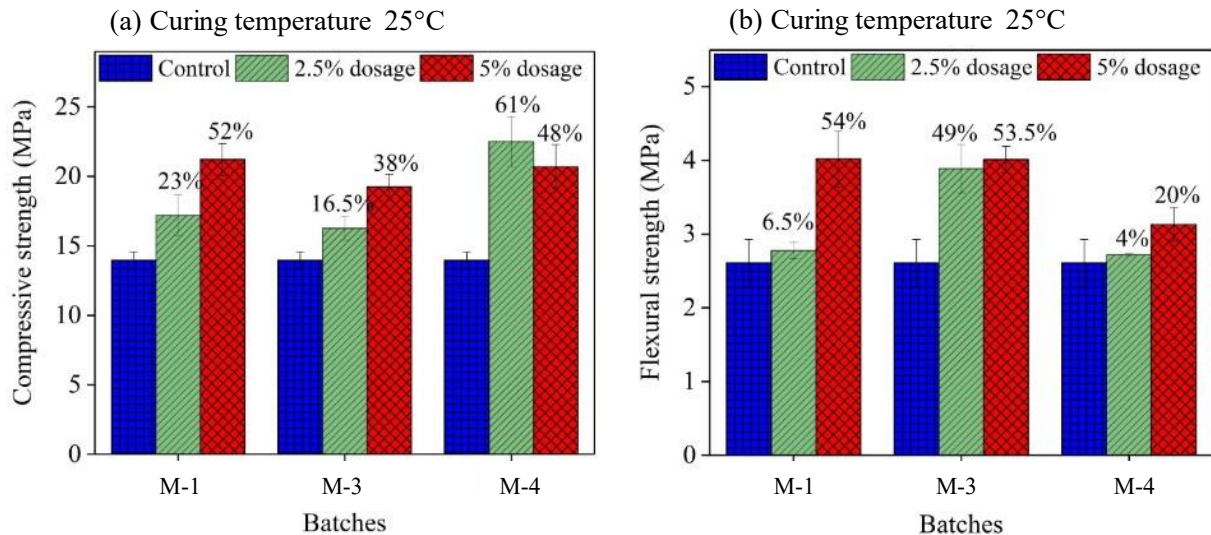
Figure 4.11: (a) Compressive strength and (b) flexural strength at 25°C curing (after 7 days of carbonation period)

The flexural strength of the beam samples got increased by 54% by the addition of 5% M-3 and 5% M-1. Even though M-1 modified batch did not show significant $CaCO_3$ polymorphs formation in the microstructure, it enhanced the strength properties because of the adhesion characteristics of aspartic acid [142]–[144].

4.3.6 Effects of elevated temperature (50°C) on strength properties
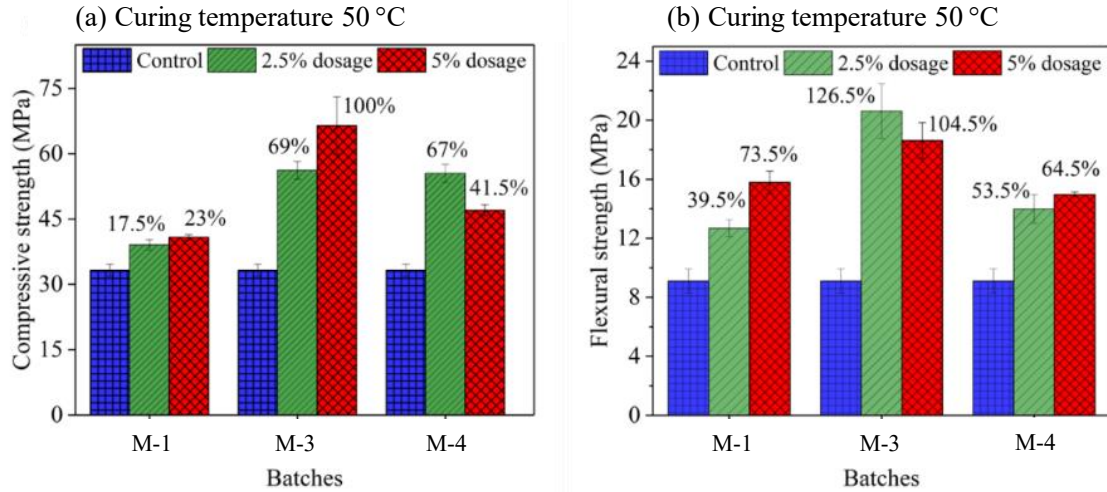
Figure 4.12: (a) Compressive strength and (b) flexural strength (cured at 50°C temperature and after 7 days of carbonation period)

Another set of samples were cured at elevated temperature (50°C) to observe the effect of temperature curing on the samples. It was observed that elevated temperature enhanced strength gain for both compressive and flexural strength to a great extent. From **Figure 4.12**(a), the results revealed a substantial improvement in strength with increasing temperature. Of particular interest is the effect of different additives, specifically 5% M-1 and 2.5% M-3, on the strength gain compared to the control batch.

When exposed to elevated temperature curing, 5% M-3 demonstrated the most significant strength enhancement, exhibiting a remarkable 100% increase in strength compared to the control batch. Additionally, 2.5% M-3 exhibited a substantial improvement, with a 69% increase in strength.

Conversely, the M-1 batches did not exhibit any noticeable improvement in strength when subjected to elevated temperature curing. This suggests that the efficacy of M-1 diminishes under

high-temperature curing conditions. In contrast, the M-4-induced batches displayed a similar percentage increase in compressive strength compared to the batches cured at ambient temperature, indicating that the effects of M-4 are consistent regardless of curing temperature.

The influence of temperature (50°C) curing on the flexural strength properties of the biomimetic molecules-induced batches is depicted in **Figure 4.12(b)**. It was evident that the batches subjected to high-temperature curing exhibited improved flexural strength when compared to their counterparts cured at ambient temperature.

Among all the batches, the 2.5% M-3 modified batch demonstrated the most significant increase in flexural strength, registering an impressive 126.5% improvement compared to the control batch. Similarly, the 5% M-3 induced batch exhibited a noteworthy increase of 104.5% in flexural strength. Interestingly, the M-4 modified batches, in contrast to previous observations, displayed a higher increase in strength when exposed to elevated temperature curing, with increments of 53.5% and 64.5% compared to the control batch. Furthermore, the 5% M-1 modified batch also showed a notable improvement in flexural strength, achieving a 73.5% increase.

These findings underscore the positive impact of high-temperature curing on the flexural strength properties of the biomimetic molecules-induced batches, with specific additives such as M-3, M-4, and M-1 contributing significantly to these enhancements.
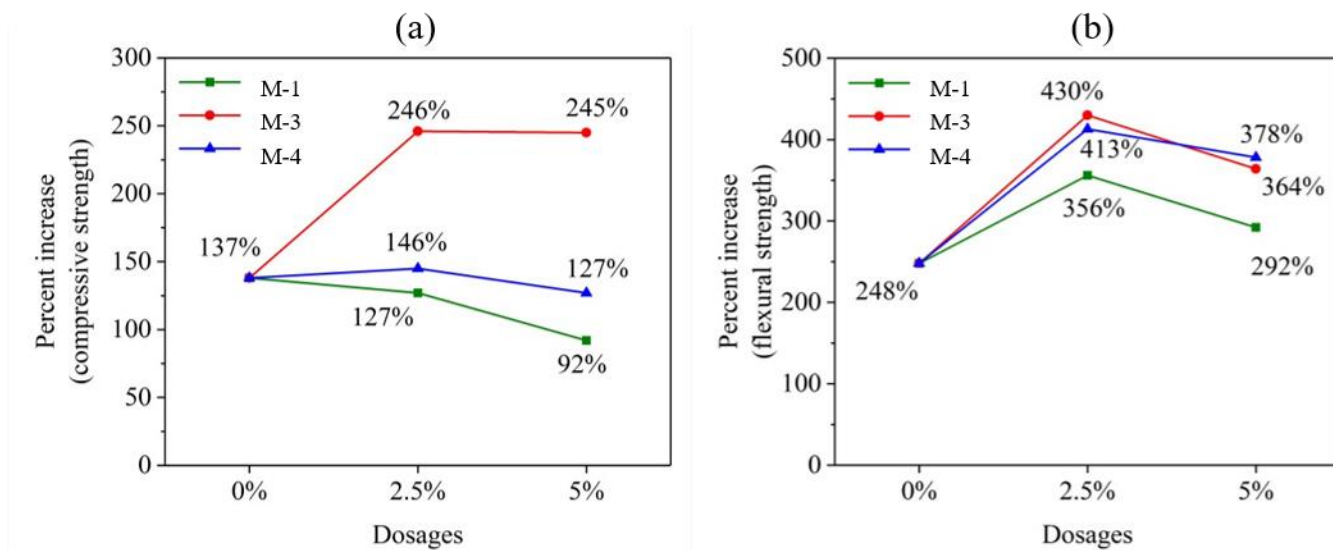
Figure 4.13: Percent increase of strength after applying temperature curing (a) compressive strength, (b) flexural strength

Figure 4.13 is showcasing the percent increase of the strength compared to the room temperature cured batches. **Figure 4.13**(a) shows that, 2.5% M-3 batches improved both compressive strength and flexural strength properties to the maximum. For compressive strength, the percent increase is almost same for the 2.5% and 5% batches. However, for the flexural strength (**Figure 4.13(b)**), 2.5% dosage batches enhanced the strength maximum compared to the 5% induced batches.

4.4 Discussions

This study showed that the selected biomimetic molecules can affect the amounts and polymorphs of the carbonates form in the carbonated γ-C_2S composites. However, effects of these molecules are substantially different due to their different characteristics including surface charge and chain lengths. The observed role of M-1 on carbonated γ-C_2S composites is similar to those observed in the case of carbonated wollastonite [91]. Specifically, with the increasing amounts of M-1, an increase in the mechanical performance was observed, even though the degree of carbonation was

reduced. The negatively charged M-1 forms complex phases with Ca^{2+} surface sites of $CaCO_3$ and subsequently, stabilizes typical metastable polymorphs of $CaCO_3$, including vaterite and ACC, which cause the strength enhancement due to the addition of this molecule [91]. However, due to the same mechanism, M-1 can also form complex with the Ca^{2+} surface sites of γ-C_2S and therefore, reduced the reacting surface area resulting in a reduced degree of carbonation. While M-3 is also negatively charged as that of M-1, the effects of M-3 on the carbonated γ-C_2S composites were different. The increased dosage of M-3 enhanced the mechanical performance as well as the degree of carbonation of the composites, and therefore making M-3 a more effective admixture for γ-C_2S compared to the M-1. Such differences in the roles of M-1 and M-3 are due to their different chain length and solubility. A higher solubility limit is likely to make M-3 more effective in controlling the carbonate polymorphs.

The role of M-4 in carbonated composite is different than that of the M-3 and M-1. Worthy to note, M-4 is also negatively charged molecule and a very well-known viscosity modifying admixture for Portland cementitious materials [145], [146]. In the case of Portland cement paste, the negatively charged M-4 can be adsorbed on the surface of cement particles, which stabilizes the particles in water and therefore, improves the workability of the mixture [145], [146]. M-4 is also well-known for its ability to alter the $CaCO_3$ crystallization pathway [147], [148]. M-4 can enable forming $CaCO_3$ with variable crystal shapes, sizes, and polymorphs (vaterite, aragonite, ACC) depending on the dosage, molecular weight, and temperature [147]–[149]. At 2.5% dosage, M-4 increased the compressive strength of the composite by 61% and CO_2 sequestration capacity by nearly 110%. Unlike M-1 and and M-3, the addition of 2.5% M-4 enabled the stabilization of aragonite (observation from FTIR and XRD). Accordingly, the enhanced role of M-4 compared to the M-1 and M-3 was attributed to its ability to stabilize aragonite. However, with an increased

dosage (5%) of M-4, the strength and CO_2 sequestration capacity were reduced compared to the 2.5% dosage (remained higher than the control and similar to 5% M-3). This performance reduction at high dosage of M-4 was attributed to the excessive adsorption of this molecule on γ-C_2S surface.

To sum up, a variety of organic molecules have been used in the past to mimic the biomineralization process of stabilization of $CaCO_3$ polymorphs in carbonation cured calcium silicates [91], [150]. The application of all of these molecules resulted in improved mechanical performances of the carbonated composites but reduced the CO_2 sequestration in those composites [91], [150]. One of the most interesting observations of the presented study is that both M-3 and M-4 were able to enhance the mechanical performance of the composites while also increasing the amounts of CO_2 sequestered in the carbonated γ-C_2S composites.

4.5 Conclusions

The following are the concluding remarks from the present study:

i.   From XRD, γ-C_2S formation is verified with prominent peaks. It indicates the proper laboratory synthesis of the γ-C_2S materials.

ii. FTIR in the 700 cm^{-1} wavenumber range showed that M-1 batches showed delayed calcium carbonate formation.

iii. TGA results showed that M-4 and M-3 formed higher amount of calcium carbonate formation compared to the control batch. Addition of biomimetic molecules accelerated the degree of reaction.

iv. Among the batches, both 5% M-1 and 5% M-4 batches showed an increase of compressive strength by around 50%. 2.5% M-4 increased the strength by around 60%.

v. From nanoindentation results, 5% M-1 and 5% M-3 showed improved modulus of elasticity. However, all the 2.5% batches showed higher mean modulus of elasticity compared to the control batch.

vi. 2.5% M-4 produced the highest amount of calcium carbonate contents and resulted in the highest compressive strengths at room temperature.

vii. At a curing temperature of 50°C, both 2.5% and 5% M-3 demonstrated substantial enhancements in both compressive and flexural strength. Specifically, the addition of 2.5% M-3 resulted in a 69% increase in compressive strength and a remarkable 126.5% improvement in flexural strength. Similarly, the incorporation of 5% M-3 led to a doubling of compressive strength (100%) and a notable increase of 104.5% in flexural strength.

Chapter 5: Role of different molecular weight of M-4 on performance enhancement of carbonated beta-dicalcium silicates (β-C₂S)

5.1 Research objectives

In recent years, the imperative need for environmentally sustainable construction practices has intensified, driven by growing concerns over the substantial carbon footprint associated with ordinary Portland cement (OPC). As a pivotal component of concrete, OPC holds the distinction of being the second most utilized substance worldwide, just after water [151]. The staggering statistics from 2015, with a total cement mass of 4.6 billion tons and a per capita average of 626 kg, resulting in the production of 2.1–2.3 m^3 of cement-based materials, underscore the scale of its impact [152]. The production of OPC is further compounded by its significant contribution to global CO_2 emissions, accounting for 7%–10% of anthropogenic CO_2 emissions and 2%–3% of energy consumption [151], [153], [154]. Disturbingly, projections indicate a 50% increase in cement production by 2050, with an additional 85–105 Gt of CO_2 emissions anticipated [153].

The primary source of CO_2 emissions in OPC production stems from the calcination of raw materials, notably limestone, in the kiln feed, as well as energy-derived CO_2 from fuel consumption during feed heating [155]. Consequently, the quest for sustainable alternatives has driven the development of low carbon footprint cementitious systems. These systems exploit non-hydraulic low-lime phases such as calcium silicates, which exhibit remarkable reactivity in the presence of CO_2 [66]–[68]. Utilizing these low-lime calcium silicates offers a promising solution to reducing the carbon footprint associated with cement production, primarily by decreasing the demand for limestone and the temperature requirements for clinker production [156].

In this context, it is paramount to recognize that C_2S, constituting approximately 15 wt% of cement clinker, is integral to the long-term properties of cement [157]. Traditionally, C_3S, accounting for

about 65 wt% of cement clinker, has been favored over C_2S for its rapid hydration and early strength development [66], [158]. However, C_2S has the potential to reduce limestone consumption, save energy, and mitigate CO_2 emissions. Enhancing the early strength development of C_2S has led to the exploration of carbonation technology, which accelerates mineral transitions in C_2S and sequestrates CO_2 into chemically stable carbonates for extended periods [30].

A pivotal distinction arises from the various polymorphs that C_2S can adopt, including α, αH', αL', β, and γ, each influenced by chemical impurities and cooling transition temperatures [159][160], [161]. Among these, β-C_2S emerges as the principal mineral component of Portland cement, reacting with water to contribute to medium and long-term strength development. Both β-C_2S and γ-C_2S have demonstrated their ability to sequestrate CO_2 and generate $CaCO_3$ and gel phases, thereby contributing to early strength development [30], [162], [163]. The distinction between the carbonation properties of β-C_2S and γ-C_2S has been subject to rigorous investigation [164], underscoring the potential for optimizing their performance by understanding and controlling the associated variables [163] [165] [166].

The mechanical properties of carbonated cement composites are significantly influenced by the formation of different $CaCO_3$ polymorphs. Among these, amorphous calcium carbonate (ACC) serves as the precursor, transitioning into metastable phases such as vaterite or aragonite before ultimately stabilizing as calcite [72], [167]. These metastable phases play a pivotal role in enhancing mechanical strengths, making the controlled regulation of polymorph formation a critical factor in achieving improved carbonated cementitious properties. Yet, this control is inherently challenging due to a multitude of variables, including humidity, temperature, CO_2 concentrations, water content, and more [70], [168]–[170].

Apart from the precise calibration of these parameters, organic molecules have shown promise in influencing polymorph formation in carbonated cementitious composites. While previous research has explored the use of amino acids for this purpose, M-4 presents a viable alternative, given its demonstrated capacity to influence the crystallization of $CaCO_3$ [92]. However, the inclusion of M-4 in cement paste has primarily aimed to enhance fluidity, with limited studies delving into its full potential [171], [172]. Crucially, M-4 is available in a wide range of molecular weights (MW), and the selection of MW can significantly impact biomimetic mineralization processes [173], [174].

Notably, a study by Haque et al. previously introduced M-1, M-2, and M-4 into γ-C_2S, highlighting the substantial role of M-4 with a molecular weight of 5000 (MW 5000) in enhancing carbonation properties under high-temperature conditions. However, this research spotlighted the influence of temperature, particularly relevant to γ-C_2S's non-hydraulic nature. Given that β-C_2S possesses greater hydraulic properties than γ-C_2S, it becomes imperative to investigate the effects of incorporating various molecular weights of polyacrylic acid to enhance the carbonation properties of β-C_2S. This study, therefore, aims to elucidate the specific influence of different MWs of M-4 on enhancing the carbonation properties of β-C_2S, ultimately paving the way for more efficient and cost-effective construction materials while addressing significant environmental concerns as belite based cement can play a great role to reduce the CO_2 emission from the cement-concrete industry [153], [175], [176].

The research objectives are –

(i) Can different molecular weight of M-4 enhance the properties of carbonated β-C_2S?

(ii) How does the different dosage of M-4 affect the properties of carbonated β-C_2S?

5.2 Materials and methods

5.2.1 Raw materials and sample preparation

Numerous methodologies are available to produce pure calcium silicate phases [121]–[123]. Most of these approaches entail the utilization of sintering to process a precise mixture of lime and silica. In our investigation, we employed $CaCO_3$ with a purity exceeding 99% and fumed silica with a purity exceeding 99% to create β-C_2S. To make β-C_2S formation stable, 0.3% boron was incorporated as dopant by the addition of Boric Acid (H_3BO_3) since previous studies showed that such dosage of boron stabilizes the beta-polymorph of C_2S by lattice distortion and changing the morphology [177]–[180]. We employed three different molecular weights (MW) of M-4 molecules in our research, specifically M-4 with MW 2000 (in a 63 wt% aqueous solution), M-4 with MW 5000 (in a 50 wt% aqueous solution), and M-4 with MW 240000 (in a 25 wt% aqueous solution). All these raw materials and biomimetic compounds were procured from VWR.

A homogeneous blend of $CaCO_3$ and fumed silica was prepared with a molar ratio of 2:1. 0.3% (by wt percent of the $CaCO_3$ and silica contents) boron dopant was added in the form of boric acid. To aid the mixing process, the water-to-binder (w/b) ratio was maintained at 0.50. The resulting paste mixture was utilized to create 1-inch cube specimens, which were placed in a 40°C oven for a duration of 6 hours. Subsequently, these cube specimens were positioned inside a high-temperature furnace and subjected to sintering at 1400°C for a duration of 4 hours. Following this, they were allowed to cool, and the sintered products were pulverized using a readily available ball mill. The resulting powdered material was then reconstituted into a paste and formed into 1-inch cubes once more. These cubes were once again placed inside a 40°C oven for 6 hours and then placed inside the furnace at 1400°C for another 4-hour sintering cycle. Ultimately, the sintered products were collected after cooling down, ensuring the stabilization of β-C_2S. Following

sintering, the resultant products underwent a grinding process and were passed through a #200 mesh (74 μm) sieve. To enhance the chemical interaction between the present lime and silica, the resulting powder underwent two firing cycles. Finally, X-ray diffraction (XRD) analysis was conducted after each sintering cycle to confirm the absence of any residual free lime components (XRD results are shown in the Results and Discussion section).

The particle size distribution and the X-ray diffraction results of the synthesized β-C_2S are shown in Figure 4.1. This confirms the well synthesis of the raw materials containing some impurities of γ-C_2S. The XRD pattern matches with previous studies [162], [164], [181]. The SEM image of raw b-C_2S shows round smooth shape.
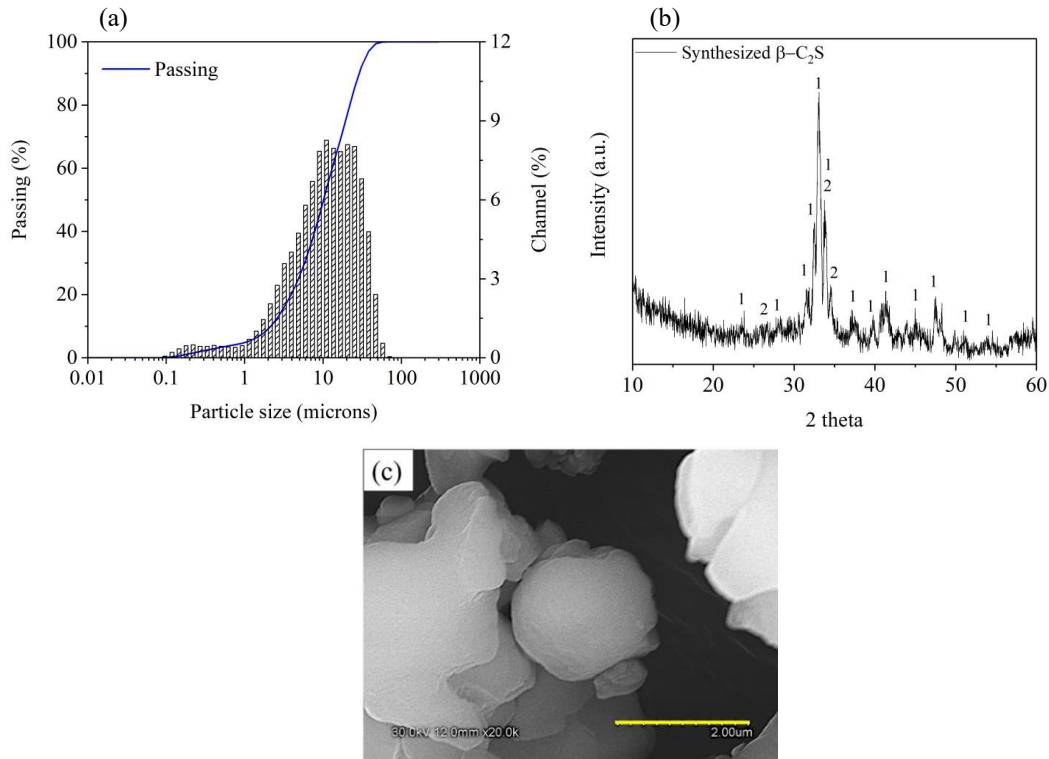
Figure 5.1: (a) Particle size distribution of synthesized β-C_2S; (b) XRD plot of synthesized β-C_2S (1: β-C_2S peak, 2: γ-C_2S peak); (c) SEM image of raw β-C_2S (scale bar represents 2 μm)

Two distinct sets of samples were fabricated for the purpose of carbonation curing: (i) thin discs, cut from paste samples measuring approximately 5 mm in thickness and 20 mm in diameter, and (ii) compacted paste cubes and beam samples. The first set of samples was used to track the formation and evolution of $CaCO_3$ polymorphs and to assess microstructural properties during the carbonation period. The second set was prepared for the analysis of mechanical strength and pore size distribution. To create the paste samples, biomimetic molecules were initially mixed with water at concentrations of 0.5%, 1%, and 2.5% by weight percentage of β-C_2S. The control batch did not contain any biomimetic molecules. The β-C_2S powder was then blended using a high shear mixer at 350 rpm for 2 minutes. The water-to-binder (w/b) ratio was maintained at 0.40 throughout the experimental process. Subsequently, the samples were placed inside a commercially available carbonation chamber with a set relative humidity of 80%, CO_2 concentration of 20%, and room temperature (25°C) for different durations.

Another set of cube and beam samples was prepared (1% dosage batch) to investigate the influence of temperature curing on strength performance. These samples were placed within a carbonation chamber with conditions set at 80% relative humidity, 20% CO_2 concentration, and a temperature of 50°C for 3 days and 7 days.

5.2.1 Test methods

The thermal gravimetric analysis (TGA) experiment on the paste sample was done using a commercially available TGA 550 instrument from TA Instruments. The paste samples, previously stored in a vacuum desiccator, were utilized for this analysis. To prepare the samples, they were manually ground with a mortar and pestle until a fine powder was achieved. Approximately 30-35 mg of the powdered material, having passed through a #200 sieve, was loaded into a platinum pan.

The pan was then subjected to an isothermal condition at 25°C for 5 minutes before gradually increasing the chamber temperature to 980°C at a rate of 15°C per minute. To maintain an inert atmosphere, nitrogen gas was purged throughout the procedure.

To confirm the uniformity of carbonation among the samples, the TGA test was initially conducted using three replicate samples. The results exhibited a variation of less than 2% in terms of total carbonation, indicating excellent reproducibility. Consequently, for the subsequent batches, TGA was carried out using a single sample due to the low level of variability.

The microstructures of the carbonated β-C_2S pastes were examined through the utilization of a Hitachi S4800 II FE-SEM. This instrument operated in a high-vacuum mode, applying a 30-kV accelerated voltage and maintaining a working distance of roughly 11 mm. Prior to acquiring SEM images, the cement paste sample was coated with a layer of Gold (Au) and Platinum (Pt). The analysis was carried out on the fractured surface of the paste samples.

In-situ FTIR spectra of the powdered paste sample were acquired utilizing the Attenuated Total Reflection (ATR) mode, with a resolution of 4 cm^{-1}, and involving 32 scans for each individual sample. The signal-to-noise ratio was held below 3:1. A total of 280 spectra was collected at an interval of 3.75 mins maintaining 99% CO_2 purging. The in-FTIR analysis was conducted on the 1% dosage batches of MW 2000, MW 5000 and MW 240000 along with the control batch.

Samples of carbonated paste collected after 7 days were subsequently milled in preparation for X-ray diffraction (XRD) analysis. These powdered samples were loaded into a Bruker D8 spectrometer, utilizing Cu Kα radiation (40 kV, 40 mA). The diffraction patterns were then recorded within a 2θ range of 10° to 60°, with a step size of 0.03 (2θ) per second.

For phase identification through X-ray diffraction (XRD), a commercially available software known as "Match! Phase Analysis using Powder Diffraction" was employed. The reference PDF

card numbers utilized were as follows: PDF #96-900-0967 for calcite, PDF #96-901-3802 for aragonite, PDF #96-150-8972 for vaterite, and PDF #96-154-6026 for γ-C_2S. For, β-C_2S, previously published [164], [181] literature was matched.

The Micrometrics Instrument Corporation AutoPore IV 9500 V2.03.01 apparatus was employed for conducting Mercury intrusion porosimeter (MIP) experiments on cementitious composites. This technique is utilized for assessing the architecture of both meso-porous materials (pore radius 2~50 nm) and macro-porous materials (> 50 nm). The MIP test was performed on three distinct sets of samples: the control batch and paste samples with 2.5% and 5% dosages, all subjected to 7 days of carbonation curing. The sample dimensions were standardized to $15 \times 15 \times 15$ mm.

In the MIP experiment, mercury was used with a surface tension of 0.485 N/m and an average contact angle of 130° with respect to the pore wall. The maximum applied pressure reached 413 MPa, enabling the investigation of pores with diameters as small as 3.02 nm. This analysis aids in characterizing the pore structures of the cementitious composites under varying dosage conditions following the carbonation curing period.

The measurement of compressive strength was conducted using a Gilson compressive strength testing machine, with a loading rate of 450 N/s. On the other hand, flexural strength, determined through the 3-point bending test, was assessed using a custom-made micro-mechanical tester with a displacement rate of 0.1 mm/min.

After 3 days and 7 days of carbonation curing, the compressive and flexural strength of paste samples were examined. The cube-shaped samples had dimensions of 25 mm $\times$ 25 mm $\times$ 25 mm, while the beam-shaped samples measured 40 mm $\times$ 20 mm $\times$ 15 mm.

5.3 Results

5.3.1 Reaction product formation and CO₂ sequestration (findings from TGA and SEM)
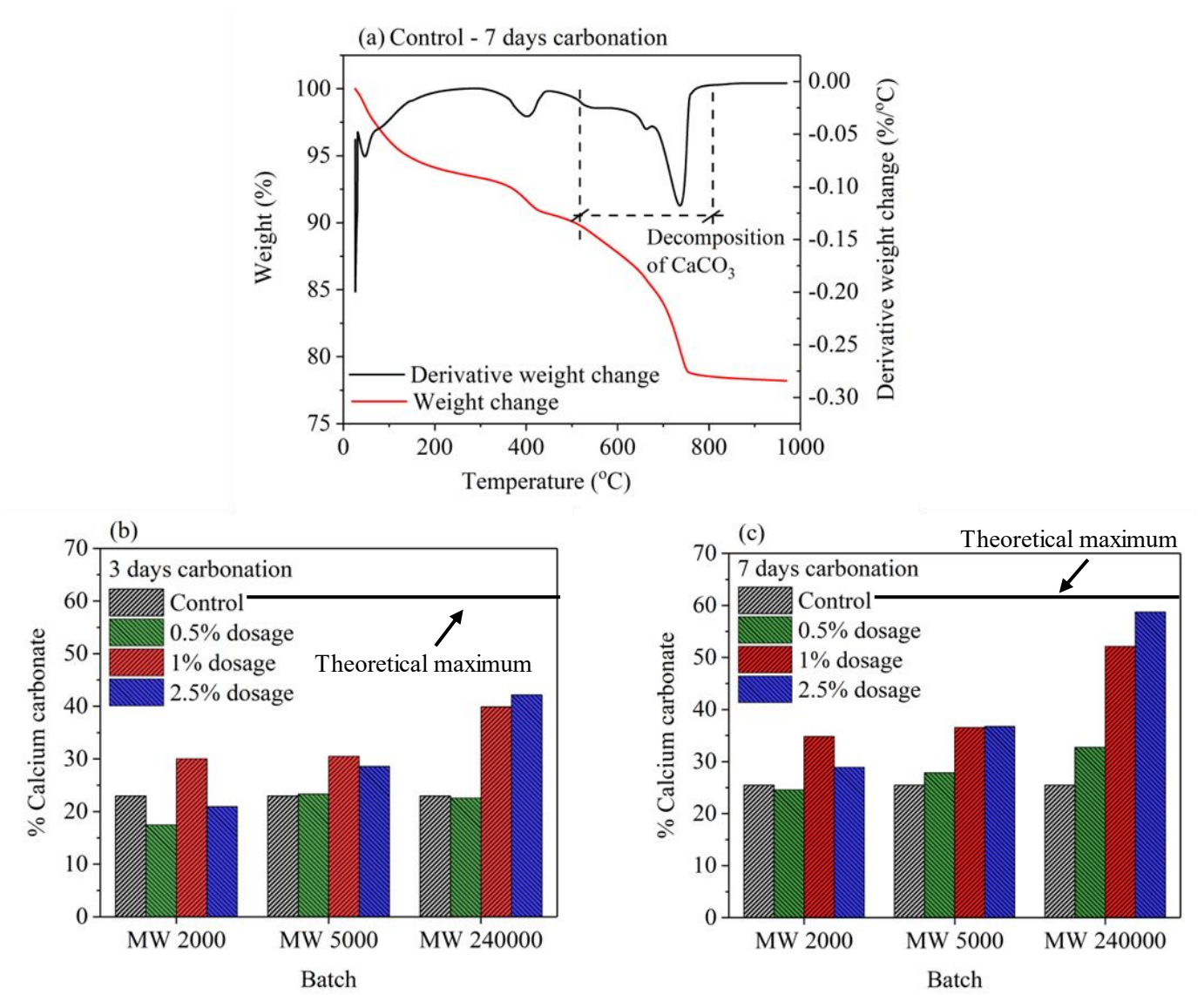
Figure 5.2: Thermogravimetric analysis of 3 days and 7 days carbonated β-C₂S samples; (a) representative TGA-DTG plot; (b) percent CaCO₃ formation of different batches after 3 days carbonation; (c) percent CaCO₃ formation of different batches after 7 days carbonation.

In **Figure 5.2(a)**, a representative TGA-DTG plot of a carbonated sample after 7 days of carbonation is depicted. Similarly, all samples underwent testing and analysis after both 3 days and 7 days of carbonation. The mass losses observed in the temperature range of 500°C-800°C can be ascribed to the decomposition of $CaCO_3$ phases [69]. The presence of multiple DTG peaks within this temperature range was a result of the decomposition of various polymorphs of $CaCO_3$ [77], [91], [129]. These findings were further corroborated by SEM and XRD results. The peak observed around 250°C was attributed to the decomposition of M-4 [182]. The thermogravimetric analysis results were analyzed to obtain the total $CaCO_3$ contents (%) (**Figure 5.2(b) and (c)**).

It was observed that as the molecular weight increased, the $CaCO_3$ content also increased for all dosages. The overall formation of carbonate was greater at 7 days compared to 3 days, which is in line with expectations due to the extended reaction time. The theoretical maximum $CaCO_3$ formation in this system is around 61%. Among the molecular weight groups, the batch with MW 240000 exhibited the highest total carbonate formation (56%) within the system. Additionally, in the lower molecular weight group, the 1% dosage resulted in the highest $CaCO_3$ formation. In the MW 240000 group, the 2.5% dosage led to the highest $CaCO_3$ formation. As molecular weight increases, so does the chain length. The negatively charged M-4 can produce $CaCO_3$ with various crystal shapes, sizes, and polymorphs (such as vaterite, aragonite, ACC) [147]–[149].

	(a) 1 hr	(b) 3 hr	(c) 6 hr	(d) 24 hr
(1) Control				
(2) MW 2000				
(3) MW 5000				
(4) MW 240000				
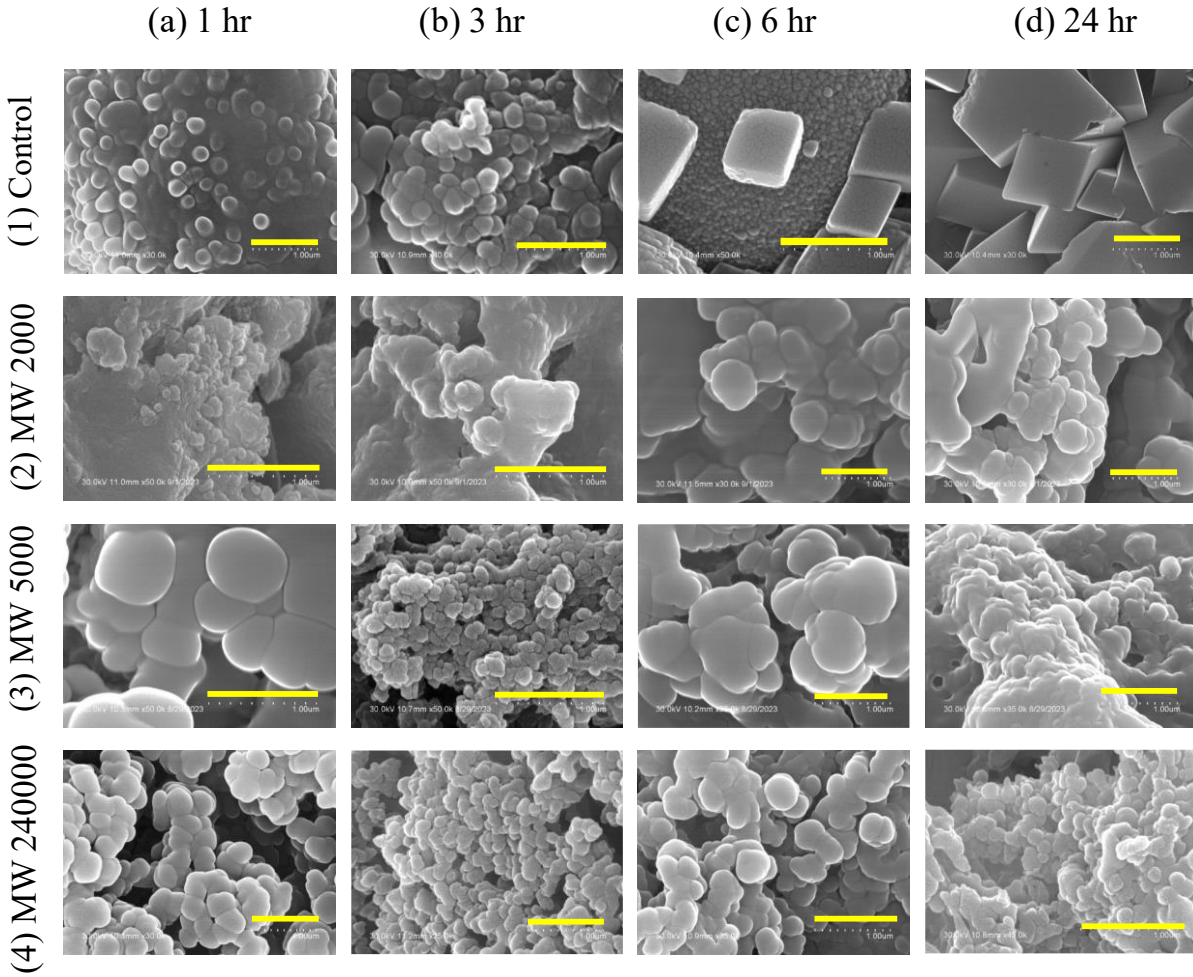
Figure 5.3: Evolution of the reaction products of Control samples, MW 2000, MW 5000, and MW 240000 over the first 24 hours. The scale bar represents 1 μm.

Figure 5.3 shows the evolution of the reaction products of different batches (1% dosage) in early age curing periods (1h, 3h, 6h and 24h). In the control sample, the amorphous calcium carbonates (ACC) formed within the first hour. The size of the ACC crystals was approximately 200 nm. After 3 hours, they became agglomerated, which eventually rearranged and formed calcite after 6 hours. The coexistence of ACC and calcites is evident from **Figure 5.3**(column b and c). After 24 hours, scattered precipitation of calcites is observed. The average size of the calcite crystals was around 600 nm after 6 hours, which increased up to 1.5 μm (approximately) after 24 hours. With

96

the addition of M-4 of MW 2000, no significant change in the reaction product morphology was observed up to the first 3 hours. Some ACC was observed after 6 hours of reaction with an average size of around 530 nm, which became agglomerated after 24 hours of reaction. In the MW 5000 sample, after one hour of exposure, well-formed metastable calcium carbonate phases with an average size of 570 nm were observed, which became agglomerated with time. A similar trend was observed in the MW 240000 sample. However, the agglomeration was prominent after the first hour of exposure in the latter specimens. After 3 hours, MW 5000 and MW 240000 batches formed larger and higher amounts of carbonate particles, indicating an accelerated carbonation reaction. It can be concluded that with the increase in the molecular weight, the glue effect became quite prominent, which bound the reaction products in the very early stages.
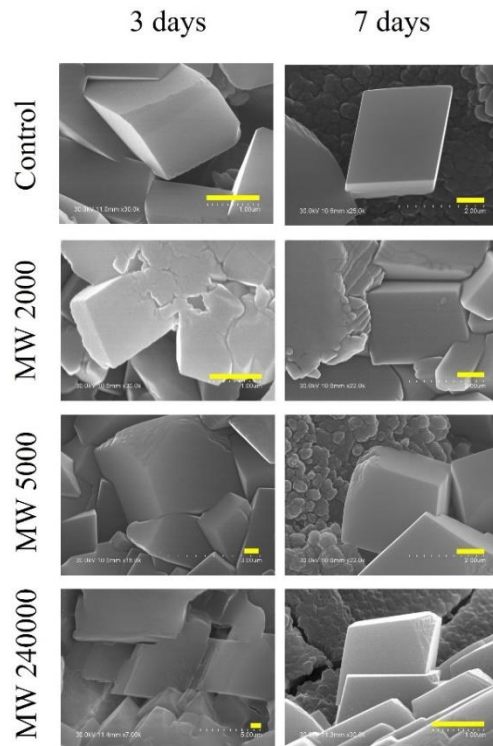
Figure 5.4: The morphology of the reaction products after 3 days and 7 days of reaction of different samples. The scale bar represents 1 μm.

After 3 days and 7 days of exposure, all the samples showed well-formed calcite crystals (**Figure 5.4**). These findings are in agreement with the findings from the thermogravimetric analyses. The calcite crystals of control samples and MW 2000 were similar, whereas the samples containing higher molecular weights (MW 5000 and MW 240000) showed well-formed calcites with a subtle boundary, which possibly resulted from the M-4 molecules.

5.3.2 Microstructural observations through in-situ FTIR, XRD and MIP

From **Figure 5.5,** the early age accelerated carbonation effects on the M-4 modified batches can be observed. 99% CO_2 purging environment visibly showed the carbonate precipitation over the time at 1400 cm^{-1} wavenumber. Further the 1400 cm^{-1} wavenumber peak values were normalized and plotted separately to understand the effect of molecular weight of M-4. Higher molecular weight batches showed faster carbonate precipitation compared to the control batch. MW 240000 batch exhibited the highest rate. However, there was no difference between MW 2000 and MW 5000 at the early age carbonation.
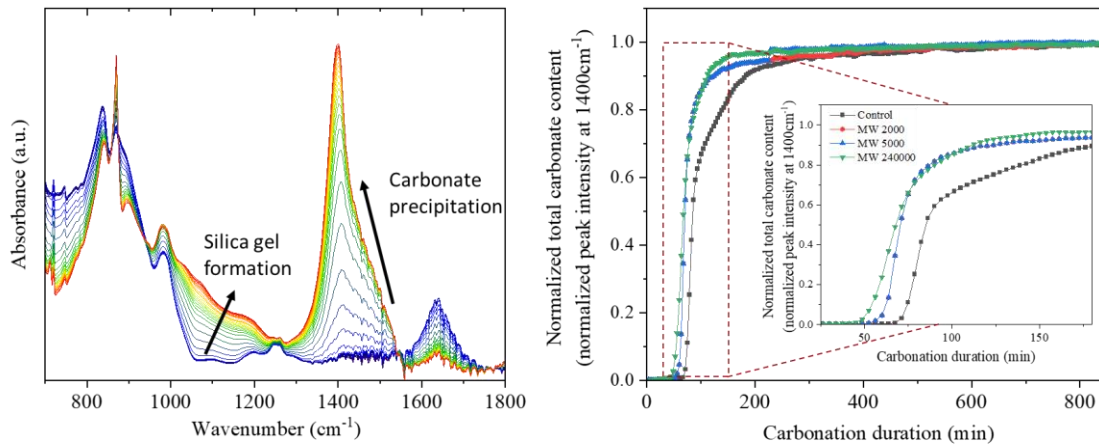
Figure 5.5: In-situ FTIR spectra of 99% CO₂ purged batches (1% dosage batches)

The X-ray diffraction results presented in Figure 6 provide valuable insights into the carbonation process, with **Figure 5.6**(a), (b), and (c) representing the 3-day carbonated batches, and **Figure 5.7**(a), (b), and (c) depicting the 7-day carbonated batches.

In the context of the 3-day carbonation batches, a notable observation was the increased intensity of the major calcite peak (around 29° 2θ) in the M-4-doped batches. Within the MW 2000 batch, both the 1% and 2.5% modifications exhibited the highest intensity of the calcite peak. Similarly, in the MW 5000 and MW 240000 batches, all modified batches (0.5%, 1%, and 2.5%) displayed enhanced calcite formation when compared to the control batch. It's important to note that in the MW 5000 and MW 240000 batches, vaterite formations were also observed alongside calcite.

Another intriguing observation was the reduction in the β-C_2S peak as the molecular weight increased. On the MW 240000 batches, both at 3 days and 7 days, the β-C_2S peak notably decreased (approximately 32° 2θ) with the simultaneous increase in calcite peak intensity. This suggests that higher molecular weights accelerated and enhanced calcite formation compared to other batches. This finding aligns well with the insights gained from the previously conducted thermogravimetric analysis.

These X-ray diffraction results provide crucial evidence of the influence of M-4 doping and molecular weight on the crystalline phases formed during carbonation, shedding light on the kinetics of calcite and vaterite formation while highlighting the relationship between molecular weight and phase transformation.
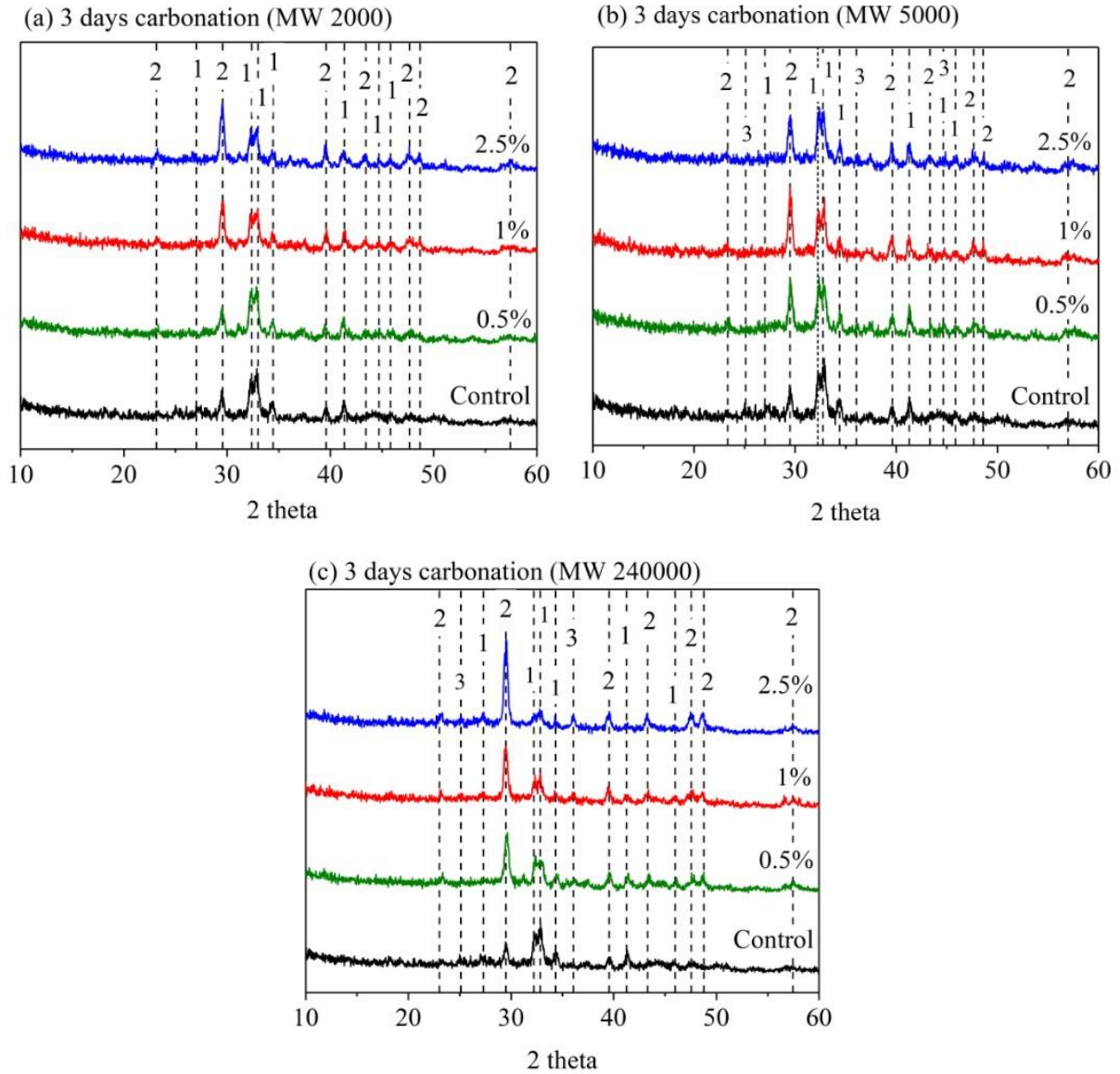
Figure 5.6: X-ray diffraction pattern of the β-C$_2$S paste samples at 3 days (different dosages)
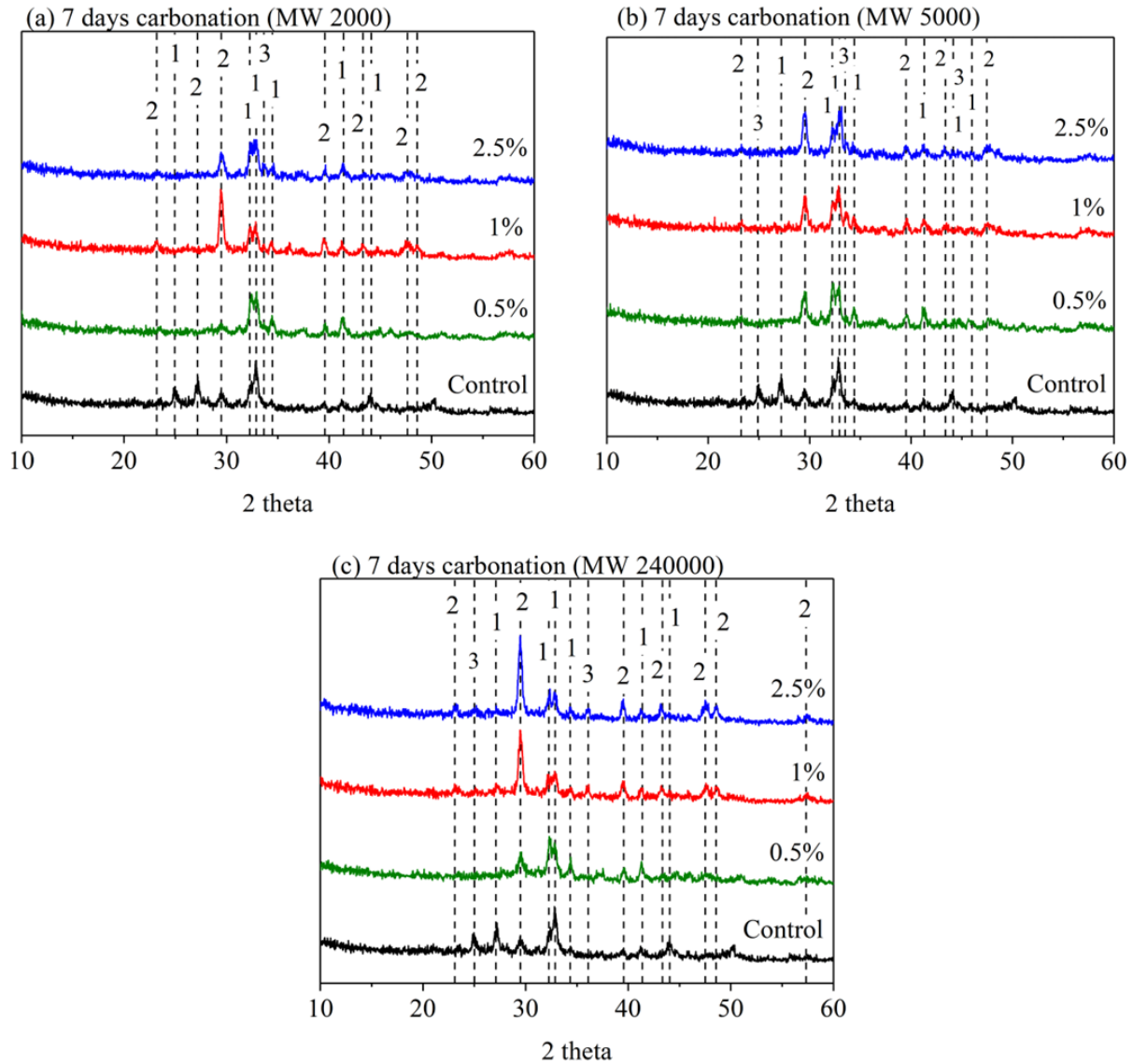
Figure 5.7: X-ray diffraction pattern of the β-C₂S paste samples at 7 days (different dosages)

Now, using the Scherrer equation, crystal size, $D = (K*\lambda)/(\beta*\cos\theta)$, where shape factor $K = 0.89$, $\lambda = 1.54$ Å, θ = Bragg's angle and β is the full width of the half maximum (FWHM) of the peak. Plugging the values, **Figure 5.8** have been obtained where average crystal size of different curing days were plotted. From Figure 5.7, it is clearly visible that, after 7 days of carbonation all the β-C₂S of MW 240000 batch have been reacted and formed $CaCO_3$. Therefore, it showed the maximum intensity of calcite formation at 29.6°. Since, the reaction product formation was also

maximized, hence, the formed crystal are supposed to be smaller. This observation matched well from the average crystal size calculation (**Figure 5.8**). From the average crystal size plots, it is found that, MW 240000 batch formed the crystals with smaller size.
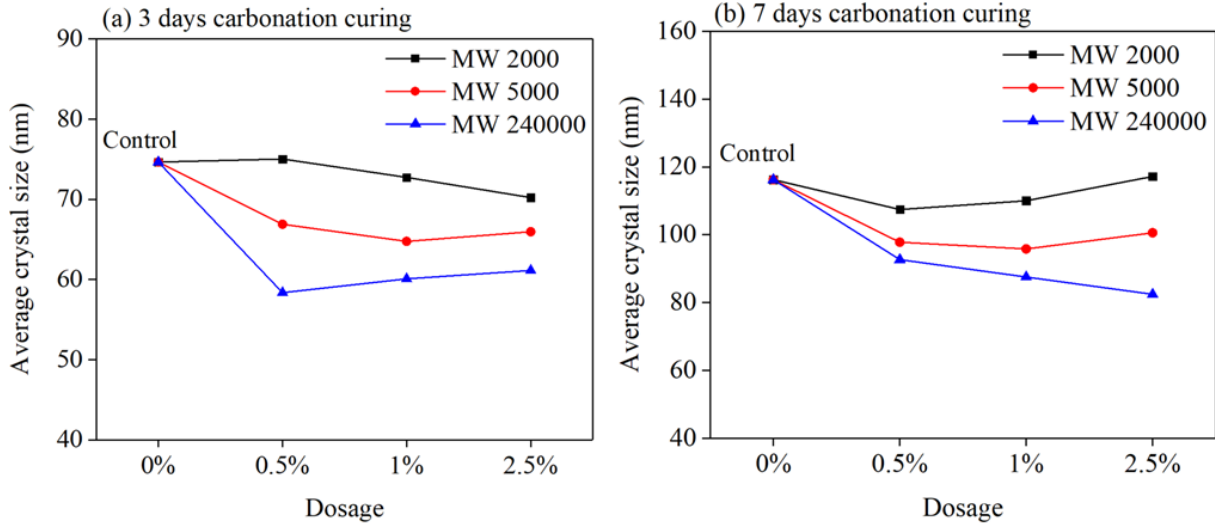
Figure 5.8: Average crystal size from XRD using Scherrer equation
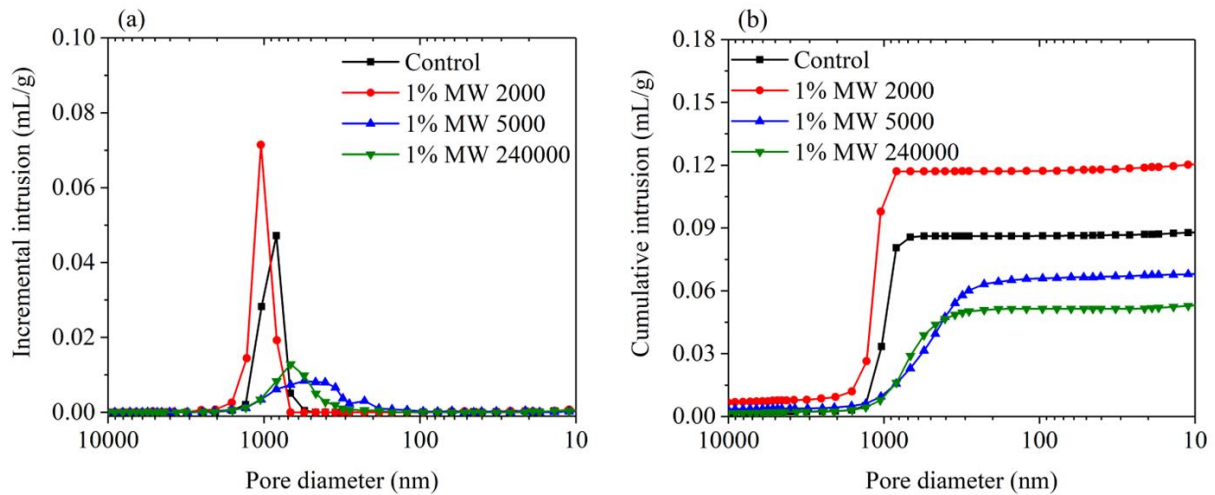
Figure 5.9: Effects of biomimetic molecules on pore size distribution of 7 days carbonated β-C$_2$S paste samples of 1% dosage batch.

The initial findings, where the 1% dosage batch displayed the most favorable performance by forming calcite after 7 days, prompted further exploration into the effects of porosity (**Figure 5.9(a) and (b)**). In comparison to the control batch, it was observed that the 1% dosage of MW 2000 exhibited an increased critical pore diameter, leading to a higher overall porosity. Due to the shorter chain length of MW 2000, the network of M-4 was not well distributed throughout the system, therefore, it could not make the matrix denser by forming higher amount of $CaCO_3$. In contrast, both the 1% dosage of MW 5000 and MW 240000 batches demonstrated a reduction in the critical diameter, resulting in a decreased total porosity. This decline in porosity can be attributed to the higher degree of carbonation, as indicated by the TGA analysis. The reduction in total porosity amounted to approximately 27% and 44% for the MW 5000 and MW 240000 batches, respectively. These findings were further substantiated by the pore size distribution data obtained from MIP, which aligns with the observations from the TGA analysis. The denser microstructure resulting from these changes is anticipated to lead to improved strength performance.

5.3.3 Macroscale performance evaluation (compressive and flexural strength)

We assessed the strength properties through two different approaches. The first involved curing at 27°C, while the second entailed testing after subjecting the samples to elevated temperatures at 50°C. For both testing conditions, we maintained consistent carbonation durations of 3 days and 7 days (20% CO_2 and 80% RH).
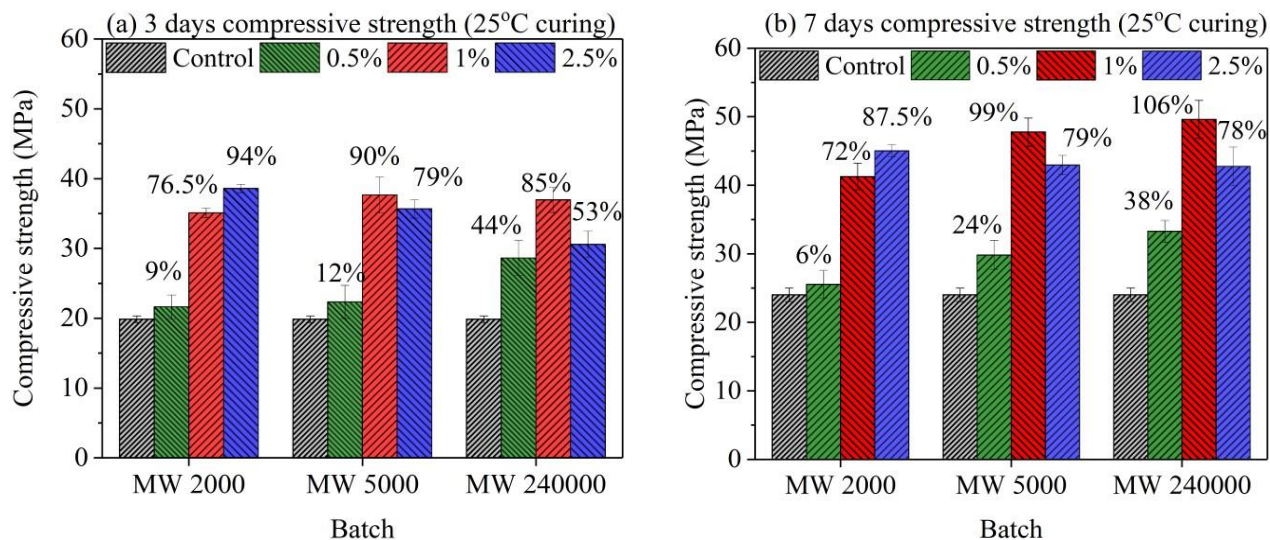
Figure 5.10: Compressive strength properties after (a) 3 days and (b) 7 days carbonation period (25°C cured batches)

In **Figure 5.10(a) and (b),** we observe the compressive strength results following 3 days and 7 days of carbonation for batches cured at ambient temperature. Consistent with our expectations based on the insights gained from TGA and MIP analyses, we witnessed improvements in compressive strength properties within the M-4-doped batches.

In the case of low dosage batches with low molecular weight, we noted a slight enhancement in strength, with the most substantial improvement reaching up to 24% in the 0.5% dosage of the MW 5000 batch. As the dosage and molecular weight increased, the performance exhibited a significant boost. This enhancement can be attributed to the reduction in porosity and the densification of the microstructure within the samples.

Notably, among the various batches, the 1% dosage batch demonstrated the most significant improvement following the addition of biomimetic molecules. Furthermore, with an increase in the molecular weight in the 1% dosage batches, the strength further improved. Specifically, after

7 days of carbonation, we observed increases of 72%, 99%, and 106% in the MW 2000, MW 5000, and MW 240000 batches, respectively.

These findings underscore the remarkable impact of M-4 doping, dosage levels, and molecular weight on the compressive strength of the specimens. The reductions in porosity and the enhancement of microstructural density contribute to the substantial improvements in strength, as evidenced by the substantial percentage increases observed across different molecular weight variations.
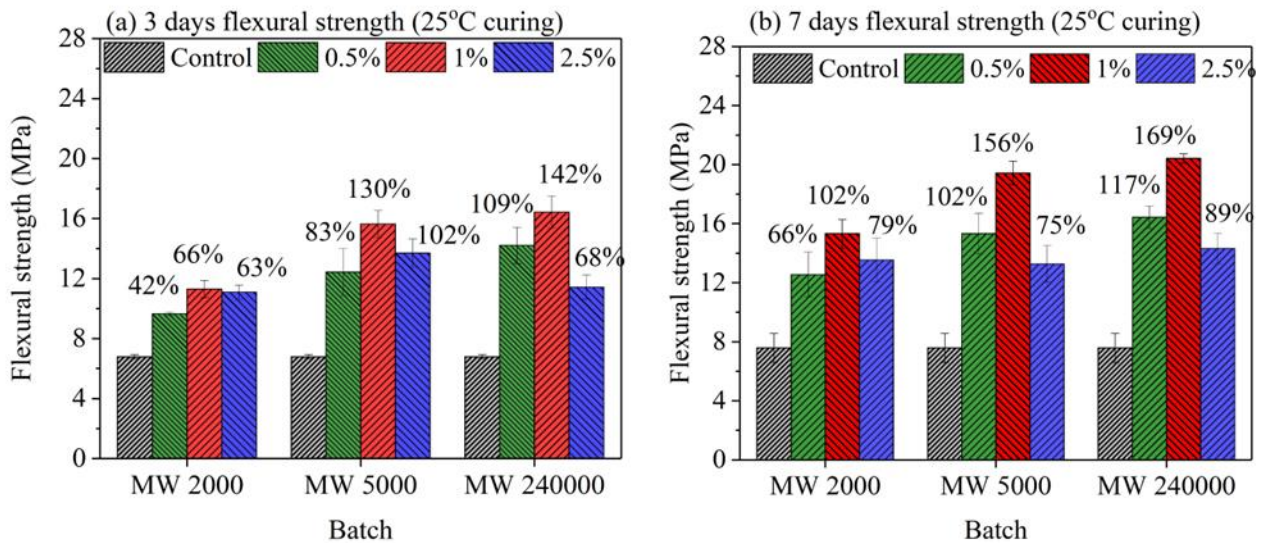
Figure 5.11: Flexural strength properties after (a) 3 days and (b) 7 days carbonation period (25°C cured batches)

Figure 5.11(a) and (b) depict the flexural strength properties of the samples cured at room temperature. Mirroring the trends observed in compression strength properties, improvements in flexural strength properties were also evident. Specifically, an increase in the dosage from 0.5% to 1% resulted in a significant enhancement in performance. However, a 2.5% dosage did not yield better results than the 1% batch, indicating that 1% dosage was optimal for flexural strength.

Both at the 3-day and 7-day marks, the 1% batch consistently showcased superior performance in the context of carbonated calcium silicate samples. The 1% dosage of MW 5000 exhibited a remarkable 130% improvement after 3 days and an even more impressive 156% increase after 7 days. Similarly, the 1% dosage of MW 240000 displayed a notable 142% increment after 3 days, which further escalated to a substantial 169% improvement after 7 days.

It is important to highlight that the higher molecular weight of the M-4 batches corresponds to longer chain lengths. This increased chain length contributed to an enhancement in tensile properties, which, in turn, translated into improved flexural properties. Therefore, the superior flexural properties observed can be attributed to the influence of M-4 molecular weight on the molecular structure and, subsequently, on the mechanical properties.

Given the notable performance of the 1% dosage batch in terms of both compressive and flexural strength properties, we conducted additional investigations with this dosage to explore the impact of temperature curing on the M-4-modified β-C_2S system.
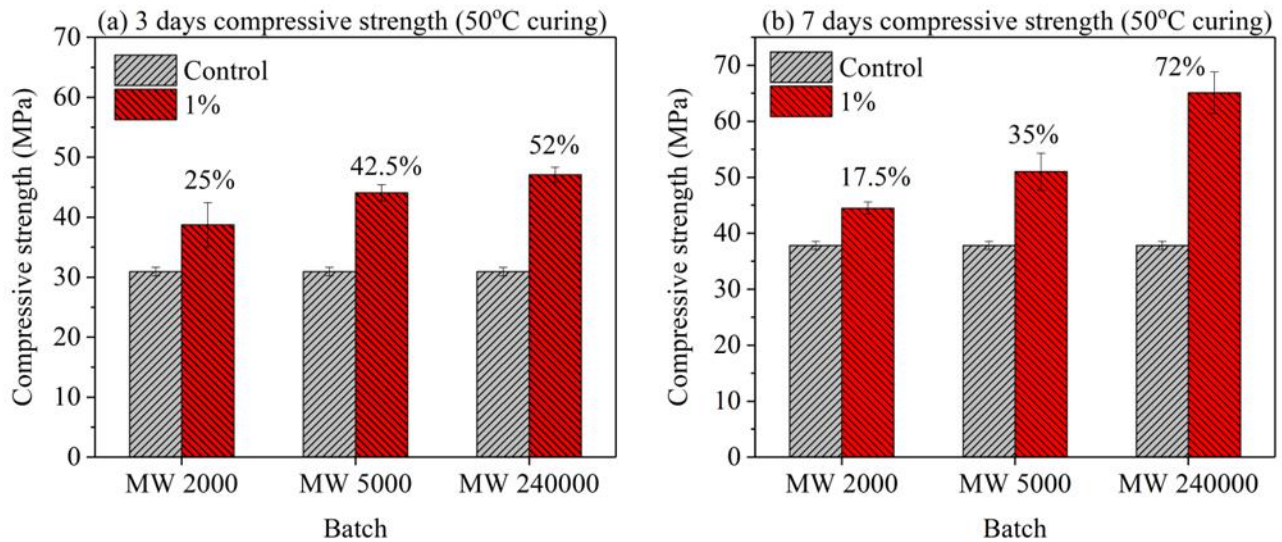
Figure 5.12: Compressive strength properties of 1% dosage - 50°C cured batches (a) 3 days (b) 7 days carbonation duration

In **Figure 5.12(a) and (b)**, we present the compressive strength results for samples subjected to elevated temperature (50°C) curing. Notably, the control batch exhibited a significant improvement of 50% and 40% after 3 days and 7 days of curing, respectively, in comparison to the 25°C temperature cured batches. Similarly, the 1% M-4-modified batches displayed improved performance. After 7 days of temperature curing, we observed compressive strength improvements of 17.5%, 35%, and 72% for the MW 2000, MW 5000, and MW 240000 batches, respectively. It's important to highlight that, while improvements were evident, the percent increase in compressive strength properties was not markedly higher than that of the non-temperature cured batches.

In **Figure 5.13(a) and (b)**, we turn our attention to the flexural strength properties of samples subjected to 3 days and 7 days of temperature (50°C) curing. Like the elevated temperature cured batches for M-4-doped compressive strength samples, the flexural strength improved. However, these improvements were not significantly higher than those observed in the ambient temperature cured batches. The most notable enhancement in flexural strength, reaching 114%, was observed in the 1% MW 240000 batch after 7 days of curing, in contrast to the previous case where a 169% improvement was recorded.
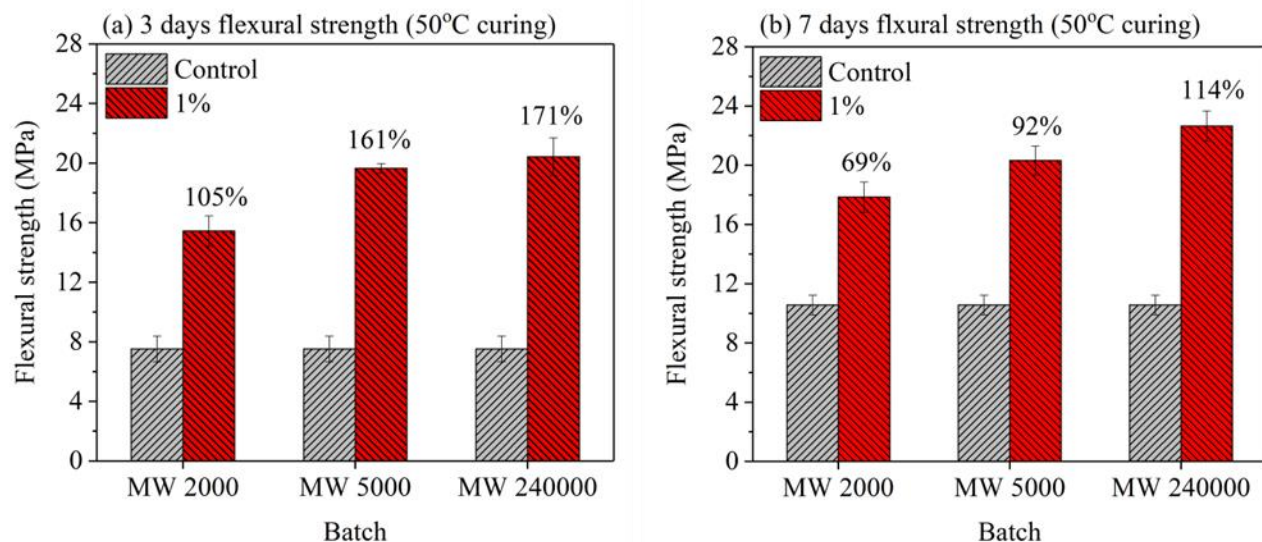
Figure 5.13: Flexural strength properties of 1% dosage - 50°C cured batches (a) 3 days (b) 7 days carbonation duration

In summary, it is evident that elevated temperature had a positive impact on the strength performance of M-4-modified β-C$_2$S. Nevertheless, it's crucial to note that even without the application of elevated temperature, the addition of the biomimetic molecule M-4 yielded significant and impressive strength properties under the conditions of 25°C temperature curing.

5.4 Discussions

The experimental analyses conducted in this study demonstrate the remarkable performance of M-4 with different molecular weights (MW 2000, MW 5000, and MW 240000) and varying dosages (0.5%, 1%, and 2.5%) when added to a β-C$_2$S binder. These effects can be attributed to several key mechanisms:

One of the fundamental mechanisms underlying the superior performance of M-4-modified β-C$_2$S binders is the molecular weight of M-4. As the molecular weight of M-4 increases, so does the chain length of the polymer. This phenomenon has a profound impact on the interaction between

M-4 and the calcium silicate matrix. The longer chains in higher molecular weight M-4 molecules enable stronger binding and bridging between the components of the matrix, resulting in increased cohesion and reduced porosity. Additionally, the longer M-4 chains provide a stronger glue effect with a greater number of surface sites for calcium ions in the system, facilitating the nucleation and growth of calcium carbonate phases. This phenomenon leads to enhanced crystal formation, as observed in the increased $CaCO_3$ content and the formation of well-defined calcite crystals in higher molecular weight M-4 batches.

The dosage of M-4 also plays a pivotal role in influencing the performance of the β-C_2S binder. Our findings consistently point to the 1% dosage as the optimum level, both in terms of $CaCO_3$ content and the formation of crystalline phases. At this dosage, the M-4 molecules are present in sufficient quantities to initiate and regulate the formation of $CaCO_3$ phases, while not overwhelming the system to the extent of excess porosity. Since, the MW 240000 provided the largest network of polymer due to glue effect, there were higher surface sites where the $CaCO_3$ could deposit. Therefore, MW 240000 could achieve almost theoretical maximum percent $CaCO_3$ formation. This observation also matched with the XRD findings where it was clearly prominent that, after 7 days carbonation, almost all the β-C_2S got reacted, hence the lesser size of crystals were formed.

The reduction in porosity and the densification of the microstructure are key factors contributing to the improved strength properties observed in M-4-modified samples. As M-4 interacts with the calcium silicate matrix, it effectively "glues" the components together, resulting in a more compact microstructure. This denser microstructure minimizes voids and pores, reducing pathways for crack propagation, and ultimately enhancing the mechanical properties of the material (**Figure 5.14**).
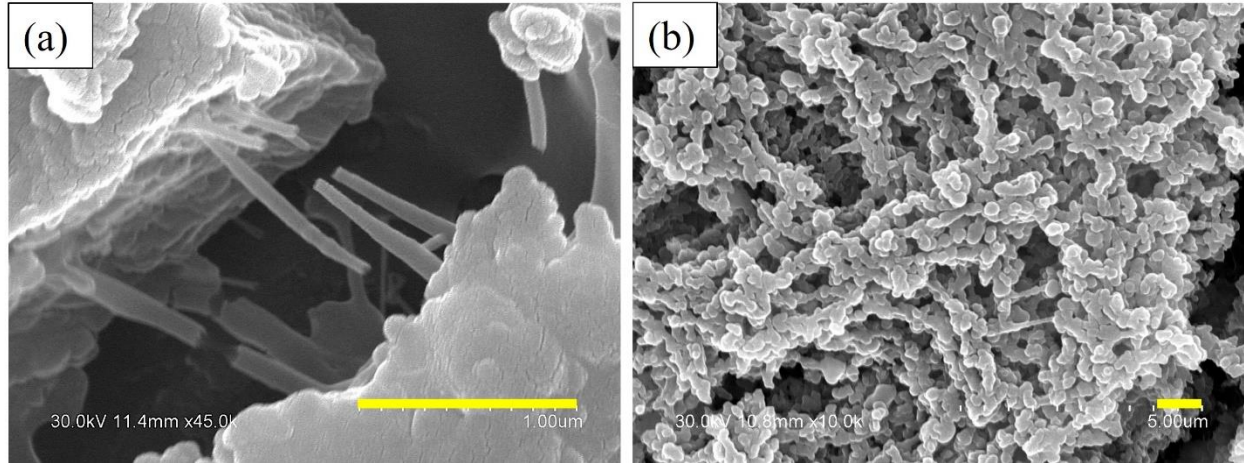
Figure 5.14: SEM images of (a) MW 5000 with the fibers of molecules, (b) MW 240000 where the molecule formed network base. The scale bar represents 1 μm.

From **Figure 5.14**(b), it can be seen that the molecules with the maximum molecular weight (MW 240000) along with the calcium carbonate polymorphs, formed a network. These networks acted as nucleation sites for further calcium carbonate precipitation. In the long run, it helped increase the compressive strength. In the MW 5000 specimens, the molecules formed fibers, but those were not viscous enough to support the calcium carbonate deposition. The discontinued fibers are shown in **Figure 5.14**(a). As a result, the glue effect was not as prominent as MW 240000 samples for MW 5000. On the other hand, the MW 2000 sample did not show such effects. These observations are in line with the compressive strength.

The influence of temperature curing on the performance of M-4-modified β-C$_2$S binders is twofold. Elevated temperature at 50°C curing accelerates the reactions between M-4 and the matrix, promoting stronger bonding and more efficient nucleation of calcium carbonate phases. However, even at 25°C temperature curing, the effects of M-4 are significant, as observed in the impressive strength properties achieved under these conditions. This suggests that the mechanisms at play extend beyond temperature dependence.

M-4 has a pronounced effect on the formation of carbonate polymorphs in the system. The ability of M-4 to regulate the formation of these carbonate phases indicates its role as a crystal growth modifier, influencing the shape, size, and polymorphism of calcium carbonate crystals.

In summary, the outstanding performance of M-4 in modifying the carbonation reaction of β-C_2S binders can be attributed to its molecular weight, dosage, and their interplay with the material's porosity and microstructure. M-4 acts as a bridge between components, enhances nucleation and growth of calcium carbonate phases, and influences the formation of distinct carbonate polymorphs. These mechanisms collectively contribute to the remarkable improvements in the mechanical properties of the material, making M-4 a promising additive for a wide range of applications in construction and materials science.

5.5 Conclusions

This study has yielded significant insights into the performance of M-4 with varying molecular weights (MW 2000, MW 5000, and MW 240000) and dosages (0.5%, 1%, and 2.5%) as a modifier in β-C_2S binders for carbonation. Several key findings can be summarized:

(i) The molecular weight of M-4 significantly influences the formation of calcium carbonate ($CaCO_3$) phases. Higher molecular weights lead to increased $CaCO_3$ content, with MW 240000 demonstrating the highest total carbonate formation which was almost as the theoretical maximum of percent calcium carbonate formation in the system.

(ii) Early-stage carbonation reaction was analyzed, and the results suggest that higher molecular weight M-4 enhances the formation of metastable calcium carbonate phases based on the SEM observations. The early stages of reaction products demonstrated the "glue effect" of M-4, resulting

111

in enhanced formation of calcium carbonate within the first hour. In-situ FTIR observation also aligned with this findings which showed MW 240000 formed faster $CaCO_3$ precipitation.

(iii) M-4-modified β-C_2S binders exhibit a reduced porosity and denser microstructure, with the 1% dosage of MW 5000 and MW 240000 batches demonstrating the most substantial reductions in porosity, contributing to improved strength properties. Added that, average crystal size analysis exhibited that higher molecular weight batches formed crystals with lesser size.

(iv) Both compressive and flexural strength properties of M-4-modified samples were examined. The 1% dosage of M-4, particularly with higher molecular weights, displayed remarkable improvements in strength, with increases reaching up to 106% for compressive strength and 169% for flexural strength after 7 days of carbonation at 25°C. When cured at 50°C, the compressive strength was observed to be improved by 72% and the flexural strength got increased by 114% for 1% dosage batches of MW 240000. These enhancements are attributed to reduced porosity and denser microstructure.

(v) The addition of M4 molecules also significantly enhanced the mechanical performance of the β-C_2S composites cured at 50C, indicating such additives can be used for both room temperature and high temperature curing conditions. However, the % increase in strength due to the addition of molecules was higher for room temperature curing considering β-C_2S show poor reactivity at room temperature.

In conclusion, this study highlights the remarkable performance of M-4 as a modifier in β-C_2S binders, with the molecular weight of M-4, dosage, and carbonation duration playing pivotal roles in enhancing calcium carbonate formation and improving mechanical strength.

6.1 Concluding remarks

The culmination of this dissertation provides valuable insights into the use of biomimetic molecules with varying dosages and molecular weights to enhance the properties of various cementitious phases, including calcium silicate hydrates (C-S-H) and beta-dicalcium silicates (β-C_2S) and gamma-dicalcium silicates (γ-C_2S). The conclusions drawn from each chapter are synthesized as follows:

Chapter 2 revealed the remarkable impact of biomimetic molecules (M-1 and M-2) on C-S-H. The modified C-S-H maintained its structure, exhibited significantly higher elastic moduli, and formed organic-inorganic nanohybrid phases, resulting in increased modulus after carbonation. These modifications also reduced the CO_2 sequestration capacity of C-S-H. The findings suggest that M-1 and M-2 can effectively enhance the durability of C-S-H by retaining its structure and improving mechanical properties after carbonation.

In Chapter 3, in-situ FTIR experiments offered a novel approach to monitor carbonation effects on calcium silicate hydrates. It was observed that pH and Ca/Si ratios influence C-S-H degradation, with higher pH environments promoting faster degradation. The addition of M-1 biomimetic molecules mitigated C-S-H degradation, emphasizing their potential to enhance resistance to carbonation-induced damage.

Chapter 4 delved into the impact of biomimetic molecules (M-1, M-3, and M-4) on γ-dicalcium silicate (γ-C_2S) cementitious systems. The modifications affected $CaCO_3$ polymorph formation, with M-4 exhibiting higher $CaCO_3$ content. While porosity measurements increased, the modified batches demonstrated significantly enhanced compressive and flexural strengths. Nanoindentation

results supported these improvements in strength, signifying the formation of organic-inorganic hybrid phases.

Chapter 5 centered on the performance of M-4 with different molecular weights and dosages as a modifier in β-C$_2$S binders. This study uncovered critical insights into the influence of molecular weight and dosage on calcium carbonate (CaCO$_3$) formation, crystal polymorphs, and microstructure. The "glue effect" of M-4 contributed to reduced porosity and denser microstructures, resulting in remarkable enhancements in compressive and flexural strengths, even without elevated temperature curing.

In summary, this dissertation highlights the promising potential of biomimetic molecules, particularly M-1, M-2, M-3 and M-4, in improving the durability and mechanical properties of cementitious phases which eventually make the conventional cementitious system or the promising low calcium silicate cement system more durable and sustainable. These findings are of significant relevance to the construction and materials science fields, offering opportunities to enhance strength and control over carbonate polymorphs. The dissertation underscores the importance of biomimetic molecules as versatile additives for optimizing construction materials and provides a foundation for further research and applications in the field.

6.2 Future recommendations

From the limitations and observations from this study, the future recommendations are as follows:

(a) Exploring the optimization of biomimetic molecules by incorporating composite dosage to enhance the carbonation properties of the cementitious phases.

(b) Exploring more promising biomimetic molecules that can play a similar or more potential role for performance enhancement of the cementitious system.

(c) Exploring the combined effects of temperature, carbonation concentration and relative humidity to observe the performance modification by the biomimetic molecules.

(d) Investigating the effects of these biomimetic molecules on macro-scale cementitious specimens to monitor the large-scale structural performance modifications.

(e) Finding the cost-optimized composite dosage of the biomimetic molecules for commercialization purpose by upscaling the production.

References

[1] S. Huey, T. Wiedmann, A. Castel, and J. De Burgh, "Hybrid life cycle assessment of greenhouse gas emissions from cement , concrete and geopolymer concrete in Australia," *J Clean Prod*, vol. 152, pp. 312–320, 2017, doi: 10.1016/j.jclepro.2017.03.122.

[2] C. Ouellet-Plamondon and G. Habert, "Life cycle assessment (LCA) of alkali-activated cements and concretes," in *Handbook of Alkali-activated Cements, Mortars and Concretes*, F. Pacheco-Torgal, J. A. Labrincha, C. Leonelli, A. Palomo, and P. Chindaprasirt, Eds., Woodhead Publishing Limited, 2020, pp. 663–686. doi: 10.1533/9781782422884.5.663.

[3] T. Bakharev, J. G. Sanjayan, and Y. B. Cheng, "Resistance of alkali-activated slag concrete to carbonation," *Cem Concr Res*, vol. 31, pp. 1277–1283, 2001, doi: 10.1016/S0008-8846(03)00125-X.

[4] F. Puertas, M. Palacios, and T. Vázquez, "Carbonation process of alkali-activated slag mortars," *J Mater Sci*, vol. 41, no. 10, pp. 3071–3082, 2006, doi: 10.1007/s10853-005-1821-2.

[5] E. Gruyaert, P. Van den Heede, and N. De Belie, "Carbonation of slag concrete: Effect of the cement replacement level and curing on the carbonation coefficient – Effect of carbonation on the pore structure," *Cem Concr Compos*, vol. 35, no. 1, pp. 39–48, Jan. 2013, doi: 10.1016/j.cemconcomp.2012.08.024.

[6] A. Younsi, P. Turcry, A. Aït-Mokhtar, and S. Staquet, "Accelerated carbonation of concrete with high content of mineral additions: Effect of interactions between hydration and drying," *Cem Concr Res*, vol. 43, no. 1, pp. 25–33, 2013, doi: 10.1016/j.cemconres.2012.10.008.

[7] B. Wu and G. Ye, "Development of porosity of cement paste blended with supplementary cementitious materials after carbonation," vol. 145, pp. 52–61, 2017, doi: 10.1016/j.conbuildmat.2017.03.176.

[8] M. Palacios and F. Puertas, "Effect of carbonation on alkali-activated slag paste," *Journal of the American Ceramic Society*, vol. 89, no. 10, pp. 3211–3221, 2006, doi: 10.1111/j.1551-2916.2006.01214.x.

[9] Z. Li and S. Li, "Carbonation resistance of fly ash and blast furnace slag based geopolymer concrete," *Constr Build Mater*, vol. 163, pp. 668–680, 2018, doi: 10.1016/j.conbuildmat.2017.12.127.

[10] V. G. Papadakis, M. N. Fardis, and C. G. Vayenas, "Hydration and carbonation of pozzolanic cements," *ACI Mater J*, vol. 89, no. 2, 1992, doi: 10.14359/2185.

[11] M. Á. Sanjuán, E. Estévez, C. Argiz, and D. del Barrio, "Effect of curing time on granulated blast-furnace slag cement mortars carbonation," *Cem Concr Compos*, vol. 90, no. September 2017, pp. 257–265, 2018, doi: 10.1016/j.cemconcomp.2018.04.006.

[12] M. Sufian Badar, K. Kupwade-Patil, S. a. Bernal, J. L. Provis, and E. N. Allouche, "Corrosion of steel bars induced by accelerated carbonation in low and high calcium fly ash geopolymer concretes," *Constr Build Mater*, vol. 61, pp. 79–89, 2014, doi: 10.1016/j.conbuildmat.2014.03.015.

[13]   V. Shah, K. Scrivener, B. Bhattacharjee, and S. Bishnoi, "Changes in microstructure characteristics of cement paste on carbonation," *Cem Concr Res*, vol. 109, no. April, pp. 184–197, 2018, doi: 10.1016/j.cemconres.2018.04.016.

[14]   S. A. Bernal, *The resistance of alkali-activated cement-based binders to carbonation*. Woodhead Publishing Limited, 2015. doi: 10.1533/9781782422884.3.319.

[15]   J. J. Chen, J. J. Thomas, and H. M. Jennings, "Decalcification shrinkage of cement paste," vol. 36, pp. 801–809, 2006, doi: 10.1016/j.cemconres.2005.11.003.

[16]   T. C. Powers, "A hypothesis on carbonation shrinkage," *Journal of Portland Cement Association. Research and Development Laboratories*, vol. 4, no. 2, pp. 40–50, 1962.

[17]   R. Liu, L. Jiang, J. Xu, C. Xiong, and Z. Song, "Influence of carbonation on chloride-induced reinforcement corrosion in simulated concrete pore solutions," *Constr Build Mater*, vol. 56, pp. 16–20, 2014, doi: 10.1016/j.conbuildmat.2014.01.030.

[18]   B. Huet, V. L'Hostis, F. Miserque, and H. Idrissi, "Electrochemical behavior of mild steel in concrete: Influence of pH and carbonate content of concrete pore solution," *Electrochim Acta*, vol. 51, no. 1, pp. 172–180, 2005, doi: 10.1016/j.electacta.2005.04.014.

[19]   J. C. Walton, S. Bin-Shafique, R. W. Smith, N. Gutierrez, and A. Tarquin, "Role of carbonation in transient leaching of cementitious wasteforms," *Environ Sci Technol*, vol. 31, no. 8, pp. 2345–2349, 1997, doi: 10.1021/es960964j.

[20]   V. T. Ngala and C. L. Page, "Effects of Carbonation on Pore Structure and Diffusional Properties of Hydrated Cement Pastes," *Cem Concr Res*, vol. 27, no. 7, pp. 995–1007, 1997, doi: 10.1016/S0008-8846(97)00102-6.

[21]   P. S. E., "Some results of the effect of carbonation on the porosity and pore size distribution of cement paste," *Materials and Construction*, pp. 521–526, 1968.

[22]   M. Morone, G. Costa, A. Polettini, R. Pomi, and R. Baciocchi, "Valorization of steel slag by a combined carbonation and granulation treatment," *Miner Eng*, vol. 59, 2014, doi: 10.1016/j.mineng.2013.08.009.

[23]   V. Rostami, Y. Shao, and A. J. Boyd, "Carbonation Curing versus Steam Curing for Precast Concrete Production," *Journal of Materials in Civil Engineering*, vol. 24, no. 9, 2012, doi: 10.1061/(asce)mt.1943-5533.0000462.

[24]   Z. He, Y. Jia, S. Wang, M. Mahoutian, and Y. Shao, "Maximizing CO2 sequestration in cement-bonded fiberboards through carbonation curing," *Constr Build Mater*, vol. 213, 2019, doi: 10.1016/j.conbuildmat.2019.04.042.

[25]   B. Lu, C. Shi, Z. Cao, M. Guo, and J. Zheng, "Effect of carbonated coarse recycled concrete aggregate on the properties and microstructure of recycled concrete," *J Clean Prod*, vol. 233, 2019, doi: 10.1016/j.jclepro.2019.05.350.

[26]   P. Ren, T. C. Ling, and K. H. Mo, "Recent advances in artificial aggregate production," *Journal of Cleaner Production*, vol. 291. 2021. doi: 10.1016/j.jclepro.2020.125215.

[27]   S. Deng, P. Ren, Y. Jiang, X. Shao, and T. C. Ling, "Use of CO2-active BOFS binder in the production of artificial aggregates with waste concrete powder," *Resour Conserv Recycl*, vol. 182, 2022, doi: 10.1016/j.resconrec.2022.106332.

[28]   N. Lippiatt, T. C. Ling, and S. Y. Pan, "Towards carbon-neutral construction materials: Carbonation of cement-based materials and the future perspective," *Journal of Building Engineering*, vol. 28. 2020. doi: 10.1016/j.jobe.2019.101062.

[29]   C. M. Woodall, N. McQueen, H. Pilorgé, and J. Wilcox, "Utilization of mineral carbonation products: current state and potential," *Greenhouse Gases: Science and Technology*, vol. 9, no. 6. 2019. doi: 10.1002/ghg.1940.

[30]   J. G. Jang and H. K. Lee, "Microstructural densification and CO2 uptake promoted by the carbonation curing of belite-rich Portland cement," *Cem Concr Res*, vol. 82, 2016, doi: 10.1016/j.cemconres.2016.01.001.

[31]   D. Xuan, B. Zhan, and C. S. Poon, "Assessment of mechanical properties of concrete incorporating carbonated recycled concrete aggregates," *Cem Concr Compos*, vol. 65, 2016, doi: 10.1016/j.cemconcomp.2015.10.018.

[32]   X. Fang, D. Xuan, and C. S. Poon, "Empirical modelling of CO2 uptake by recycled concrete aggregates under accelerated carbonation conditions," *Materials and Structures/Materiaux et Constructions*, vol. 50, no. 4, 2017, doi: 10.1617/s11527-017-1066-y.

[33]   M. Zhan, G. Pan, Y. Wang, M. Fu, and X. Lu, "Effect of presoak-accelerated carbonation factors on enhancing recycled aggregate mortars," *Magazine of Concrete Research*, vol. 69, no. 16, 2017, doi: 10.1680/jmacr.16.00468.

[34]   B. J. Zhan, D. X. Xuan, C. S. Poon, and C. J. Shi, "Effect of curing parameters on CO2 curing of concrete blocks containing recycled aggregates," *Cem Concr Compos*, vol. 71, 2016, doi: 10.1016/j.cemconcomp.2016.05.002.

[35]   J. Wang, J. Zhang, D. Cao, H. Dang, and B. Ding, "Comparison of recycled aggregate treatment methods on the performance for recycled concrete," *Constr Build Mater*, vol. 234, 2020, doi: 10.1016/j.conbuildmat.2019.117366.

[36]   S. C. Kou, B. J. Zhan, and C. S. Poon, "Use of a CO2 curing step to improve the properties of concrete prepared with recycled aggregates," *Cem Concr Compos*, vol. 45, 2014, doi: 10.1016/j.cemconcomp.2013.09.008.

[37]   V. W. Y. Tam, A. Butera, and K. N. Le, "An investigation of the shrinkage, concrete shrinkage reversibility and permeability of CO2-treated concrete," *Constr Build Mater*, vol. 365, 2023, doi: 10.1016/j.conbuildmat.2022.130120.

[38]   Y. Pu *et al.*, "Accelerated carbonation technology for enhanced treatment of recycled concrete aggregates: A state-of-the-art review," *Constr Build Mater*, vol. 282, 2021, doi: 10.1016/j.conbuildmat.2021.122671.

[39]   N. Li, L. Mo, and C. Unluer, "Emerging CO2utilization technologies for construction materials: A review," *Journal of CO2 Utilization*, vol. 65. 2022. doi: 10.1016/j.jcou.2022.102237.

[40] A. E. Morandeau and C. E. White, "Role of Magnesium-Stabilized Amorphous Calcium Carbonate in Mitigating the Extent of Carbonation in Alkali-Activated Slag," *Chemistry of Materials*, vol. 27, no. 19, pp. 6625–6634, 2015, doi: 10.1021/acs.chemmater.5b02382.

[41] S. Goto, K. Suenaga, and T. Kado, "Calcium silicate carbonation products," *Journal of the American Ceramic Society*, vol. 78, no. 11, pp. 2867–72, 1995.

[42] G. W. Groves, A. Brough, I. G. Richardson, and C. M. Dobson, "Progressive changes in the structure of hardened C3S cement pastes due to carbonation," *Journal of the American Ceramic Society*, vol. 74, pp. 2891–2896, 1991, doi: 10.1111/j.1151-2916.1991.tb06859.x.

[43] O. Shtepenko, C. Hills, A. Brough, and M. Thomas, "The effect of carbon dioxide on β-dicalcium silicate and Portland cement," *Chemical Engineering Journal*, vol. 118, no. 1–2, pp. 107–118, May 2006, doi: 10.1016/j.cej.2006.02.005.

[44] E. T. Stepkowska, M. A. Aviles, and J. M. Blanes, "GRADUAL TRANSFORMATION OF Ca (OH) 2 INTO CaCO 3 ON CEMENT HYDRATION XRD study," *Journal ofThermal Analysis and Calorimetry*, vol. 87, pp. 189–198, 2007.

[45] R. Ylmén and U. Jäglid, "Carbonation of Portland Cement Studied by Diffuse Reflection Fourier Transform Infrared Spectroscopy," *Int J Concr Struct Mater*, vol. 7, no. 2, pp. 119–125, May 2013, doi: 10.1007/s40069-013-0039-y.

[46] P. López-Arce, L. S. Gómez-Villalba, S. Martínez-Ramírez, M. Álvarez de Buergo, and R. Fort, "Influence of relative humidity on the carbonation of calcium hydroxide nanoparticles and the formation of calcium carbonate polymorphs," *Powder Technol*, vol. 205, no. 1–3, pp. 263–269, 2011, doi: 10.1016/j.powtec.2010.09.026.

[47] S. Goñi, M. T. Gaztañaga, and a. Guerrero, "Role of Cement Type on Carbonation Attack," *J Mater Res*, vol. 17, no. 07, pp. 1834–1842, 2002, doi: 10.1557/JMR.2002.0271.

[48] D. Gebauer, A. Völkel, and H. Cölfen, "Stable Prenucleation Calcium Carbonate Clusters," *Science (1979)*, vol. 322, no. 5909, pp. 1819–1822, 2008, doi: 10.1126/science.1164271.

[49] L. N. Plummer and E. Busenberg, "The solubilities of calcite, aragonite and vaterite in CO2," *Geochim Cosmochim Acta*, vol. 46, no. 6, pp. 1011–1040, 1982, doi: 10.1016/0016-7037(82)90056-4.

[50] D. Ren, Q. Feng, and X. Bourrat, "Effects of additives and templates on calcium carbonate mineralization in vitro," *Micron*, vol. 42, no. 3, pp. 228–245, 2011, doi: 10.1016/j.micron.2010.09.005.

[51] O. E. Meiron *et al.*, "Solubility and bioavailability of stabilized amorphous calcium carbonate," *Journal of Bone and Mineral Research*, vol. 26, no. 2, pp. 364–372, 2011, doi: 10.1002/jbmr.196.

[52] S. Y. Wang, E. McCaslin, and C. E. White, "Effects of magnesium content and carbonation on the multiscale pore structure of alkali-activated slags," *Cem Concr Res*, vol. 130, no. October 2019, p. 105979, 2020, doi: 10.1016/j.cemconres.2020.105979.

[53] N. A. J. M. Sommerdijk and G. De With, "Biomimetic CaCO 3 Mineralization using Designer Molecules and Interfaces," *Chem Rev*, vol. 108, no. 11, pp. 4499–4550, 2008.

[54] B. Polyamorphism, J. H. E. Cartwright, A. G. Checa, J. D. Gale, D. Gebauer, and C. I. Sainz-díaz, "Calcium Carbonate Polyamorphism and Its Role in Biomineralization : How Many Amorphous Calcium Carbonates Are There ? Angewandte," pp. 11960–11970, 2012, doi: 10.1002/anie.201203125.

[55] K. Maruyama, T. Yoshino, and H. Kagi, "Synthesizing a composite material of amorphous calcium carbonate and aspartic acid," *Mater Lett*, vol. 65, no. 2, pp. 179–181, 2011, doi: 10.1016/j.matlet.2010.09.039.

[56] Z. Zou, L. Bertinetti, Y. Politi, P. Fratzl, and W. J. E. M. Habraken, "Control of Polymorph Selection in Amorphous Calcium Carbonate Crystallization by Poly(Aspartic Acid): Two Different Mechanisms," *Small*, vol. 13, no. 21, pp. 1–11, 2017, doi: 10.1002/smll.201603100.

[57] P. Stempfle, O. Pantale, R. K. Njiwa, M. Rousseau, E. Lopez, and X. Bourrat, "Friction-induced sheet nacre fracture: effects of nano-shocks on cracks location," *Int J Nanotechnol*, vol. 4, no. 6, p. 712, 2015, doi: 10.1504/ijnt.2007.015466.

[58] R. I. Khan, W. Ashraf, and J. Olek, "Amino acids as performance-controlling additives in carbonation-activated cementitious materials," *Cem Concr Res*, vol. 147, 2021, doi: 10.1016/j.cemconres.2021.106501.

[59] S. Kim and C. B. Park, "Dopamine-Induced Mineralization of Calcium Carbonate Vaterite Microspheres," *Langmuir*, vol. 26, no. 21, pp. 14730–14736, 2010, doi: 10.1021/la1027509.

[60] S. S. Wang and A. W. Xu, "Amorphous calcium carbonate stabilized by a flexible biomimetic polymer inspired by marine mussels," *Cryst Growth Des*, vol. 13, no. 5, pp. 1937–1942, 2013, doi: 10.1021/cg301759t.

[61] Z. Li, B. Peng, and Z. Deng, "Biomimetic synthesis of calcium carbonate films on bioinspired polydopamine matrices," *J Coat Technol Res*, vol. 14, no. 5, pp. 1095–1105, 2017, doi: 10.1007/s11998-016-9898-x.

[62] Z. Liu *et al.*, "Effect of polydopamine on the biomimetic mineralization of mussel-inspired calcium phosphate cement in vitro," *Materials Science and Engineering C*, vol. 44, pp. 44–51, 2014, doi: 10.1016/j.msec.2014.07.063.

[63] Z. Liu *et al.*, "Effect of polydopamine on the biomimetic mineralization of mussel-inspired calcium phosphate cement in vitro," *Materials Science and Engineering C*, vol. 44, pp. 44–51, 2014, doi: 10.1016/j.msec.2014.07.063.

[64] Y. Fang, J. Wang, X. Qian, L. Wang, G. Lin, and Z. Liu, "Bio-inspired functionalization of very fine aggregates for better performance of cementitious materials," *Constr Build Mater*, vol. 241, p. 118104, 2020, doi: 10.1016/j.conbuildmat.2020.118104.

[65] W. Ashraf and J. Olek, "Carbonation activated binders from pure calcium silicates: Reaction kinetics and performance controlling factors," *Cem Concr Compos*, vol. 93, no. February, pp. 85–98, 2018, doi: 10.1016/j.cemconcomp.2018.07.004.

[66] W. Ashraf and J. Olek, "Carbonation behavior of hydraulic and non-hydraulic calcium silicates: potential of utilizing low-lime calcium silicates in cement-based materials," *J Mater Sci*, vol. 51, no. 13, pp. 6173–6191, 2016, doi: 10.1007/s10853-016-9909-4.

[67] J. M. Bukowski and R. L. Berger, "Reactivity and strength development of CO2 activated non-hydraulic calcium silicates," *Cem Concr Res*, vol. 9, no. 1, 1979, doi: 10.1016/0008-8846(79)90095-4.

[68] R. L. BERGER, J. F. YOUNG, and K. LEUNG, "Acceleration of Hydration of Calcium Silicates by Carbon Dioxide Treatment," *Nature Physical Science*, vol. 240, no. 97, 1972, doi: 10.1038/physci240016a0.

[69] W. Ashraf, "Microstructure of chemically activated of gamma-dicalcium silicate paste," *Constr Build Mater*, vol. 185, 2018, doi: 10.1016/j.conbuildmat.2018.07.030.

[70] C. Shi, B. Qu, and J. L. Provis, "Recent progress in low-carbon binders," *Cem Concr Res*, vol. 122, no. April, pp. 227–250, 2019, doi: 10.1016/j.cemconres.2019.05.009.

[71] M. C. G. Juenger, F. Winnefeld, J. L. Provis, and J. H. Ideker, "Advances in alternative cementitious binders," *Cem Concr Res*, vol. 41, no. 12, pp. 1232–1243, 2011, doi: 10.1016/j.cemconres.2010.11.012.

[72] S. A. Bernal *et al.*, "Gel nanostructure in alkali-activated binders based on slag and fly ash, and effects of accelerated carbonation," *Cem Concr Res*, vol. 53, 2013, doi: 10.1016/j.cemconres.2013.06.007.

[73] S. A. Bernal, J. L. Provis, D. G. Brice, A. Kilcullen, P. Duxson, and J. S. J. van Deventer, "Accelerated carbonation testing of alkali-activated binders significantly underestimates service life: The role of pore solution chemistry," *Cem Concr Res*, vol. 42, no. 10, 2012, doi: 10.1016/j.cemconres.2012.07.002.

[74] P. López-Arce, L. S. Gómez-Villalba, S. Martínez-Ramírez, M. Álvarez de Buergo, and R. Fort, "Influence of relative humidity on the carbonation of calcium hydroxide nanoparticles and the formation of calcium carbonate polymorphs," *Powder Technol*, vol. 205, no. 1–3, 2011, doi: 10.1016/j.powtec.2010.09.026.

[75] S. Goñi, M. T. Gaztañaga, and A. Guerrero, "Role of cement type on carbonation attack," *J Mater Res*, vol. 17, no. 7, 2002, doi: 10.1557/JMR.2002.0271.

[76] D. Gebauer, A. Völkel, and H. Cölfen, "Stable prenucleation calcium carbonate clusters," *Science (1979)*, vol. 322, no. 5909, 2008, doi: 10.1126/science.1164271.

[77] W. Ashraf and J. Olek, "Elucidating the accelerated carbonation products of calcium silicates using multi-technique approach," *Journal of CO2 Utilization*, vol. 23, 2018, doi: 10.1016/j.jcou.2017.11.003.

[78] A. E. Morandeau and C. E. White, "Role of Magnesium-Stabilized Amorphous Calcium Carbonate in Mitigating the Extent of Carbonation in Alkali-Activated Slag," *Chemistry of Materials*, vol. 27, no. 19, 2015, doi: 10.1021/acs.chemmater.5b02382.

[79] N. A. J. M. Sommerdijk and G. de With, "Biomimetic CaCO3 mineralization using designer molecules and interfaces," *Chem Rev*, vol. 108, no. 11, 2008, doi: 10.1021/cr078259o.

[80] L. Ma, J. Zhu, M. Cui, L. Huang, and Y. Su, "Biomimetic synthesis of novel calcium carbonate heterogeneous dendrites," *New Journal of Chemistry*, vol. 39, no. 7, pp. 5309–5315, 2015, doi: 10.1039/c5nj00219b.

[81]   K. Maruyama, T. Yoshino, and H. Kagi, "Synthesizing a composite material of amorphous calcium carbonate and aspartic acid," *Mater Lett*, vol. 65, no. 2, pp. 179–181, 2011, doi: 10.1016/j.matlet.2010.09.039.

[82]   Z. Zou, L. Bertinetti, Y. Politi, P. Fratzl, and W. J. E. M. Habraken, "Control of Polymorph Selection in Amorphous Calcium Carbonate Crystallization by Poly(Aspartic Acid): Two Different Mechanisms," *Small*, vol. 13, no. 21, pp. 1–11, 2017, doi: 10.1002/smll.201603100.

[83]   P. Wan, J. Hu, W. Ma, L. Wang, L. Cao, and H. Tong, "Control over the crystal phase, shape, size and aggregation of calcium carbonate via a l-aspartic acid inducing process," *Biomaterials*, vol. 25, no. 17, pp. 3923–3929, 2003, doi: 10.1016/j.biomaterials.2003.10.038.

[84]   L. Štajner *et al.*, "The effect of different amino acids on spontaneous precipitation of calcium carbonate polymorphs," *J Cryst Growth*, vol. 486, pp. 71–81, 2018, doi: 10.1016/j.jcrysgro.2018.01.023.

[85]   P. Stempflé, O. Pantalé, R. K. Njiwa, M. Rousseau, E. Lopez, and X. Bourrat, "Friction-induced sheet nacre fracture: Effects of nano-shocks on cracks location," *Int J Nanotechnol*, vol. 4, no. 6, pp. 712–729, 2007, doi: 10.1504/IJNT.2007.015466.

[86]   C. A. Orme *et al.*, "Formation of chiral morphologies through selective binding of amino acids to calcite surface steps," *Nature*, vol. 411, no. 6839, 2001, doi: 10.1038/35081034.

[87]   H. H. Teng, P. M. Dove, C. A. Orme, and J. J. de Yoreo, "Thermodynamics of calcite growth: Baseline for understanding biomineral formation," *Science (1979)*, vol. 282, no. 5389, 1998, doi: 10.1126/science.282.5389.724.

[88]   Y. Y. Kim *et al.*, "Tuning hardness in calcite by incorporation of amino acids," *Nat Mater*, vol. 15, no. 8, pp. 903–910, 2016, doi: 10.1038/nmat4631.

[89]   L. Qiao, Q. Feng, Z. Li, and S. Lu, "Alternate deposition of oriented calcite and amino acid layer on calcite substrates," *Journal of Physical Chemistry B*, vol. 112, no. 43, 2008, doi: 10.1021/jp8028775.

[90]   X. H. Guo, A. W. Xu, and S. H. Yu, "Crystallization of calcium carbonate mineral with hierarchical structures in DMF solution under control of poly(ethylene glycol)-b-poly(L-glutamic acid): Effects of crystallization temperature and polymer concentration," *Cryst Growth Des*, vol. 8, no. 4, 2008, doi: 10.1021/cg7008368.

[91]   R. I. Khan, W. Ashraf, and J. Olek, "Amino acids as performance-controlling additives in carbonation-activated cementitious materials," *Cem Concr Res*, vol. 147, no. May, 2021.

[92]   H. L. Kim, Y. S. Shin, and S. H. Yang, "Effect of poly(acrylic acid) on crystallization of calcium carbonate in a hydrogel," *CrystEngComm*, vol. 24, no. 7, 2022, doi: 10.1039/d1ce01687c.

[93]   H. Matsuyama and J. F. Young, "Synthesis of calcium silicate hydrate / polymer complexes : Part II . Cationic polymers and complex formation with different polymers," *Journal of Material Research*, vol. 14, no. 8, pp. 3389–3396, 1999.

[94]   H. Matsuyama and J. F. Young, "Synthesis of calcium silicate hydrate / polymer complexes : Part I. Anionic and nonionic polymers," *Journal of Material Research*, vol. 14, no. 8, pp. 3379–3388, 1999.

[95]   W. Ashraf, J. Olek, and N. Tian, "Multiscale characterization of carbonated wollastonite paste and application of homogenization schemes to predict its effective elastic modulus," *Cem Concr Compos*, vol. 72, pp. 284–298, 2016, doi: 10.1016/j.cemconcomp.2016.05.023.

[96]   W. C. Oliver and G. M. Pharr, "An improved technique for determining hardness and elastic-modulus using load and displacement sensing indentation experiments," *J Mater Res*, vol. 7, no. 6, pp. 1564–1583, 1992, doi: 10.1557/.

[97]   I. G. Richardson, "Nature of C-S-H in hardened cements," *Cem Concr Res*, vol. 29, no. 8, 1999, doi: 10.1016/S0008-8846(99)00168-4.

[98]   H. Lechert, " G. Engelhardt und D. Michel: High Resolution Solid State NMR of Silicates and Zeolites . John Wiley & Sons, Chichester, New York, Brisbane, Toronto, Singapore, 1987. 485 Seiten, Preis: $ 55.-. ," *Berichte der Bunsengesellschaft für physikalische Chemie*, vol. 92, no. 9, 1988, doi: 10.1002/bbpc.198800267.

[99]   T. F. Sevelsted and J. Skibsted, "Carbonation of C–S–H and C–A–S–H samples studied by 13C, 27Al and 29Si MAS NMR spectroscopy," *Cem Concr Res*, vol. 71, pp. 56–65, 2015, doi: 10.1016/j.cemconres.2015.01.019.

[100]   X. Cong and R. J. Kirkpatrick, "29Si MAS NMR study of the structure of calcium silicate hydrate," *Advanced Cement Based Materials*, vol. 3, no. 96, pp. 144–156, 1996, doi: 10.1016/S1065-7355(96)90046-2.

[101]   M. Schönlein and J. Plank, "A TEM study on the very early crystallization of C-S-H in the presence of polycarboxylate superplasticizers : Transformation from initial C-S-H globules to nanofoils," *Cem Concr Res*, vol. 106, no. June 2017, pp. 33–39, 2018, doi: 10.1016/j.cemconres.2018.01.017.

[102]   R. Hay, J. Li, and K. Celik, "Phase evolution, micromechanical properties , and morphology of calcium (alumino) silicate hydrates C-(A-) S-H under carbonation," *Cem Concr Res*, vol. 152, no. November 2021, p. 106683, 2022, doi: 10.1016/j.cemconres.2021.106683.

[103]   Z. Liu *et al.*, "Effect of polydopamine on the biomimetic mineralization of mussel-inspired calcium phosphate cement in vitro," *Materials Science and Engineering C*, vol. 44, pp. 44–51, 2014, doi: 10.1016/j.msec.2014.07.063.

[104]   M. Kamali and A. Ghahremaninezhad, "Effect of Biomolecules on the Nanostructure and Nanomechanical Property of," no. June, pp. 1–16, 2018, doi: 10.1038/s41598-018-27746-x.

[105]   V. Morales-Florez, N. Findling, and F. Brunet, "Changes on the nanostructure of cementitius calcium silicate hydrates (C–S–H) induced by aqueous carbonation," *J Mater Sci*, vol. 47, no. 2, pp. 764–771, Aug. 2011, doi: 10.1007/s10853-011-5852-6.

[106]   W. Ashraf and J. Olek, "Carbonation behavior of hydraulic and non-hydraulic calcium silicates: potential of utilizing low-lime calcium silicates in cement-based materials," *J Mater Sci*, vol. 51, no. 13, pp. 6173–6191, 2016, doi: 10.1007/s10853-016-9909-4.

[107]   N. Y. Mostafa, A. A. Shaltout, H. Omar, and S. A. Abo-el-enein, "Hydrothermal synthesis and characterization of aluminium and sulfate substituted 1 . 1 nm tobermorites," vol. 467, pp. 332–337, 2009, doi: 10.1016/j.jallcom.2007.11.130.

[108] P. Yin, "IR - Spectroscopic Investigations of the Kinetics of Calcium Carbonate Precipitation," 2016.

[109] N. V Vagenas, A. Gatsouli, and C. G. Kontoyannis, "Quantitative analysis of synthetic calcium carbonate polymorphs using FT-IR spectroscopy," *Talanta*, vol. 59, pp. 831–836, 2003, doi: 10.1016/S0039-9140(02)00638-0.

[110] P. Yin, "IR - Spectroscopic Investigations of the Kinetics of Calcium Carbonate Precipitation," 2016.

[111] F. a. Andersen and L. Brečević, "Infrared Spectra of Amorphous and Crystalline Calcium Carbonate.," *Acta Chemica Scandinavica*, vol. 45. pp. 1018–1024, 1991. doi: 10.3891/acta.chem.scand.45-1018.

[112] N. Koga, Y. Nakagoe, and H. Tanaka, "Crystallization of amorphous calcium carbonate," *Thermochim Acta*, vol. 318, no. September 1997, pp. 239–244, 1998.

[113] Z. Zou *et al.*, "Opposite Particle Size E ff ect on Amorphous Calcium Carbonate Crystallization in Water and during Heating in Air," *Chemistry of Materials*, vol. 27, pp. 4237–4246, 2015, doi: 10.1021/acs.chemmater.5b00145.

[114] N. Nassrallah-Aboukaïs, C. Jacquemin, J., Decarne, E. Abi-Aad, J. F. Lamonier, and A. Aboukaïs, "Transformation of vaterite into calcite in the absence and the presence of copper (II) species . Thermal analysis , IR and EPR study E," *J Therm Anal Calorim*, vol. 74, no. 1, pp. 21–27, 2003.

[115] R. Hay, J. Li, and K. Celik, "Phase evolution, micromechanical properties , and morphology of calcium (alumino) silicate hydrates C-(A-) S-H under carbonation," *Cem Concr Res*, vol. 152, no. November 2021, p. 106683, 2022, doi: 10.1016/j.cemconres.2021.106683.

[116] W. Ashraf, J. Olek, and N. Tian, "Nanomechanical Characterization of the Carbonated Wollastonite System," in *Nanotechnology in Construction*, 2015. doi: 10.1007/978-3-319-17088-6_8.

[117] M. Saharay, A. O. Yazaydin, and R. J. Kirkpatrick, "Dehydration-induced amorphous phases of calcium carbonate," *Journal of Physical Chemistry B*, vol. 117, no. 12, pp. 3328–3336, 2013, doi: 10.1021/jp308353t.

[118] Y. Y. Kim *et al.*, "Tuning hardness in calcite by incorporation of amino acids," *Nat Mater*, vol. 15, no. 8, pp. 903–910, 2016, doi: 10.1038/nmat4631.

[119] M. I. Haque, I. B. Borno, R. I. Khan, and W. Ashraf, "Reducing carbonation degradation and enhancing elastic properties of calcium silicate hydrates using biomimetic molecules," *Cem Concr Compos*, vol. 136, p. 104888, Feb. 2023, doi: 10.1016/j.cemconcomp.2022.104888.

[120] G. T. Zhou, J. C. Yu, X. C. Wang, and L. Z. Zhang, "Sonochemical synthesis of aragonite-type calcium carbonate with different morphologies," *New Journal of Chemistry*, vol. 28, no. 8, 2004, doi: 10.1039/b315198k.

[121] S. Goto, K. Suenaga, and T. Kado, "Calcium silicate carbonation products," *Journal of the American Ceramic Society*, vol. 78, no. 11, pp. 2867–72, 1995.

[122] R. Berliner, C. Ball, and P. B. West, "Neutron powder diffraction investigation of model cement compounds," *Cem Concr Res*, vol. 27, no. 4, 1997, doi: 10.1016/S0008-8846(97)00028-8.

[123] I. F. Sáez Del Bosque, S. Martínez-Ramírez, and M. T. Blanco-Varela, "FTIR study of the effect of temperature and nanosilica on the nano structure of C-S-H gel formed by hydrating tricalcium silicate," *Constr Build Mater*, vol. 52, 2014, doi: 10.1016/j.conbuildmat.2013.10.056.

[124] I. Odler, "The BET-specific surface area of hydrated Portland cement and related materials," *Cem Concr Res*, vol. 33, no. 12, pp. 2049–2056, 2003, doi: 10.1016/S0008-8846(03)00225-4.

[125] S. Brunauer, P. H. Emmett, and E. Teller, "Adsorption of Gases in Multimolecular Layers," *J Am Chem Soc*, vol. 60, no. 2, 1938, doi: 10.1021/ja01269a023.

[126] E. P. Barrett, L. G. Joyner, and P. P. Halenda, "The Determination of Pore Volume and Area Distributions in Porous Substances. I. Computations from Nitrogen Isotherms," *J Am Chem Soc*, vol. 73, no. 1, 1951, doi: 10.1021/ja01145a126.

[127] D. K. Panesar and J. Francis, "Influence of limestone and slag on the pore structure of cement paste based on mercury intrusion porosimetry and water vapour sorption measurements," *Constr Build Mater*, vol. 52, 2014, doi: 10.1016/j.conbuildmat.2013.11.022.

[128] W. Ashraf, J. Olek, and N. Tian, "Multiscale characterization of carbonated wollastonite paste and application of homogenization schemes to predict its effective elastic modulus," *Cem Concr Compos*, vol. 72, pp. 284–298, 2016, doi: 10.1016/j.cemconcomp.2016.05.023.

[129] R. I. Khan, S. Siddique, and W. Ashraf, "Effects of magnesia in semi-hydraulic and non-hydraulic calcium silicate binders during carbonation curing," *Constr Build Mater*, vol. 338, p. 127628, Jul. 2022, doi: 10.1016/j.conbuildmat.2022.127628.

[130] S. H. Lee, K. Kim, Mabudo, and M. S. Song, "Physical and chemical properties of cement mortar with gamma-C2S," *Journal of the Korean Ceramic Society*, vol. 53, no. 2, 2016, doi: 10.4191/kcers.2016.53.2.194.

[131] R. I. Khan, M. I. Haque, W. Ashraf, S. Shah, and N. Saleh, "Role of biopolymers in enhancing multiscale characteristics of carbonation-cured cementitious composites," *Cem Concr Compos*, vol. 134, p. 104766, 2022, doi: https://doi.org/10.1016/j.cemconcomp.2022.104766.

[132] F. A. Andersen and L. Brečević, "Infrared spectra of amorphous and crystalline calcium carbonate," *Acta Chem Scand*, vol. 45, 1991, doi: 10.3891/acta.chem.scand.45-1018.

[133] C. E. Weir and E. R. Lippincott, "Infrared studies of aragonite, calcite, and vaterite type structures in the borates, carbonates, and nitrates," *J Res Natl Bur Stand A Phys Chem*, vol. 65A, no. 3, p. 173, 1961, doi: 10.6028/jres.065a.021.

[134] M. Sato and S. Matsuda, "Structure of vaterite and infrared spectra," *Zeitschrift fur Kristallographie - New Crystal Structures*, vol. 129, no. 5–6, pp. 405–410, 1969, doi: 10.1524/zkri.1969.129.5-6.405.

[135] D. Chakrabarty and S. Mahapatra, "Aragonite crystals with unconventional morphologies," *J Mater Chem*, vol. 9, no. 11, pp. 2953–2957, 1999, doi: 10.1039/a905407c.

[136] V. Baroghel-Bouny, "Water vapour sorption experiments on hardened cementitious materials," *Cem Concr Res*, vol. 37, no. 3, 2007, doi: 10.1016/j.cemconres.2006.11.019.

[137] W. Ashraf and J. Olek, "Elucidating the accelerated carbonation products of calcium silicates using multi-technique approach," *Journal of CO2 Utilization*, vol. 23, pp. 61–74, Jan. 2018, doi: 10.1016/j.jcou.2017.11.003.

[138] G. Constantinides, K. S. Ravi Chandran, F. J. Ulm, and K. J. van Vliet, "Grid indentation analysis of composite microstructure and mechanics: Principles and validation," *Materials Science and Engineering A*, vol. 430, no. 1–2, pp. 189–202, 2006, doi: 10.1016/j.msea.2006.05.125.

[139] W. Ashraf, J. Olek, and J. Jain, "Microscopic features of non-hydraulic calcium silicate cement paste and mortar," *Cem Concr Res*, vol. 100, 2017, doi: 10.1016/j.cemconres.2017.07.001.

[140] M. Miller, C. Bobko, M. Vandamme, and F. Ulm, "Surface roughness criteria for cement paste nanoindentation," vol. 38, pp. 467–476, 2008, doi: 10.1016/j.cemconres.2007.11.014.

[141] N. K. Dhami, A. Mukherjee, and M. S. Reddy, "Micrographical, minerological and nano-mechanical characterisation of microbial carbonates from urease and carbonic anhydrase producing bacteria," *Ecol Eng*, vol. 94, pp. 443–454, Sep. 2016, doi: 10.1016/j.ecoleng.2016.06.013.

[142] R. L. Willett, K. W. Baldwin, K. W. West, and L. N. Pfeiffer, "Differential adhesion of amino acids to inorganic surfaces," *Proc Natl Acad Sci U S A*, vol. 102, no. 22, 2005, doi: 10.1073/pnas.0408565102.

[143] O. Schussler *et al.*, "Use of arginine-glycine-aspartic acid adhesion peptides coupled with a new collagen scaffold to engineer a myocardium-like tissue graft," *Nat Clin Pract Cardiovasc Med*, vol. 6, no. 3, 2009, doi: 10.1038/ncpcardio1451.

[144] J. J. Hwang and S. I. Stupp, "Poly(amino acid) bioadhesives for tissue repair," *J Biomater Sci Polym Ed*, vol. 11, no. 10, 2000, doi: 10.1163/156856200743553.

[145] B. Ma, Y. Peng, H. Tan, Z. Lv, and X. Deng, "Effect of polyacrylic acid on rheology of cement paste plasticized by polycarboxylate superplasticizer," *Materials*, vol. 11, no. 7, Jun. 2018, doi: 10.3390/ma11071081.

[146] Y. Guo *et al.*, "Effect of polyacrylic acid emulsion on fluidity of cement paste," *Colloids Surf A Physicochem Eng Asp*, vol. 535, pp. 139–148, Dec. 2017, doi: 10.1016/j.colsurfa.2017.09.039.

[147] S. Ouhenia, D. Chateigner, M. A. Belkhir, E. Guilmeau, and C. Krauss, "Synthesis of calcium carbonate polymorphs in the presence of polyacrylic acid," *J Cryst Growth*, vol. 310, no. 11, pp. 2832–2841, May 2008, doi: 10.1016/j.jcrysgro.2008.02.006.

[148] H. Watamura, Y. Sonobe, and I. Hirasawa, "Polyacrylic Acid-Assisted Crystallization Phenomena of Carbonate Crystals," *Chem Eng Technol*, vol. 37, no. 8, pp. 1422–1426, 2014, doi: 10.1002/ceat.201400017.

[149] S. C. Huang, K. Naka, and Y. Chujo, "Effect of molecular weights of poly(acrylic acid) on crystallization of calcium carbonate by the delayed addition method," *Polym J*, vol. 40, no. 2, 2008, doi: 10.1295/polymj.PJ2007162.

[150] R. I. Khan, M. I. Haque, W. Ashraf, S. Shah, and N. Saleh, "Role of biopolymers in enhancing multiscale characteristics of carbonation-cured cementitious composites," *Cem Concr Compos*, vol. 134, Nov. 2022, doi: 10.1016/j.cemconcomp.2022.104766.

[151] L. Wang, L. Chen, J. L. Provis, D. C. W. Tsang, and C. S. Poon, "Accelerated carbonation of reactive MgO and Portland cement blends under flowing CO_2 gas," *Cem Concr Compos*, vol. 106, 2020, doi: 10.1016/j.cemconcomp.2019.103489.

[152] K. L. Scrivener, V. M. John, and E. M. Gartner, "Eco-efficient cements: Potential economically viable solutions for a low-CO_2 cement-based materials industry," *Cem Concr Res*, vol. 114, 2018, doi: 10.1016/j.cemconres.2018.03.015.

[153] P. J. M. Monteiro, S. A. Miller, and A. Horvath, "Towards sustainable concrete," *Nature Materials*, vol. 16, no. 7. 2017. doi: 10.1038/nmat4930.

[154] Y. Geng, Z. Wang, L. Shen, and J. Zhao, "Calculating of CO_2 emission factors for Chinese cement production based on inorganic carbon and organic carbon," *J Clean Prod*, vol. 217, 2019, doi: 10.1016/j.jclepro.2019.01.224.

[155] L. Barcelo, J. Kline, G. Walenta, and E. Gartner, "Cement and carbon emissions," *Materials and Structures/Materiaux et Constructions*, vol. 47, no. 6, 2014, doi: 10.1617/s11527-013-0114-5.

[156] W. Ashraf and J. Olek, "Carbonation activated binders from pure calcium silicates: Reaction kinetics and performance controlling factors," *Cem Concr Compos*, 2018, doi: 10.1016/j.cemconcomp.2018.07.004.

[157] N. L. Mai, N. H. Hoang, H. T. Do, M. Pilz, and T. T. Trinh, "Elastic and thermodynamic properties of the major clinker phases of Portland cement: Insights from first principles calculations," *Constr Build Mater*, vol. 287, 2021, doi: 10.1016/j.conbuildmat.2021.122873.

[158] T. Staněk and P. Sulovský, "Active low-energy belite cement," *Cem Concr Res*, vol. 68, 2015, doi: 10.1016/j.cemconres.2014.11.004.

[159] Z. Wang, M. Wang, Z. Wen, and W. Zhang, "Progress on study of dicalcium silicate and low calcium cement with dicalcium silicate as a main mineral composition," *Cailiao Daobao/Materials Review*, vol. 30, no. 1. 2016. doi: 10.11896/j.issn.1005-023X.2016.01.012.

[160] J. Chang, Y. Fang, and X. Shang, "The role of β-C2S and γ-C2S in carbon capture and strength development," *Materials and Structures/Materiaux et Constructions*, vol. 49, no. 10, 2016, doi: 10.1617/s11527-016-0797-5.

[161] A. Elhoweris, I. Galan, and F. P. Glasser, "Stabilisation of α ′ dicalcium silicate in calcium sulfoaluminate clinker," *Advances in Cement Research*, vol. 32, no. 3, 2020, doi: 10.1680/jadcr.18.00050.

[162] J. Chang, T. Jiang, and K. Cui, "Influence on compressive strength and CO_2 capture after accelerated carbonation of combination β-C2S with γ-C2S," *Constr Build Mater*, vol. 312, 2021, doi: 10.1016/j.conbuildmat.2021.125359.

[163] Y. Fang and J. Chang, "Rapid hardening β-C2S mineral and microstructure changes activated by accelerated carbonation curing," *J Therm Anal Calorim*, vol. 129, no. 2, 2017, doi: 10.1007/s10973-017-6165-z.

[164] T. Jiang, K. Cui, and J. Chang, "Development of low-carbon cement: Carbonation of compounded C2S by β-C2S and γ-C2S," *Cem Concr Compos*, vol. 139, 2023, doi: 10.1016/j.cemconcomp.2023.105071.

[165] X. Guan, S. Liu, C. Feng, and M. Qiu, "The hardening behavior of γ-C2S binder using accelerated carbonation," *Constr Build Mater*, vol. 114, 2016, doi: 10.1016/j.conbuildmat.2016.03.208.

[166] Z. Ghouleh, R. I. L. Guthrie, and Y. Shao, "High-strength KOBM steel slag binder activated by carbonation," *Constr Build Mater*, vol. 99, 2015, doi: 10.1016/j.conbuildmat.2015.09.028.

[167] D. R. Moorehead, "Cementation by the carbonation of hydrated lime," *Cem Concr Res*, vol. 16, no. 5, 1986, doi: 10.1016/0008-8846(86)90044-X.

[168] B. Lu, S. Drissi, J. Liu, X. Hu, B. Song, and C. Shi, "Effect of temperature on CO2 curing, compressive strength and microstructure of cement paste," *Cem Concr Res*, vol. 157, 2022, doi: 10.1016/j.cemconres.2022.106827.

[169] E. Baffoe and A. Ghahremaninezhad, "Effect of proteins on the mineralization, microstructure and mechanical properties of carbonation cured calcium silicate," *Cem Concr Compos*, vol. 141, p. 105121, Aug. 2023, doi: 10.1016/j.cemconcomp.2023.105121.

[170] F. Wu *et al.*, "Increasing flexural strength of CO2 cured cement paste by CaCO3 polymorph control," *Cem Concr Compos*, vol. 141, p. 105128, Aug. 2023, doi: 10.1016/j.cemconcomp.2023.105128.

[171] Y. Guo *et al.*, "Effect of polyacrylic acid emulsion on fluidity of cement paste," *Colloids Surf A Physicochem Eng Asp*, vol. 535, 2017, doi: 10.1016/j.colsurfa.2017.09.039.

[172] B. Ma *et al.*, "Preparation for polyacrylic acid modified by ester group in side chain and its application as viscosity enhancing agent in polycarboxylate superplasticizer system," *Constr Build Mater*, vol. 233, 2020, doi: 10.1016/j.conbuildmat.2019.117272.

[173] Y. Qi *et al.*, "Effects of Molecular Weight and Concentration of Poly(Acrylic Acid) on Biomimetic Mineralization of Collagen," *ACS Biomater Sci Eng*, vol. 4, no. 8, 2018, doi: 10.1021/acsbiomaterials.8b00512.

[174] L. Shen, H. Bu, Y. Zhang, P. Tang, and G. Li, "Molecular weight and concentration of poly (acrylic acid) dual-responsive homogeneous and intrafibrillar collagen mineralization using an in situ co-organization strategy," *Polym Compos*, vol. 42, no. 9, 2021, doi: 10.1002/pc.26161.

[175] A. Cuesta, A. Ayuela, and M. A. G. Aranda, "Belite cements and their activation," *Cement and Concrete Research*, vol. 140. 2021. doi: 10.1016/j.cemconres.2020.106319.

[176] H. Sun *et al.*, "Mechanical and durability properties of blended OPC mortar modified by low-carbon belite (C2S) nanoparticles," *J Clean Prod*, vol. 305, 2021, doi: 10.1016/j.jclepro.2021.127087.

[177] S. Saidani, A. Smith, Y. El Hafiane, and L. Ben Tahar, "Role of dopants (B, P and S) on the stabilization of β-Ca2SiO4," *J Eur Ceram Soc*, vol. 41, no. 1, 2021, doi: 10.1016/j.jeurceramsoc.2020.07.037.

[178] G. C. Lai, T. Nojiri, and K. ichi Nakano, "Studies of the stability of β-Ca2SiO4 doped by minor ions," *Cem Concr Res*, vol. 22, no. 5, 1992, doi: 10.1016/0008-8846(92)90097-F.

[179] D. Koumpouri and G. N. Angelopoulos, "Effect of boron waste and boric acid addition on the production of low energy belite cement," *Cem Concr Compos*, vol. 68, 2016, doi: 10.1016/j.cemconcomp.2015.12.009.

[180] A. Cuesta, E. R. Losilla, M. A. G. Aranda, J. Sanz, and Á. G. De La Torre, "Reactive belite stabilization mechanisms by boron-bearing dopants," *Cem Concr Res*, vol. 42, no. 4, 2012, doi: 10.1016/j.cemconres.2012.01.006.

[181] P. Jin, R. Wang, Y. Su, H. Dong, and Q. Wang, "Study on carbonation process of β-C2S under microbial enzymatic action," *Constr Build Mater*, vol. 228, 2019, doi: 10.1016/j.conbuildmat.2019.117110.

[182] V. Datsyuk *et al.*, "In situ nitroxide-mediated polymerized poly(acrylic acid) as a stabilizer/compatibilizer carbon nanotube/polymer composites," *J Nanomater*, vol. 2007, 2007, doi: 10.1155/2007/74769.